Subduction, underplating, and return flow recorded in the Cycladic Blueschist Unit exposed on Syros Island, Greece

Alissa Jeanne Kotowski[1,1], Whitney Maria Behr[2,2], Miguel Cisneros[3,3], Daniel Fritz Stockli[4,4], Konstantinos Soukis[5,5], Jaime Barnes[4,4], and Daniel Ortega-Arroyo[6,6]

[1]McGill University
[2]ETH Zürich
[3]ETH Zurich
[4]University of Texas at Austin
[5]National and Kapodistrian University of Athens
[6]Massachusetts Institute of Technology

November 30, 2022

Abstract

Exhumed high-pressure/low-temperature (HP/LT) metamorphic rocks provide insights into deep (~20-70 km) subduction interface dynamics. On Syros Island (Cyclades, Greece), the Cycladic Blueschist Unit (CBU) preserves blueschist-to-eclogite facies oceanic- and continental-affinity rocks that record the structural and thermal evolution associated with Eocene subduction. Despite decades of research on Syros, the pressure-temperature-deformation history (P-T-D), and timing of subduction and exhumation, are matters of ongoing discussion. Here we show that the CBU on Syros comprises three coherent tectonic slices, and each one underwent subduction, underplating, and syn-subduction return flow along similar P-T trajectories, but at progressively younger times. Subduction and return flow are distinguished by stretching lineations and ductile fold axis orientations: top-to-the-S (prograde-to-peak subduction), top-to-the-NE (blueschist facies exhumation), and then E-W coaxial stretching (greenschist facies exhumation). Amphibole chemical zonations record cooling during decompression, indicating return flow along the top of a cold subducting slab. New multi-mineral Rb-Sr isochrons and compiled metamorphic geochronology demonstrate that three nappes record distinct stages of peak subduction (53 Ma, ~50 Ma (?), and 47 Ma) that young with structural depth. Retrograde blueschist and greenschist facies fabrics span ~50-40 Ma and~43-20 Ma, respectively, and also young with structural depth. The datasets support a revised tectonic framework for the CBU, involving subduction of structurally distinct nappes and simultaneous return flow of previously accreted tectonic slices in the subduction channel shear zone. Distributed, ductile, dominantly coaxial return flow in an Eocene-Oligocene subduction channel proceeded at rates of ~1.5-5 mm/yr, and accommodated ~80% of the total exhumation of this HP/LT complex.

Subduction, underplating, and return flow recorded in the Cycladic Blueschist Unit exposed on Syros, Greece

Alissa J. Kotowski[1*], Whitney M. Behr[1,2], Miguel Cisneros[1,2], Daniel F. Stockli[1], Konstantinos Soukis[3], Jaime D. Barnes[1], Daniel Ortega-Arroyo[1†]

[1]Department of Geological Sciences, Jackson School of Geosciences, University of Texas at Austin, USA
[2]Geological Institute, Department of Earth Sciences, Swiss Federal Institute of Technology (ETH)
[3]Geology and Geoenvironment, National and Kapodistrian University of Athens, Greece

Key Points:

- Syros is a tectonic stack composed of 3 slices constructed by subduction and underplating; peak subduction ages young with structural depth.
- The subduction-to-exhumation transition is marked by kinematic rotation and cooling during decompression.
- Metamorphic geochronology indicates syn-subduction exhumation occurred continuously in an Eocene-Oligocene subduction channel.

*now at Department of Earth and Planetary Sciences, McGill University
†now at Department of Earth, Atmospheric & Planetary Sciences, Massachusetts Institute of Technology

Corresponding author: Alissa J. Kotowski, alissa.kotowski@mcgill.ca

Abstract

Exhumed high-pressure/low-temperature (HP/LT) metamorphic rocks provide insights into deep (~20-70 km) subduction interface dynamics. On Syros Island (Cyclades, Greece), the Cycladic Blueschist Unit (CBU) preserves blueschist-to-eclogite facies oceanic- and continental-affinity rocks that record the structural and thermal evolution associated with Eocene subduction. Despite decades of research, the pressure-temperature- deformation history (P-T-D) and timing of subduction and exhumation are matters of ongoing discussion. Here we show that the CBU on Syros comprises three coherent tectonic slices, and each one underwent subduction, underplating, and syn-subduction return flow along similar P-T trajectories, but at progressively younger times. Subduction and return flow are distinguished by stretching lineations and ductile fold axis orientations: top-to-the-S-SW (prograde-to-peak subduction), top-to-the-NE (blueschist facies exhumation), and then E-W coaxial stretching (greenschist facies exhumation). Amphibole chemical zonations record cooling during decompression, indicating return flow along the top of a cold subducting slab. New multi-mineral Rb-Sr isochrons and compiled metamorphic geochronology suggest that three nappes record distinct stages of peak subduction (53-52 Ma, ~50 Ma (?), and 47-45 Ma) that young with structural depth. Retrograde blueschist and greenschist facies fabrics span ~50-40 Ma and ~43-20 Ma, respectively, and also young with structural depth. The datasets support a revised tectonic framework for the CBU, involving subduction of structurally distinct nappes and simultaneous return flow of previously accreted tectonic slices in the subduction channel shear zone. Distributed, ductile, dominantly coaxial return flow in an Eocene-Oligocene subduction channel proceeded at rates of ~1.5-5 mm/yr, and accommodated ~80% of the total exhumation of this HP/LT complex.

1 Introduction

The mechanical and thermal properties of the subduction interface strongly influence the internal structure, kinematics, and dynamics of a subduction zone (e.g., Agard et al., 2018; Cloos, 1982; Gerya & Stöckhert, 2002). Along the shallow interface ($\leq$ 20 km), direct observations of the megathrust and accretionary wedge are possible through high-resolution seismic reflection imaging, ocean bottom seismometers, and ocean drilling projects (e.g., Fagereng et al., 2019; H. Kimura et al., 2010; Park et al., 2002). However, seismic tomography and earthquake seismology have limited spatial and temporal resolution (e.g., Calvert et al., 2011; Rondenay et al., 2008) so the geometry and internal structure of the deep interface (~20-70+ km) remain poorly understood (Agard et al., 2018; Chemenda et al., 1995; Gerya & Stöckhert, 2002; Platt, 1993).

The deep interface can be studied through geologic observations of exhumed high-pressure/low-temperature (HP/LT) metamorphic rocks. Some of the most spectacular examples – e.g., the Franciscan Complex (e.g., Cloos, 1986; Wakabayashi, 1990), Japan (Aoki et al., 2008; G. Kimura et al., 2012), and the Mediterranean region (e.g., Brun & Faccenna, 2008; Jolivet et al., 2003; Platt et al., 1998) – have profoundly shaped our understanding of subduction and exhumation processes. Specifically, field studies provide constraints on the structural and kinematic evolution, interface geometry, metamorphic pressure-temperature (P-T) trajectories, and timing and rates of subduction and exhumation (e.g., Agard et al., 2018; Angiboust et al., 2016; Behr & Platt, 2012; Dragovic et al., 2015; Platt et al., 2018; Ukar et al., 2012; Xia & Platt, 2017). Geologic observations can validate or challenge the results of geodynamic simulations that model the kinematics and dynamics of rock within plate boundary shear zones (e.g., Cloos, 1982; Gerya & Stöckhert, 2002; Gerya et al., 2002; Warren et al., 2008).

Syros Island, located in the central Aegean Sea (Fig. 1), is an ideal locality to study deep subduction interface processes due to its exceptional preservation and exposure of HP/LT blueschist-to-eclogite facies assemblages (Dürr et al., 1978; Okrusch & Bröcker, 1990; Ridley, 1982, 1984). Despite decades of research on Syros, there are many disagreements regarding the structural evolution, metamorphic conditions, and timing and mechanisms of subduction and exhumation on the island (e.g., Aravadinou & Xypolias, 2017; Bröcker et al., 2013; Keiter et al., 2004; Laurent et al., 2016, 2018; Lister & Forster, 2016; Ridley, 1982; Ring & Layer, 2003; Rosenbaum et al., 2002; Schumacher et al., 2008; Skelton et al., 2019; Soukis & Stockli, 2013; Trotet, Jolivet, & Vidal, 2001). Furthermore, crustal-scale extensional detachments that accommodated the latest stages of post-orogenic exhumation are well-documented across the Cyclades (Avigad & Garfunkel, 1989, 1991; Gautier et al., 1993; Grasemann et al., 2012; Jolivet et al., 2010; Jolivet & Brun, 2010; Schneider et al., 2018; Soukis & Stockli, 2013), but workers still debate the relative importance of major detachments during syn-orogenic exhumation from peak conditions, and whether strain was distributed or highly localized on Syros (Bond et al., 2007; Keiter et al., 2004; Laurent et al., 2016; Lister & Forster, 2016; Rosenbaum et al., 2002).

In this work, we present new structural and petrologic data and Rb-Sr geochronology, and integrate our results with a synthesis of previously published geochronology, to present a new model for the evolution of the CBU on Syros. Our results refine the island's deformation-metamorphism history, and shed light on the kinematics, metamorphic conditions, and timing of subduction and return flow in the Hellenic subduction zone. This work has implications for rates and mechanisms of HP/LT rock exhumation, and provides a broader framework for regional construction of the Attic-Cycladic Complex.

2 Regional Geologic Setting

The Cycladic Islands and parts of mainland Greece are part of the Attic-Cycladic Complex (ACC), which is divided into three units according to depositional age and metamorphic history. From structural top to bottom, the units are: (1) the Upper Cycladic Nappe; (2) the Cycladic Blueschist Unit; and (3) the Basal Unit (e.g., Altherr et al., 1994; Avigad & Garfunkel, 1989; Dürr et al., 1978; Jacobshagen, 1986; van der Maar & Jansen, 1983) (Fig. 1). The Upper Cycladic Nappe is a suite of ophiolitic slivers, altered carbonates $\pm$ serpentinites, Late Cretaceous (70-100 Ma) amphibolite-facies orthogneisses, and Miocene greenschist-facies meta-basalts, and correlates with the Pelagonian Unit exposed on mainland Greece (Papanikolaou, 1987). The Upper Nappe was the upper plate during Late Cretaceous-Paleogene subduction and crops out above the Cycladic Blueschist Unit (CBU) in the hanging wall of crustal-scale, Miocene detachment faults on several Cycladic Islands (Jolivet et al., 2010, 2013; Soukis & Stockli, 2013).

The majority of the ACC is composed of the Cycladic Blueschist Unit (CBU) (Fig. 1). The CBU comprises poly-metamorphosed tectonic slices (Dürr et al., 1978; Forster & Lister, 2005, 2008; Jolivet & Brun, 2010) of the following protoliths: (1) (Jurassic?-to-) Cretaceous ($\sim$80 Ma) mafic igneous crust with enriched-MORB and back-arc geochemical signatures $\pm$ serpentinized mantle (Bonneau, 1984; Bulle et al., 2010; Cooperdock et al., 2018; Fu et al., 2015; Seck et al., 1996; Tomaschek et al., 2003), (2) Triassic ($\sim$240 Ma) bimodal rift volcanics (Bolhar et al., 2017; Keay, 1998; Löwen et al., 2015; Robertson, 2007) blanketed by Triassic-to-Cretaceous, locally-sourced, rifted and passive continental margin siliciclastic and carbonate rocks (Löwen et al., 2015; Papanikolaou, 2013; Poulaki et al., 2019; Seman, 2016; Seman et al., 2017), and (3) peri-Gondwanan basement cross-cut by Carboniferous calc-alkaline granitoids (Flansburg et al., 2019; Keay, 1998; Keay & Lister, 2002). Regionally, CBU lithologies record evidence for HP/LT metamorphism under blueschist-to-eclogite facies ('M1') conditions between $\sim$53-30 Ma (Cliff et al., 2016; Dixon, 1976; Lagos et al., 2007; Laurent et al., 2017; Okrusch & Bröcker, 1990; Ring, Glodny, et al., 2007; Schliestedt, 1986; Tomaschek et al., 2003; J. R. Wijbrans et al., 1990) . The CBU was exhumed first within the subduction channel, leading to blueschist and greenschist facies overprinting (e.g. Cliff et al., 2016; Kotowski & Behr, 2019; Laurent et al., 2018; Ring et al., 2020), and then in the footwalls of crustal-scale, low-angle normal faults of the North, West, and South Cycladic (Grasemann et al., 2012; Jolivet et al., 2003, 2010; Jolivet & Brun, 2010; Ring et al., 2003, 2011; Roche et al., 2016; Soukis & Stockli, 2013), the

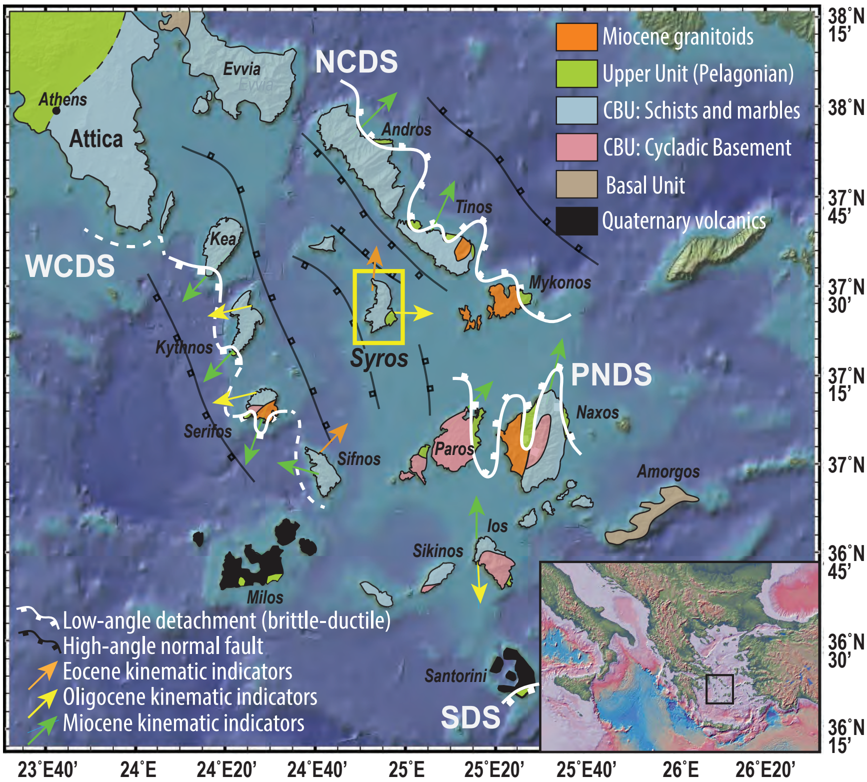

Figure 1: Regional tectonic map of the Cyclades, modified from Grasemann et al. (2012). Syros is outlined by the yellow box. North Cycladic (NCDS), West Cycladic (WCDS), Paros-Naxos (PNDS), and Santorini (SDS) Detachment Systems are outlined in white. Kinematic indicators are from Aravadinou et al. (2016), Forster et al. (2020), Grasemann et al. (2012), Huet et al. (2009) and references therein.

Paros-Naxos (Gautier et al., 1993), and the Santorini Detachment Systems (Schneider et al., 2018). Exhumation beneath ductile and semi-brittle detachments led to the development of Metamorphic Core Complexes (MCCs) that locally also produced a greenschist-facies ('M2') overprint (Bröcker, 1990; Bröcker et al., 1993). As slab rollback initiated and the arc migrated southward through the former forearc, Miocene I-type plutons intruded the exhuming CBU, and MCC formation led to a local high-temperature, amphibolite-facies ('M3') overprint on some islands (e.g., Paros and Naxos, Mykonos, and Ikaria) between ~21-17 Ma (Andriessen et al., 1979; Brichau et al., 2007; Lister et al., 1984; Pe-Piper et al., 2002; Rabillard et al., 2018; Vanderhaeghe & Whitney, 2004; J. Wijbrans & McDougall, 1988).

3 The CBU on Syros Island

3.1 Rock types and tectonostratigraphy

Syros is a small island (~84 km^2) in the central Cyclades and is dominantly composed of CBU with a klippe of UU in the southeast in the hanging wall of the Oligo-Miocene Vari Detachment (Ridley, 1984; Ring et al., 2003; Keiter et al., 2011; Soukis & Stockli, 2013) (Fig. 1). In the context of the Cyclades, Syros best preserves the regional HP/LT metamorphic event (Ridley, 1982; Okrusch & Bröcker, 1990), but similar assemblages are preserved on the island of Sifnos (Aravadinou et al., 2016; Roche et al., 2016).

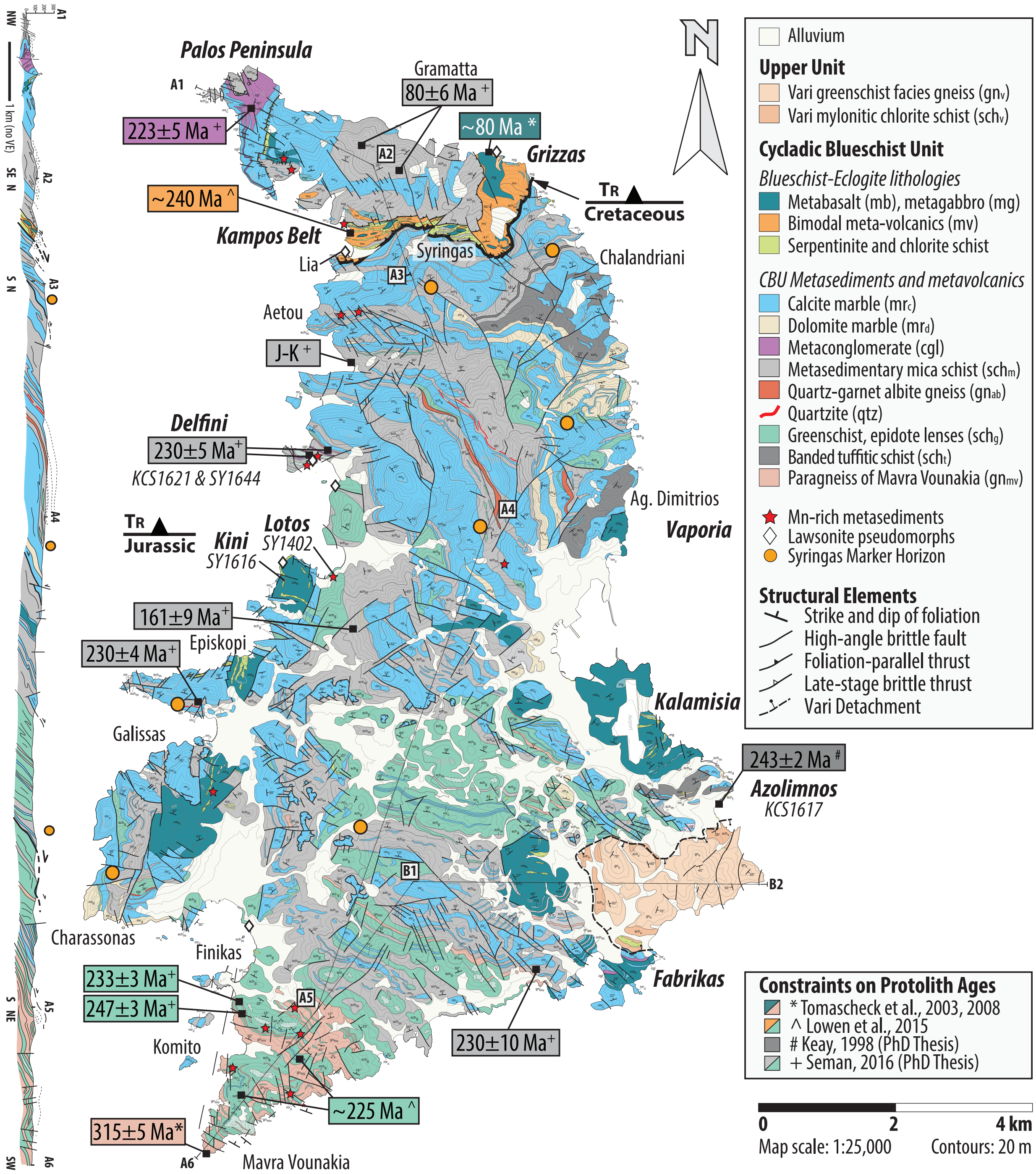

Figure 2: Geologic and structural map of Syros Island, modified from Keiter et al. (2004, 2011). Structural elements and locations of the Syringas Marker Horizon are from Keiter et al. (2011). Constraints on protolith ages are from the references discussed in Section 3.1. Protolith ages are color coded according to rock type. Localities discussed in this study are shown in bold italics, new Rb-Sr sample names and locations are in italics.

Within the CBU on Syros, mafic blueschists and eclogites crop out along three tectonostratigraphic horizons: Kampos Belt, Kini-Vaporia-Kalamisia, and Galissas-Fabrikas. Each horizon exposes ~300-500 m (structural thickness) of blueschist-to-eclogite facies meta-basalts and gabbros, serpentinites, and bimodal blueschist-quartz schist meta-volcanics in varying proportions. Along Kampos Belt, eclogitic meta-gabbros, blueschist facies bimodal meta-volcanics, and serpentinite/chlorite-talc schists are most abundant (Dixon & Ridley, 1987; Keiter et al., 2011; Ridley, 1982) (Fig. 2). Kini, Vaporia (north of Ermoupoli), and Kalamisia are primarily composed of fine-grained mafic blueschist, and contain pods and lenses of eclogite (centimeters-to-decimeters in diameter) and meters-thick layers of serpentinite/talc schist (Keiter et al., 2011; Kotowski & Behr, 2019). Fabrikas comprises coarse-grained glaucophane-bearing eclogites (centimeters to meters in diameter) within a fine-grained matrix of mafic blueschists and quartz-mica schists, capped by meta-carbonate (Kotowski & Behr, 2019; Ring et al., 2020; Skelton et al., 2019). Keiter et al. (2011) suggested that mafic blueschists and eclogites are genetically related, and changes in volume proportions of lithologies reflect primary lateral and/or vertical 'facies changes' of an enriched-MORB or back-arc igneous suite.

The majority of the CBU comprises a ~6-8 km section of intercalated meta-volcanic and meta-sedimentary schists, and calcite- and dolomite-marbles with Jurassic-to-Cretaceous depositional ages (Keiter et al., 2004; Löwen et al., 2015; Papanikolaou, 2013; Seman et al., 2017) (Fig. 2). Keiter et al. (2004, 2011) documented a series of boudinaged marbles, cherts, and albite-bearing quartzite, which they named the Syringas Marker Horizon (orange dots on Fig. 2). The sequence crops out at 3 or 4 different structural levels suggesting it marks several km-scale thrust sheets and may reflect relict primary sedimentary layering (Dixon & Ridley, 1987; Keiter et al., 2011; Ridley, 1982). Repetition of the Syringas Marker Horizon by km-scale folding is unlikely because the largest observable upright folds within this sequence have amplitudes of several hundreds of meters and the marker horizon never appears to be overturned (Keiter et al., 2011). Furthermore, Keiter et al. (2011) documented repetition of distinct packages of bimodal, rift-related meta-volcanics (also mapped as "banded tuffitic schists") that have Triassic magmatic protolith ages (Keay, 1998; Löwen et al., 2015; Pe-Piper et al., 2002; Seman, 2016) (Fig. 2), and Seman (2016) presented detrital zircon (DZ) Maximum Depositional Ages (MDA) for meta-sedimentary rocks that reveal young-on-old tectonostratigraphic inversions; both results appear to support imbrication.

3.2 Previously proposed P-T-D-t paths

Previously published P-T-D evolutions for Syros fall into two categories. Some workers have argued that the majority of deformation and metamorphism on the island is exhumation-related (Laurent et al., 2016; Lister & Forster, 2016; Trotet, Jolivet, & Vidal, 2001) (Fig. 3A). These studies interpret mafic blueschists and eclogites to occupy the top of the structural pile and separate them from underlying meta-sedimentary rocks along extensional shear zones (Forster & Lister, 2005; Laurent et al., 2016, 2018; Trotet, Vidal, & Jolivet, 2001). An implication of this model is that distinct rock types were juxtaposed during syn-orogenic exhumation (Forster & Lister, 2005; Laurent et al., 2016). Fresh and retrogressed eclogite has been documented throughout the structural pile on Syros, which is considered evidence that all rocks reached high-pressure conditions during subduction. However, lithologic packages that currently occupy different structural depths could have followed different P-T paths during exhumation (cf. Laurent et al., 2018; Trotet, Vidal, & Jolivet, 2001; Trotet, Jolivet, & Vidal, 2001), and/or could have been subducted at different times (Laurent et al., 2017; Lister & Forster, 2016). This model could potentially explain reported differences in P-T estimates across Syros; mafic blueschists and eclogites may have been subducted slightly deeper, earlier, compared to meta-sedimentary lithologies (as discussed by Schumacher et al. (2008)).

Alternatively, other work has suggested that prograde deformation and metamorphism on the island are locally preserved, and exhumation-related strain was partitioned into

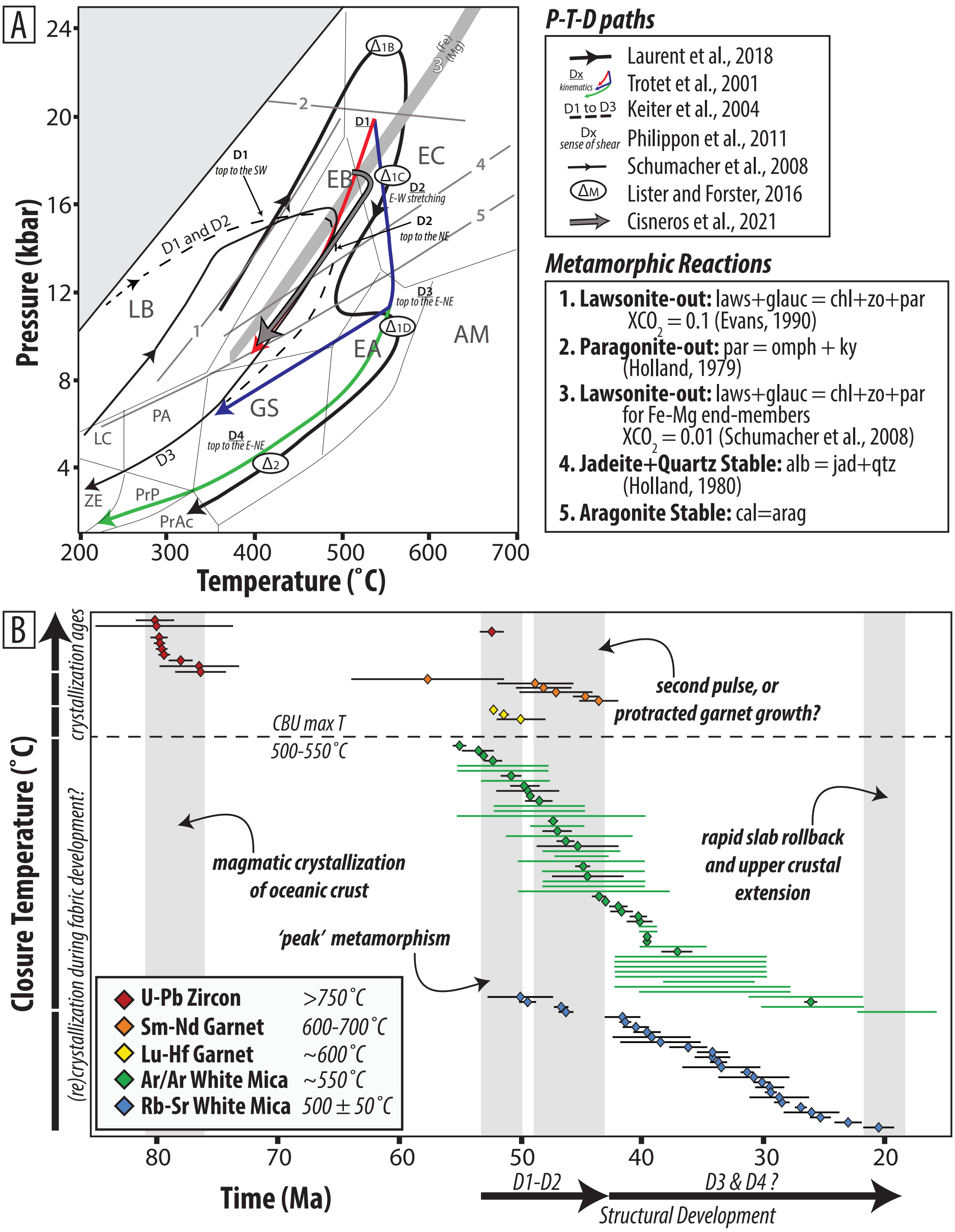

Figure 3: (A) Compilation of proposed P-T-D histories for the CBU on Syros. (B) Closure temperature vs. time for compiled metamorphic geochronology listed in Table A2. This dataset comprises 100 datapoints made up of 185 individual ages (some data clusters are weighted means), from 16 studies and 5 chronometers, from work published during the interval 1987-2019. The black bar at the bottom labeled 'structural development' shows that the timing and tectonic significance of progressive Eo-Oligocene deformation events (see also D1-D4 in panel A) and corresponding fabric development is contentious.

weaker lithologies (Bond et al., 2007; Cisneros et al., in press; Keiter et al., 2004, 2011; Ridley, 1982; Rosenbaum et al., 2002) (Fig. 3A). These studies interpret mafic blueschist and eclogites to record primary relationships with surrounding schists and marbles, or to have been juxtaposed with the schists and marbles during early thrusting (Blake Jr et al., 1981; Hecht, 1985; Keiter et al., 2004; Ridley, 1982). For either of those cases, map-scale lenses of mafic blueschists and eclogites at Vaporia, Kalamisia, and Fabrikas need not be separated from surrounding CBU by faults or shear zones (i.e., the structurally highest Kampos sub-unit of Laurent et al. (2016)), but instead could occupy a range of structural depths throughout the tectonostratigraphic pile (Keiter et al., 2004). This model implies that meta-mafic and meta-sedimentary rocks that occupy similar structural levels were subducted together and experienced similar P-T histories through subduction and exhumation (Cisneros et al., in press; Keiter et al., 2011; Schumacher et al., 2008).

Although existing metamorphic ages help to roughly distinguish prograde from retrograde fabrics, and the timing of subduction vs. exhumation, clearly differentiating between these P-T-D evolutions has been challenging because of the difficulty in assigning geologic significance to ages (Fig. 3B). Two age clusters are commonly cited for the timing of peak subduction on Syros: ∼53-50 Ma (U-Pb zircon, Ar/Ar and Rb-Sr white mica, Lu-Hf garnet; Cliff et al. (2016); Lagos et al. (2007); Lister and Forster (2016); Tomaschek et al. (2003)), and both ∼52 Ma *and* ∼45 Ma for different underplated slices (Ar/Ar white mica; Forster and Lister (2005); Laurent et al. (2017); Lister and Forster (2016)). Garnet Sm-Nd and Lu-Hf ages span the proposed range, thus raising the question of whether garnet growth reflects two pulses or continuous growth at peak conditions (cf. Kendall, 2016). Furthermore, Ar/Ar and Rb-Sr ages span the entire Eocene. Maximum CBU temperatures do not appear to have exceeded those required for diffusional resetting of the Ar/Ar and Rb-Sr systems, therefore it is unclear whether retrograde blueschist-to-greenschist facies white mica ages record incomplete isotopic mixing, and/or partial or continuous recrystallization during exhumation, beneath the isotopic closure temperature of the Ar/Ar and Rb-Sr systems (Fig. 3B) (e.g., Bröcker et al., 2013; Cliff et al., 2016; Laurent et al., 2017; Rogowitz et al., 2014; Uunk et al., 2018). An additional challenge is that many geochronologic data points in Figure 3B were collected without a clear framework for linking the ages to specific fabric-forming events.

4 Approach and Methodology

4.1 Structural and Microstructural Analysis

Following detailed mapping by Keiter et al. (2004, 2011) (map in Figure 2 and 4), we collected new structural data at several localities from Northern Syros (Fig. 4A-C), Central Syros (Fig. 4D-H), and Southeastern Syros (Fig. 4I-K). Planar and linear structural elements were measured, including foliations and cleavages, axial planes to folds, fold axes, and mineral growth, crenulation and stretching lineations. We constructed π circle diagrams to constrain fold orientations by plotting poles to metamorphic foliation planes. Each color on a given stereonet in Figure 4 corresponds to poles to foliations of a specific rock type, or poles to foliations defining single outcrop-scale folds (e.g. Fig. 5I,K). Our measurements used to produce π diagrams were all derived from cylindrical structures; even if folds have curved hinge lines on larger scales, we measured folds in locations where hinge lines are locally straight. We calculated poles to mean circles to determine fold axis orientations (bold circles), and compared them to fold axes that could be directly measured (diamonds) and mineral lineations (open circles). We documented minerals defining lineations and fold axes, porphyroblast stability and kinematic context (i.e., pre-, syn, post-kinematic with respect to surrounding fabric), and break-down and replacement textures (Fig. 5) to constrain metamorphic conditions of deformation. Microstructural analysis (Fig. 6) (139 total samples, 21 studied in detail) and quantitative EPMA analyses of zoned minerals (6 samples) further refined P-T-D conditions (Figs. 7, 8).

4.2 Rb-Sr Geochronology

We selected five samples for multi-mineral Rb-Sr geochronology. This technique has been applied to exhumed HP/LT metamorphic rocks to date deformation and metamorphism with great success (Angiboust et al., 2016; Cliff et al., 2016; Freeman et al., 1997; Glodny et al., 2005, 2008; Kirchner et al., 2016; Ring, Will, et al., 2007). The primary assumption required to construct a multi-mineral isochron is that the phases defining the isochron were co-genetic, such that they all inherited the same initial Sr composition. We separated and picked minerals that we hypothesized were co-genetic based on our structural and microstructural results, and quantitatively tested this hypothesis by identifying phases that were in isotopic disequilibrium (i.e., fell off the isochron) (Cliff & Meffan-Main, 2003). Strong foliations support the assumption of syn-kinematic recrystallization of selected minerals, which can reset the Sr isotopic signature between mica and co-genetic phases to temperatures as low as 300°C (Müller et al., 2000). Furthermore, diffusional resetting of the Rb-Sr system is thought to begin at ∼550-600°C (Glodny et al., 2008; Inger & Cliff, 1994), which exceeds maximum temperatures in the CBU. Therefore, we interpret our Rb-Sr ages as (re-)crystallization ages associated with deformation.

Following Glodny et al. (2003, 2008), we used a bulk mineral separation technique and cut out ∼5 cm^3 cubes of rock from hand samples to isolate specific fabrics corresponding to different stages of the deformation history recorded on Syros. Samples were crushed with a small hammer between sheets of paper, ground gently with a rock crusher, and sieved and separated by grain size. Grain size fractions 125-250 μm and 250-500 μm were frantzed to separate minerals based on magnetic susceptibility. Mineral separates were picked by hand under a microscope, and white mica separates were cleaned of inclusions by gently smearing them in a mortar and pestle and washing them through a sieve with ethanol. All Rb and Sr isotopic separation and analyses were done at the University of Texas at Austin in the Radiogenic Isotopic Clean Lab. All separates (except apatite) were cleaned in 2 N HCl to remove surficial contamination and spiked with mixed high Rb/Sr and low Rb/Sr spikes. We followed methodology for mineral dissolution, isotope column chemistry, Thermal Ionization Mass Spectrometry (Sr analyses), Solution Inductively Coupled Plasma Mass Spectrometry (Rb analyses), and estimating uncertainties in isotopic ratios as described in Kirchner et al. (2016). Reproducibility on replicate USGS Standard Hawaiian Basalt (BHVO) Rb measurements determine the uncertainty of the Rb-Sr ratio, and long-term reproducibility on the NBS987 Sr standard determines the uncertainty of the Sr ratio (Table 2). Ages were calculated using the IsoplotR toolbox (Vermeesch, 2018) with the ^{87}Rb decay constant of 1.3972 ± 0.0045 x 10 $^{-11}$ year $^{-1}$ (Villa et al., 2015).

5 Structures and Deformation Fabrics

The CBU on Syros records evidence for three main phases of deformation and metamorphism, herein referred to as D_R, D_S, and D_{T1-2} (Table 1). Subscripts follow an alphabetical order according to the relative age of deformation, i.e., D_R is the oldest observed deformation, and D_{T1-2} is the youngest. Each phase led to spaced to penetrative foliation development, and/or ductile folding of older foliations. Kinematic indicators, metamorphic mineral assemblages, and porphyroblast zonations described herein demonstrate that D_R and D_S developed on the prograde path and are best preserved in mafic blueschists and eclogites (but are locally preserved as textural relicts in bimodal meta-volcanics and meta-sediments), and D_T developed on the retrograde path and is best recorded by meta-volcanic and meta-sedimentary schists.

5.1 D_R – Prograde fabric development during subduction under blueschist facies conditions

D_R is the earliest recognizable prograde event but it is not visible at the outcrop-scale. D_R likely formed a strong, penetrative S_R foliation that is locally recorded as inclusion trails

Event	Context	Diagnostic Structures		Metamorphism	Example Localities
D_R	Subduction	• Only preserved as inclusion trails in garnets and as early fabric (S_R) that is tightly folded during D_S	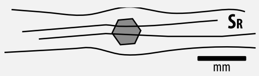	lawsonite-blueschist	N/A
D_S	Subduction to near-peak P-T conditions	• Axial plane schistosity (S_S) associated with tight to isoclinal folds (F_S) that transpose the S_R foliation, with S-SW-plunging fold axes • S-SW mineral and stretching lineations • Dominantly non-coaxial with top-S-SW sense of shear, locally non-penetrative in mafic lenses (e.g. Grizzas)	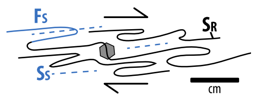	lawsonite blueschist-to-eclogite	Grizzas Kini
$D_{T1\text{-}2}$	Exhumation	• Crenulation cleavage (S_T) associated with upright, open-to-tight folds (F_T) that fold S_S • S_S foliation continuously reworked and retrogressed • Fold axes and mineral lineations rotate from N-NE (D_{T1}) to E-W (D_{T2}) as a function of strain • Dominantly coaxial, but locally non-coaxial (e.g. near the Vari Detachment at Fabrikas, Kalamisia) • Ductile to semi-brittle boudinage in later stages	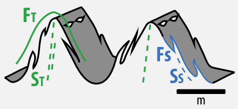	epidote-blueschist progressing to greenschist	Kampos (early) Azolimnos (early) Delfini (later) Lotos (later)

Table 1: Summary of interpreted deformation-metamorphism events in the CBU on Syros.

in garnet porphyroblasts at Kampos (Fig. 6A,B) and is tightly folded during D_S. Inclusion trails are orthogonal to the external foliation and are defined by glaucophane, omphacite, and white mica.

5.2 D_S – Prograde-to-peak fabric development during subduction under blueschist to eclogite facies conditions

5.2.1 D_S Structures

D_S is best recorded at Grizzas and Kini (Fig. 4E), with relicts preserved on Kampos Belt (Fig. 4C), at Lia Beach, and at Azolimnos (Fig. 4J). D_S produced a dominant S_S foliation in mafic blueschists, meta-cherts, and bimodal meta-volcanics at Grizzas that is parallel to the axial planes of intrafolial folds (F_S), and rotated and boudinaged quartz veins. This folding event is characterized by shallowly to moderately plunging SW-trending fold axes clustering around 205-251°/15-35°; glaucophane mineral lineations are similarly oriented (Fig. 4B). In rare cases, outcrop-scale prograde metamorphism was not associated with penetrative deformation, indicated by preservation of igneous protolith features such as pillow lavas (Grizzas, cf. Keiter et al. (2011)), intrusive relationships (Kini, cf. Kotowski and Behr (2019) and Laurent et al. (2016)), and magmatic breccias (e.g., at Grizzas, Episkopi, Fig. 5A).

Kini dominantly records D_S deformation-metamorphism; it is bounded by high-angle normal faults and is structurally discordant with respect to the surrounding CBU (Fig. 4E; cf. Keiter et al. (2011)). In one location, serpentinite wraps around the base of massive meta-gabbros, which transitions upward into fine-grained blueschists, suggesting local preservation of an attenuated section of metamorphosed oceanic lithosphere (Fig. 5B). Similar to Grizzas, the D_S fabric in Kini blueschists contains isoclinal folds (F_S) with shallowly south-plunging fold axes. This fold generation is recorded by a 182°/33° fold axis in Kini schists (Fig. 4E; Fig. 5D). The S_S axial planar cleavage seen in Kini mafic blueschists (e.g., Fig. 5C,D) is also seen as textural relicts in quartz-mica rich lithologies, as at Azolimnos (Fig. 5G). In some localities, blue amphibole lineations define great circles, likely reflecting folding of earlier

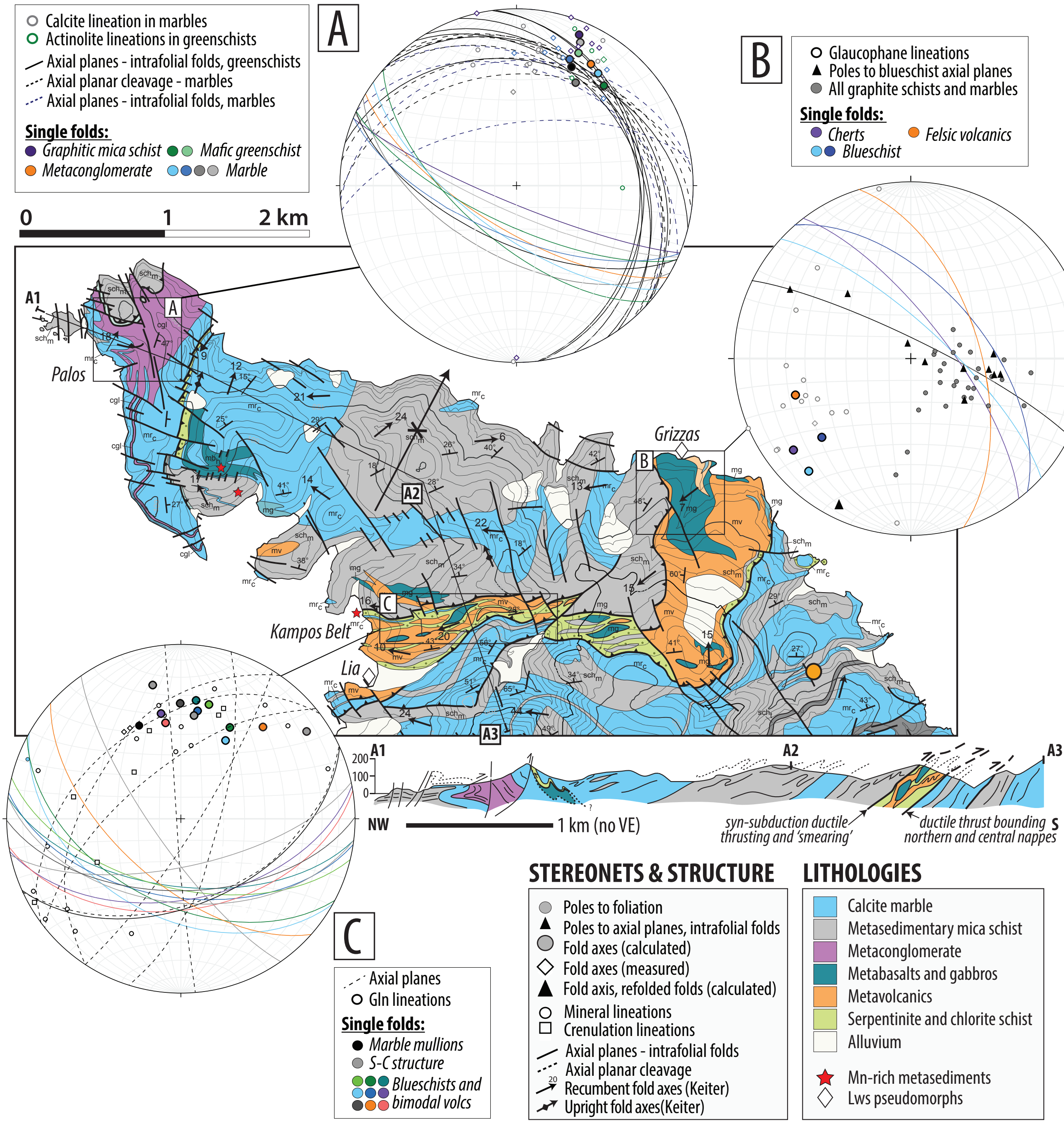

Figure 4: Geology and structural elements of Northern Syros. Base map, foliation orientations, and fold axes (black arrows) are from Keiter et al. (2011). Black fold axes are Keiter et al. (2011)'s intrafolial 'F2 shear folds.' The spread of orientations is the result of superposed folding, as older folds were progressively reoriented by S-vergent simple shear folding during prograde subduction (cf. Keiter et al., 2004). Foliations are plotted as poles (unless otherwise specified), and colored best-fit planes are π circles. Topographic contours are 20 m. New data plotted in stereonets were collected from the areas outlined by solid black boxes. Cross section A1-A2-A3 is modified from Keiter et al. (2011). See text for description of structural elements.

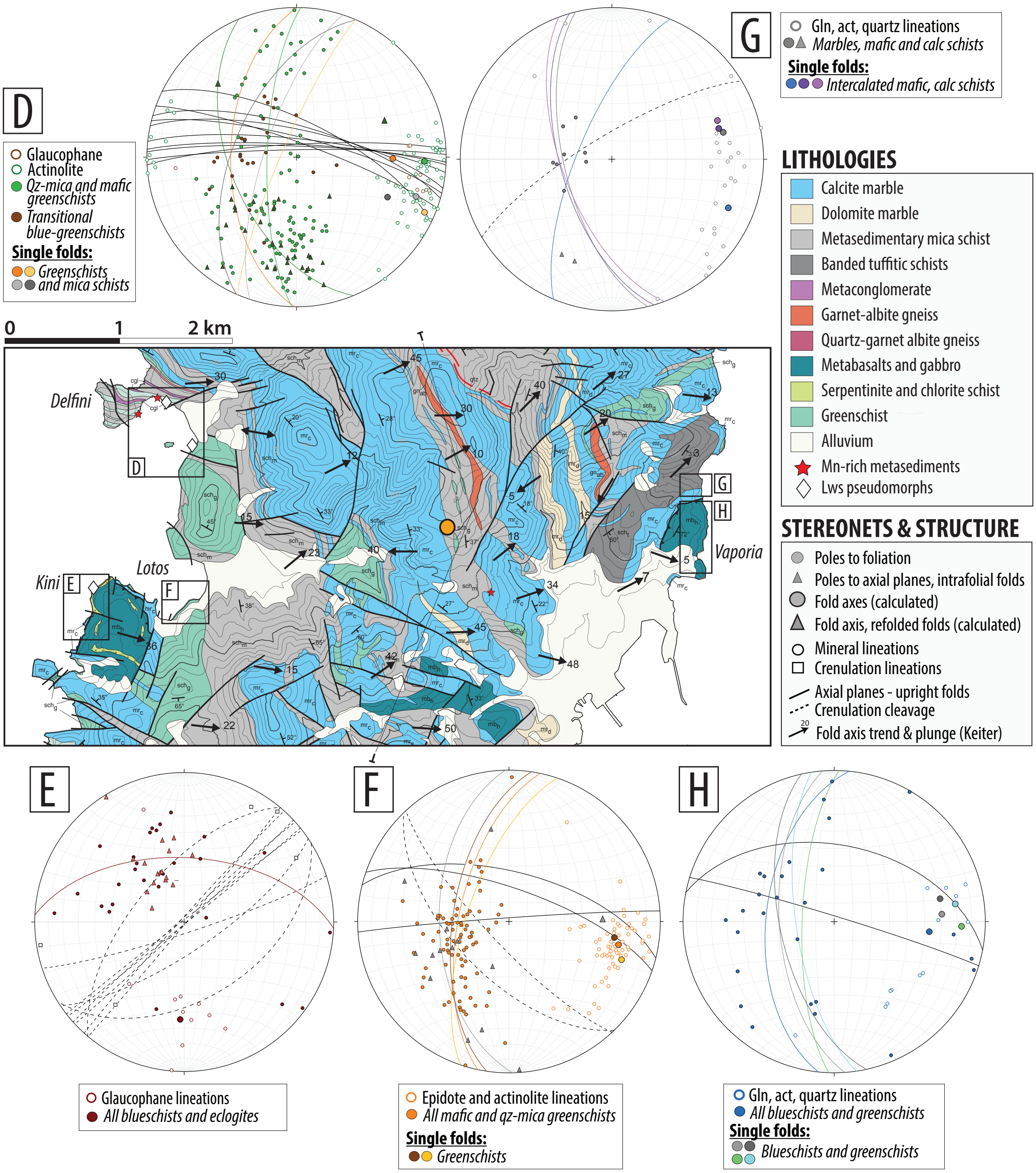

Figure 4: Continued. Geology and structural elements of Central Syros. See Fig. 2 for the cross section corresponding to the line shown.

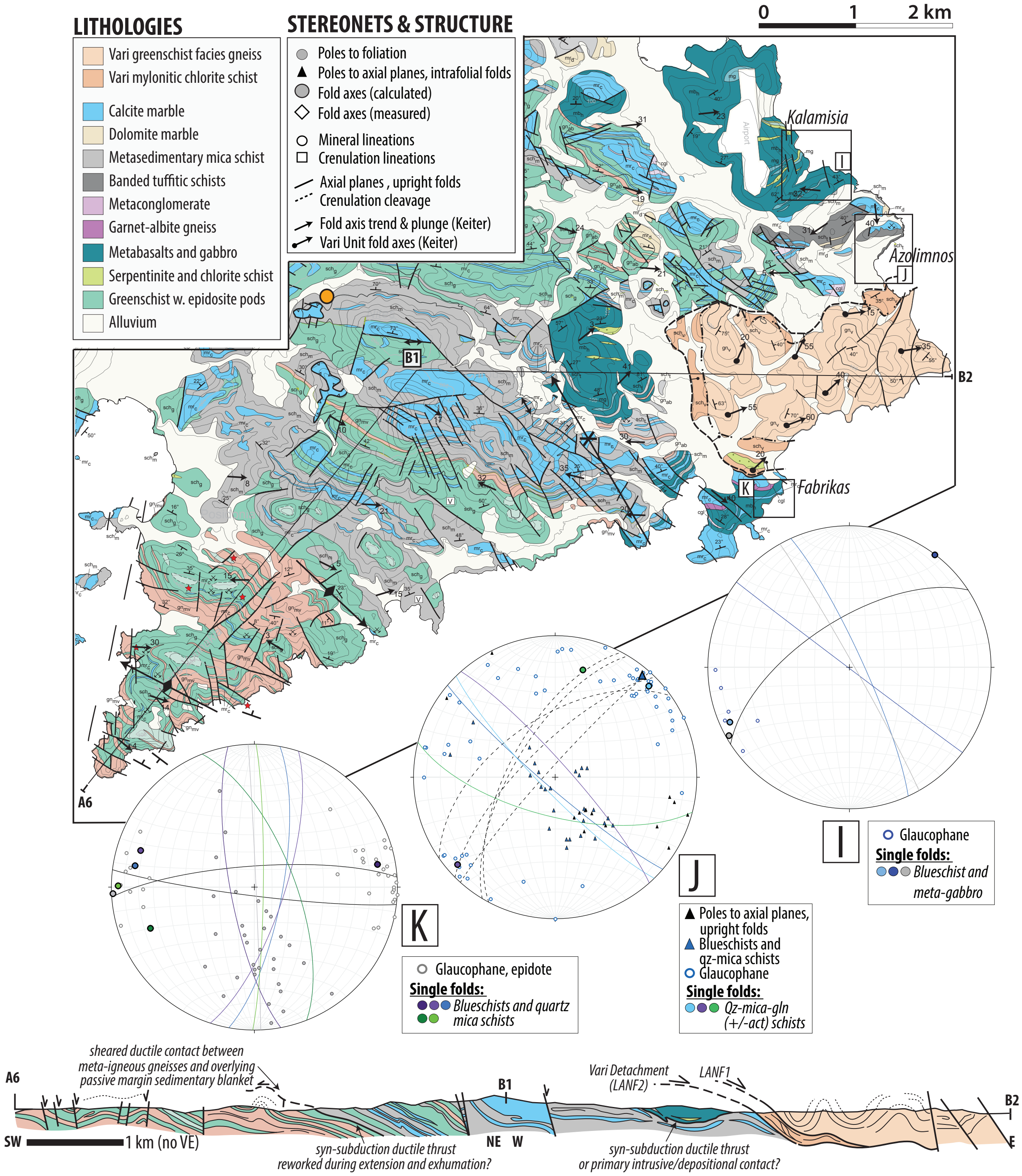

Figure 4: Continued. Geology and structural elements of Southeast Syros. Black arrows with the circles are upright fold axes in the Vari Unit. Cross section B1-B2-B3 is modified from Keiter et al. (2011); compare with Laurent et al. (2016).

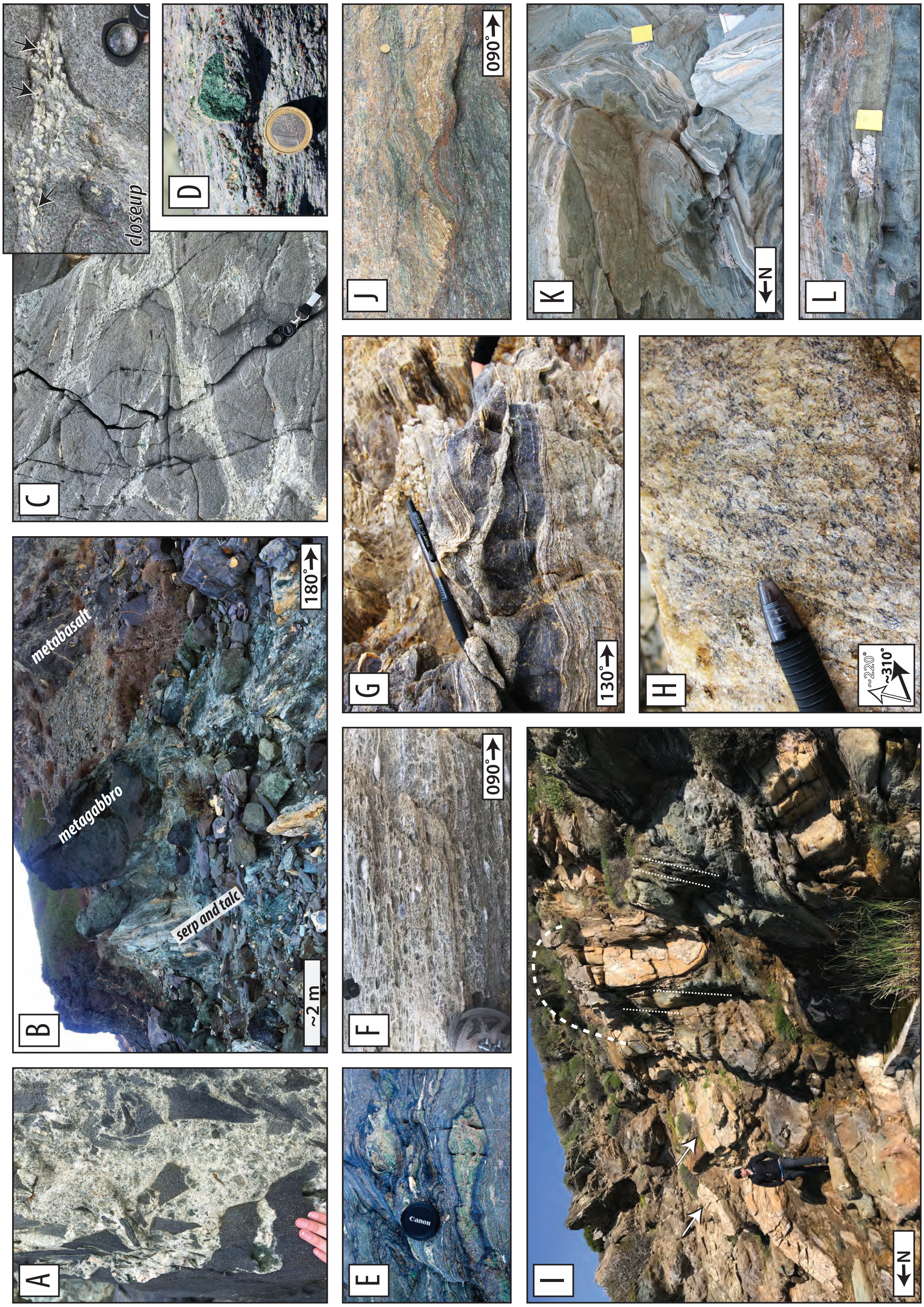

Figure 5: Caption next page.

Figure 5: (Previous page.) Selected field photos showing prograde (A-D) and retrograde (E-L) deformation and metamorphism. (A) Preservation of primary igneous breccias at Grizzas. (B) Right-side-up sequence of oceanic lithosphere at Kini. (C, D) S_S at Kini contains lawsonite pseudomorphs and omphacite with glaucophane- and garnet-filled pressure shadows. Black arrows in the close-up photo of (C) point to pseudomorphs with garnet inclusions. (E) D_{T1} retrogression under blueschist-facies conditions is marked by local static glaucophane coronas formed around pinched eclogite lenses at Vaporia. (F) Coaxial E-W stretching of calcite clasts in meta-conglomerate at Delfini during D_{T1-2}. (G,H) S_S is cut by S_{T1} crenulation cleavage at Azolimnos. (H) Two glaucophane lineations record transposition of S_S (black arrow, parallel to pen) into alignment with crenulation hinges (white arrow) during D_{T1}. (I-K) D_{T2} greenschist facies retrogression and upright folding at Delfini (I) and Lotos (K). (I) White arrows point to F_S folds along the limbs of F_T fold. Dashed white lines mark the axial planar S_T cleavage. (J) Non-coaxial, top-to-the-E extensional shear under retrograde blueschist-to-greenschist facies conditions at Fabrikas. (K) S_S cross-cut by D_T folding; fold axes trend E-W. (L) Coaxial, lineation-parallel D_{T2} brittle boudinage of epidote-rich lenses in greenschists.

(D_R) fabric during D_S (Fig. 4C, 4E; relicts at Azolimnos in Fig. 4J). In other localities, blue amphibole lineations appear to be reoriented into moderately S- or SW-plunging clusters (e.g., Grizzas and Kini, Fig. 4B,E). Similarly, Keiter et al. (2004, 2011) documented a significant spread of fold axis orientations which they attributed to superposed folding that systematically reoriented older fold hinges via S-vergent simple shear during prograde-to-peak subduction (i.e. their D_2, black fold axes in Fig. 4).

Locally, centimeter-sized, prismatic pseudomorphs after lawsonite indicate that lawsonite grew at the culmination of D_S but did not survive peak conditions. Syn-to-post-kinematic porphyroblasts overgrow the mafic blueschist foliation at Grizzas and Lia, decorate foliation-parallel compositional layers at Kini (Fig. 5C), and commonly contain inclusions of garnet, and are included by garnet (Fig. 5C, closeup). Pseudomorphs are weakly attenuated along the limbs of folds, but preserve their diamond-like shapes in fold hinges (Fig. 5C).

5.2.2 D_S Microstructures and Mineral Chemistry

D_S micro-textures in meta-sedimentary rocks are characterized by strong quartz-mica cleavage-microlithon S_S fabrics and rotated inclusion trails in garnets that are mostly continuous with external foliations (Fig. 6C). Quartz-rich microlithons have strong lineation-parallel shape-preferred orientations, and mica-rich cleavages comprise intergrown phengite and paragonite (Fig. 6C, Fig. 7C). Lawsonite pseudomorphs preserved as inclusions in garnet comprise intergrown epidote and white mica (Fig. 6D).

D_S micro-textures in mafic blueschists are characterized by compositional segregation defined by glaucophane-rich and epidote-rich layering alternating on the mm-scale ($\sim$50-200 μm grain size) (Fig. 6E). The S_S foliation contains syn-kinematic porphyroblasts of garnet and omphacite ($\sim$300 μm-5 mm), and rutile with minor titanite overgrowths (Figs. 6F, 7A). Syn-kinematic phengitic white mica is chemically homogeneous and has 3.35-3.45 Si atoms p.f.u. (Fig. B1). Omphacite and garnet deflect local foliations, and have pressure shadows and strain caps composed of glaucophane, phengite and paragonite, and/or more omphacite (Fig. 5D, 7A). Omphacite porphyroblasts in Kini blueschists have cores of low-Na, high-Mg omphacite, fringed by asymmetric, syn-kinematic pressure shadows of high-Na, low-Mg omphacite (Fig. 7A). D_S amphibole is glaucophane (Figs. 7A, 8A). Rare

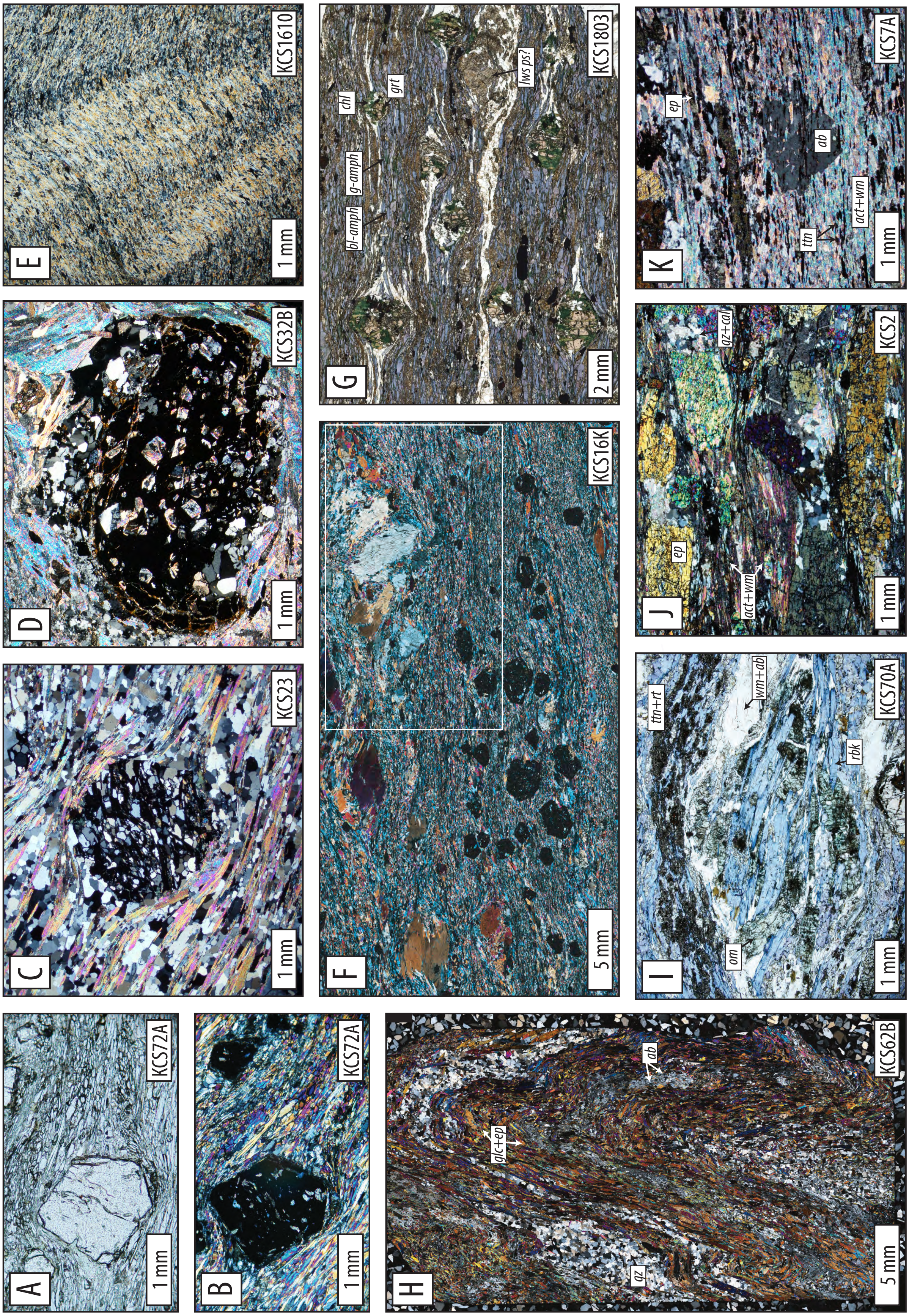

Figure 6: Caption next page.

Figure 6: (Previous page.) Selected photomicrographs showing prograde (A-F) and retrograde (E, G-K) deformation and metamorphism. (A,B) Internal S_R inclusion trails from Lia Beach (A, PPL; B, XPL). (C) S_S contains syn-kinematic garnet porphyroblasts with foamy quartz inclusion trails that are rotated but continuous with respect to the dominant external S_S foliation. (D) D_S garnets include pseudomorphs after lawsonite (comprising epidote and white mica). (E, F) S_S in mafic blueschists. (E) S_S is cut by D_{T1} crenulation under glaucophane-stable conditions in mafic blueschists. (F) Omphacite and garnet in D_S Kini blueschists have asymmetric pressure shadows filled with high-pressure minerals. (G-I) D_{T1} retrogression in bimodal meta-volcanics at Kampos (H), Azolimnos (H) and Kalamisia (I). (H) D_{T2} crenulation transposes S_S, and strengthens as albite, chlorite, and actinolite stabilize. (I) Omphacite and paragonite break down to epidote, blue amphibole, and albite. (J,K) D_{T2} in Lotos greenschists. (J) Brittle micro-boudinage of epidote porphyroblasts. (K) Final stages of D_{T2} are characterized by post-tectonic albite growth.

examples reveal glaucophane cores with thin, patchy rims (Fig. 7B) that trend towards lower $Al^{iv}/(Al^{iv}+Fe_{tot})$ values and higher $(Na+K)_A$ (Fig. 8A, Fig. B1).

5.3 D_T – Retrograde fabric development, crenulation, and re-folding through blueschist-to-greenschist facies conditions

5.3.1 D_T Structures

D_{T1} is best recorded at Kampos Belt and Palos (Fig. 4A,C), Azolimnos (Fig. 4J), and Kalamisia (Fig. 4I), and locally at Kini (Fig. 4E). D_{T1} structures refold older S_S foliations into inclined-to-upright, open-to-tight, shallowly to moderately N- and NE-plunging folds (Fig. 4C, 4G,H, 4I,J; C1). Glaucophane, calcite, and quartz mineral and stretching lineations are oriented parallel to F_T fold hinge lines (Fig. 4C,I,J). Along Kampos Belt, D_{T1} fold axes span ∼335-055°/15-45°, with a cluster of moderately N-plunging folds (e.g., Fig. 4C). At Azolimnos, D_{T1} folding locally develops an upright crenulation cleavange (S_T) that cuts the S_S foliation (Fig. 4I,J; 5G). Cm-scale spaced cleavages are parasitic to larger open folds with 045°/5-10° fold axes and steep axial planes. At Azolimnos, glaucophane lineations define a great circle and swing from N to NE into alignment with F_{T1} crenulation hinge lines (Fig. 5H). Crenulation of Kini rocks is defined by a vertical, NE-striking S_{T1} cleavage that cross-cuts mafic blueschists (Fig. 4E).

D_{T2} is characterized by E-W orientated mineral and stretching lineations that are primarily indicative of greenschist facies conditions (e.g., Lotos, Delfini; Fig. 4D,F) but locally preserve blueschist facies conditions where strain was highly non-coaxial (i.e., Fabrikas; Figs. 4K, 5J), and can be seen in a wide range of rock types throughout central and southern Syros. At Vaporia, the mafic blueschists and eclogites and the surrounding meta-sedimentary rocks develop identical D_{T2} structures (Fig. 4G,H). Single greenschist facies F_{T2} folds range in geometry from open to tight and have near-vertical, E-NE- to E-W striking axial planes. F_{T2} fold axes cluster strongly around ∼070-110°/5-30° (Figs. 4D,F; 5I,K), and mineral and stretching lineations defined by actinolite, quartz, calcite, and relict glaucophane are oriented parallel to F_{T2} hinge lines (Fig. 4 D,F,H). Older S_S foliations are progressively reworked during D_{T2} creating a composite retrogressed foliation which is visible as S- and Z-folds (e.g., Fig. 5I,K) with hinge-limb layer thickness variations locally exceeding 20:1 (Fig. C1). F_{T2} folds have axial planar cleavages decorated with actinolite, epidote, and chlorite. Coaxial stretching parallel to F_{T2} fold hinges is common, resulting in semi-brittle to brittle boudinage of epidote-rich lenses visible from the meso- to the micro-scale, as competent lithologies become brittle during exhumation (Fig. 5L). At Delfini, shear sense clast counting of a carbonate meta-conglomerate (GPS: 37°27'36" N/024°53'46" E) reveals

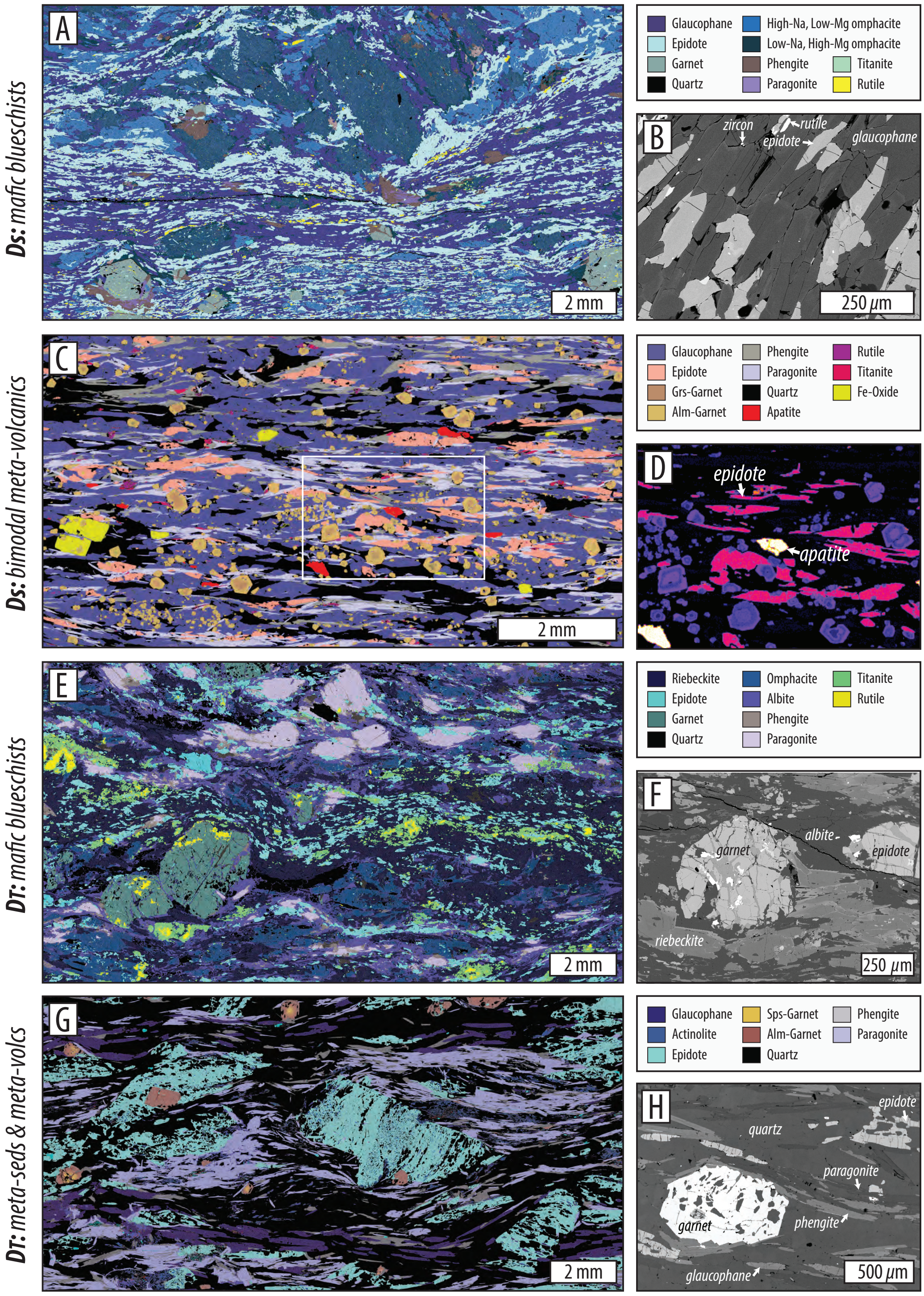

Figure 7: False-colored X-Ray maps and representative BSE images of D_S in Kini blueschists (A,B) and Azolimnos bimodal meta-volcanics (C,D), D_{T1} in Kalamisia blueschists (E,F), and D_{T2} in Fabrikas quartz-mica schists (G,H). Quantitative analyses of sodic amphiboles in (B, KCS53) and (F, KCS12B) are shown in Fig. 8; white mica analyses from (H, KCS65) are shown in Fig. B1.

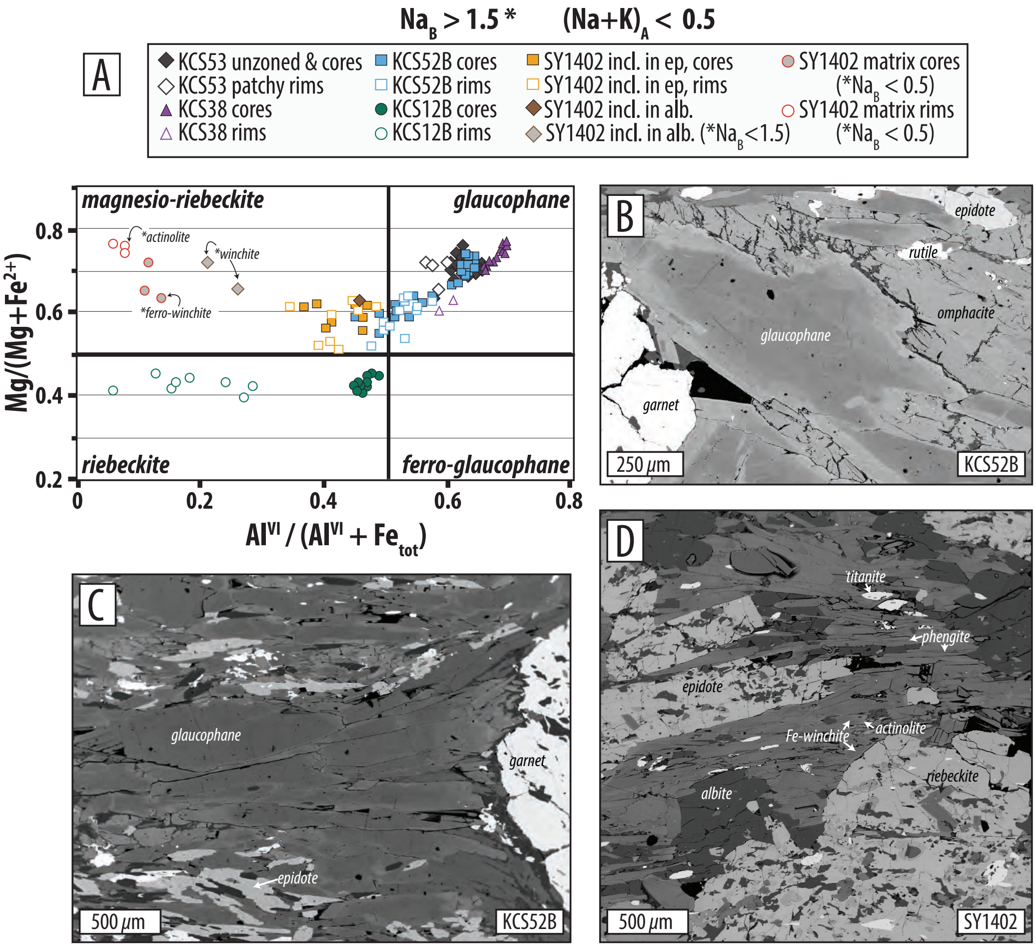

Figure 8: Amphibole mineral chemistry and micro-textures. (A) Quantitative amphibole EPMA analyses (Leake et al. (1997) classification scheme). All analyses have $Na_B > 1.5$ apfu except for those indicated with an asterisk. (B) D_{T1} static growth zonations in glaucophane contained in retrogressed eclogite pod. (C) D_{T1} lineation-parallel zonations developed in glaucophane-filled strain shadow fringing garnet porphyroclasts. (D) Greenschists preserve relict D_{T1} sodic amphibole as inclusions in epidote, and matrix amphibole records lineation-parallel compositional changes during D_{T2} retrogression.

conflicting and/or ambiguous shear sense. This is indicative of dominantly coaxial strain during reworking of a composite foliation that develops syn-kinematically with respect to upright folding (cf. Supplemental Fig. C1).

Pulses of D_T metamorphism that are not associated with penetrative strain are seen at Vaporia where pinched eclogite pods are rimmed by roughly even-thickness inky blue coronas of glaucophane (Fig. 5E), and along Kampos Belt where the margins of metagabbros develop radiating clusters of blue and green amphibole needles (Fig. C1). Although D_T strain is primarily coaxial, strongly asymmetric strain occurs locally on the E-SE side of the island. Non-coaxial D_{T1-2} is best preserved at Kalamisia and Fabrikas, respectively. At Fabrikas for example, outcrop-scale extensional shear bands and boudinage cross-cut eclogite pods and are decorated by glaucophane (partially replaced by actinolite) and quartz (Kotowski & Behr, 2019; Laurent et al., 2016).

5.3.2 D_T Microstructures and Mineral Chemistry

D_{T1} microstructures transpose and retrogress older S_S foliations, record geochemical evidence for retrogression through primarily blueschist facies conditions, and are primarily coaxial. Crenulation hinges that record D_{T1} in mafic blueschists are defined by high-Si white mica and glaucophane that has an identical composition to glaucophane defining the S_S foliation (Lia Beach, Fig. 6E; Fig. B1). Coaxial D_{T1} deformation in mafic blueschists is evidenced by symmetric strain shadows around partially chloritized garnets. During D_{T1}, S_S-defining blue amphibole grows in the symmetric strain shadows and records lineation-parallel growth zonations trending from glaucophane to magnesio-riebeckite (Vaporia, Fig. 8A,C) and locally becomes actinolitic (e.g., Kampos, Fig. 6G). Some static textures record the same compositional trend (e.g., Fig. 8A,B). At Kalamisia, extensional C-C' fabrics are well-developed in thin section, and C' top-to-the-ENE shear bands are decorated with albite, paragonite, and phengite (Fig. 7E,F). C' cleavages are also defined by finely recrystallized blue amphibole that records lineation-parallel core-to-rim zonations from high-Al riebeckite to low-Al (and lower $(Na+K)_A$) riebeckite (Figs. 6I, 7F, 8A). Omphacite and paragonite porphyroblasts record the breakdown reaction *omphacite + paragonite + H_2O = sodic amphibole + epidote + albite* (Fig. 6I), and rutile is overgrown by syn-kinematic titanite (Figs. 7E). In quartz-mica schists, the retrogressed S_S foliation comprises alternating glaucophane-rich and quartz-mica $\pm$ albite-calcite layering; the syn-D_{T1} axial planar cleavage, S_{T1}, is defined by actinolite, albite, phengite and paragonite in the cores of upright F_{T1} folds (Fig. 6H).

D_{T2} microstructures transpose and retrogress older S_S foliations, and are primarily coaxial and record geochemical evidence for retrogression under greenschist facies conditions (e.g., Delfini and Lotos). Locally D_{T2} was non-coaxial and developed under blueschist facies conditions (e.g., Fabrikas). Mafic greenschists that record D_{T2} comprise strongly retrogressed S_S foliations that are defined by fine-grained white mica, albite, epidote, actinolite, chlorite, calcite, and titanite ($\sim$50-500 μm grain size), and contain lineation-parallel epidote porphyroblasts ($\sim$2-5 mm) and unoriented, mat-like albite porphyroblasts ($\sim$1-5 mm) (Fig. 6J,K). Amphibole occurs in two distinct contexts: as inclusions in epidote and albite porphyroblasts, and as a dominant S_S foliation-forming phase. Amphibole inclusions record core-rim zonations evolving from magnesio-riebeckite to winchite, and matrix amphibole record core-rim zonations evolving from ferro-winchite to actinolite (Figs. 8A,D). S_S-defining, syn-D_{T2} epidote porphyroblasts have pressure shadows filled with white mica, calcite and albite, and are boudinaged, with necks filled by quartz and calcite (Fig. 6J, 8D). In blueschist facies fabrics at Fabrikas, the retrogressed S_S foliation comprises syn-D_{T2} epidote porphyroblasts that contain rotated inclusion trails of quartz and glaucophane and inclusions of garnet that preserve syn-D_S spessartine-to-almandine zonations (Figs. 7G,H). Phengite and paragonite define C- and C'-planes of an extensional, top-to-the-E shear fabric. Phengitic white mica reveals a tight range of Si atoms p.f.u. ($\sim$3.33-3.39 a.p.f.u, Fig. B1), and Si content of C- and C'-defining phengite is identical (Fig. 7G, Fig.

B1). Lineation-parallel brittle micro-boudinage of epidote and amphibole porphyroblasts is common; epidote boudin necks are filled with quartz, and blue amphibole boudin necks contain green amphibole needles. A planar S_{T2} fabric that cuts S_S is only found in the core of F_{T2} folds (i.e., S_{T2} crenulation cleavage at Delfini, Cisneros et al. (in press)).

6 Geochronology

6.1 New multi-mineral Rb-Sr isochron petrochronology

All of the isochrons described herein have Mean Standard Weighted Deviations (MSWDs) greater than 1, which suggests that the data dispersion exceeds that predicted by analytical uncertainties (i.e., the data are overdispersed) (Wendt & Carl, 1991). However, MSWDs are a reflection of analytical precision (e.g., Kullerud, 1991; Powell et al., 2002), and reflect the goodness of fit of a regression line to the datapoints, which includes their analytical uncertainties. Our dataset has a very high analytical precision (calculated from reproducibility of standards measurements), which leads to a significant increase in the MSWD of a Rb-Sr isochron when the regression line does pass through a datapoint's uncertainties (e.g., Fig. 9B). However, we consider our Rb-Sr ages reliable records of true deformation and metamorphism events, after closer evaluation of our isochrons (see Table A1), despite their high MSWDs. This is because the isochrons were contructed from mineral suites that our structural and petrographic observations suggest are co-genetic, and the co-linearity of the data are striking (with some justifiable exceptions discussed below). The high MSWD values may reflect underestimation of our analytical uncertainties, or minor Rb-Sr disequilibrium during metamorphism (perhaps due to incomplete recrystallization, e.g., Halama et al. (2018)) that does not significantly affect our Rb-Sr ages (Table A1).

Sample SY1616 is an omphacite-blueschist collected at Kini Beach and records D_S (texturally identical to Fig. 7A). This sample yielded an age of 53.48 ± 0.65 Ma (MSWD = 5) based on a 10-point isochron defined by epidote, glaucophane, omphacite, five paragonite separates, garnet, and one phengite separate (Table 2, Fig. 9). To test the robustness of the isochron, several two- to five-point isochrons were calculated from combinations of the co-genetic phases; the age does not change but the MSWD is reduced (=1 for 2-pt isochrons by definition; <1 for 3- and 4-pt, and 1.4-1.7 for 5-pt).

Sample KCS1617 is a bimodal meta-volcanic schist collected at Azolimnos and records D_{T1} (similar to sample in Fig. 7C). This sample yielded an age of 45.51 ± 0.29 Ma (MSWD = 8) based on a 7-point isochron defined by glaucophane, four paragonite separates, and two phengite separates (Table 2, Fig. 9). Two garnet separates fell off of the isochron and are discarded in the age calculation. We justify this based on microstructural observations shown in Figure 7D; garnets preserve complex Ca-zonation patterns and may record pulsed growth. Furthermore, garnets are D_S porphyroblasts and are not expected to be in isotopic equilibrium with the D_{T1} fabric during incipient retrogression. Previous work suggests that Sr isotopic zoning in garnets (Sousa et al., 2013) and/or isotopic inheritance from earlier stages of metamorphism and poor homogenization during subsequent stages of metamorphism (Romer & Rotzler, 2011) tend to make garnets poor candidates for constructing Rb-Sr isochrons. Adding epidote to the isochron does not change the age (45.43 ± 0.46 Ma, n=8), but increases the MSWD to 23. Epidote is stable throughout subduction and exhumation and could record subtle zonations that grew during subsequent deformation events and therefore may not be co-genetic (e.g., Cisneros et al., in press).

Sample KCS1621 is a quartz-mica schist collected from Delfini and records D_{T2} in meta-sedimentary schists. It was collected from a fold limb of a structure like the one in Fig. 5I, and is interlayered with quartz-schists on the decimeter-scale that locally preserve blue amphibole lineations. This sample yielded an age of 37.06 ± 0.12 Ma (MSWD = 13) based on a 7-point isochron defined by epidote, chlorite, 3 paragonite separates, and 2 phengite separates (Table 2, Fig. 9). For this sample, various combinations of 2- to

Sample ID and Summary	Mineral	Rb (ppm)	Sr (ppm)	87Rb / 86Sr	± 2σ	87Sr / 86Sr	± 2σ
SY1616: Kini omphacite-epidote blueschist	epidote (L18-001)	0.12	1008	0.00035	1.73E-07	0.703224	1.41E-05
Solution on 10 points: 53.48 ± 0.65 Ma	glaucophane (L18-010)	0.15	143	0.00301	1.50E-06	0.703225	1.41E-05
Initial 87/86 Sr: 0.703211 ± 0.000012	omphacite (L19-099)	0.28	31	0.02571	1.29E-05	0.703235	1.41E-05
MSWD = 5	paragonite (L19-097)	0.31	19	0.04765	2.38E-05	0.703244	1.41E-05
	paragonite (L19-093)	0.31	16	0.05829	2.91E-05	0.703234	1.41E-05
	paragonite, 0.5 A, 125-250 µm (L19-009)	0.37	17	0.06439	3.22E-05	0.703284	1.41E-05
	garnet #1 (L18-011)	0.29	13	0.06562	3.28E-05	0.703261	2.04E-05
	paragonite (L19-094)	1	44	0.07644	3.82E-05	0.703248	1.41E-05
	paragonite (L19-096)	6	142	0.12305	6.15E-05	0.703289	1.41E-05
	phengite, 0.4 A, 250-500 µm (L19-095)	35	24	4.26296	2.13E-03	0.706398	1.41E-05
	removed from isochron						
	garnet #2 (L19-098)	0.35	12	0.08338	4.17E-05	0.703353	1.41E-05
KCS1617: Azolimnos glaucophane-mica blueschist	paragonite (L19-103)	9	199	0.13309	6.65E-05	0.706681	1.41E-05
Solution on 7 points: 45.51 ± 0.29 Ma	paragonite (L19-102)	15	179	0.23810	1.19E-04	0.706776	1.41E-05
Initial 87/86 Sr: 0.706592 + 0.000022	glaucophane (L18-002)	0.3	3	0.33478	1.67E-04	0.706783	1.41E-05
MSWD = 8	paragonite (L19-100)	34	178	0.55161	2.76E-04	0.706927	1.41E-05
	paragonite, 0.8 A, 125-250 µm (L18-007)	5	14	0.97194	4.86E-04	0.707200	1.41E-05
	phengite (L19-101)	112	112	2.87985	1.44E-03	0.708433	1.42E-05
	phengite, 0.7 A, 250-500 µm (L18-005)	219	43	14.89794	7.45E-03	0.716067	1.43E-05
	removed from isochron						
	epidote (L18-003)	0.7	1486	0.00136	6.82E-07	0.706668	1.41E-05
	garnet #1 (L19-004)	0.69	8	0.26530	1.33E-04	0.706583	1.41E-05
	garnet #2 (L19-104)	0.87	4	0.63469	3.17E-04	0.706733	1.41E-05
KCS1621: Delfini actinolite-mica greenschist	epidote	1	1961	0.00143	5.71E-07	0.706597	1.41E-05
Solution on 7 points: 37.06 ± 0.12 Ma	paragonite, 0.6 A, 250-500 µm (L19-225)	54	258	0.60594	2.42E-04	0.706951	1.41E-05
Initial 87/86 Sr: 0.706626 + 0.000033	paragonite, 0.5 A, 125-250 µm (L19-222)	326	39	2.37806	9.51E-04	0.707878	1.42E-05
MSWD = 13	chlorite, 0.25 A, 250-500 µm (L19-226)	9	11	2.41488	9.66E-04	0.707852	1.42E-05
	paragonite, 0.6 A, 125-250 µm (L19-224)	150	155	2.79655	1.12E-03	0.708052	1.42E-05
	phengite, 0.5 A 125-250 µm (L19-223)	142	173	24.45665	9.78E-03	0.719330	1.44E-05
	phengite, 0.4 A, 250-500 µm (L19-221)	369	21	51.64803	2.07E-02	0.733354	1.47E-05
	removed from isochron						
	phengite, 0.4 A, 125-250 µm (L19-220)	343	47	21.16233	8.46E-03	0.717173	1.43E-05
SY1644: Delfini mineralization in epidosite boudin neck	epidote (L19-041)	0.23	2170	0.00031	1.23E-07	0.706608	1.41E-05
Solution on 3 points: 36.05 ± 2.6 Ma	actinolite (L19-042)	17	123	0.39700	1.59E-04	0.706899	1.41E-05
Initial 87/86 Sr: 0.706655 + 0.00058	white mica (L19-040)	303	30	29.24565	1.17E-02	0.721388	1.44E-05
MSWD = 82							
SY1402: Lotos reaction rim around epidosite pod	apatite	2	726	0.00992	5.21E-03	0.70497	8.10E-06
Solution on 5 points: 34.88 ± 5.8 Ma	white mica < 125 µm (L19-029)	204	13	47.20997	1.89E-02	0.72438	1.45E-05
Initial 87/86 Sr: 0.70455 ± 0.00363	white mica 125-250 µm (L19-030)	227	10	68.82184	2.75E-02	0.73953	1.48E-05
MSWD = 76000	white mica, 0.4 A, 250-500 µm (L19-031)	234	7	95.01809	3.80E-02	0.75342	1.51E-05
	white mica, 0.6 A, 250-500 µm (L19-032)	203	9	67.84958	2.71E-02	0.73643	1.47E-05

Table 2: Summary of Rb and Sr concentrations and measured ratios from analyzed samples. Mineral separates discarded from calculated isochrons are listed. Uncertainty in age estimate (i.e., $\pm t$) are calculated assuming overdispersion, as z = y x $\sqrt{MSWD}$, where y is the confidence interval for t using the appropriate number of degrees of freedom.

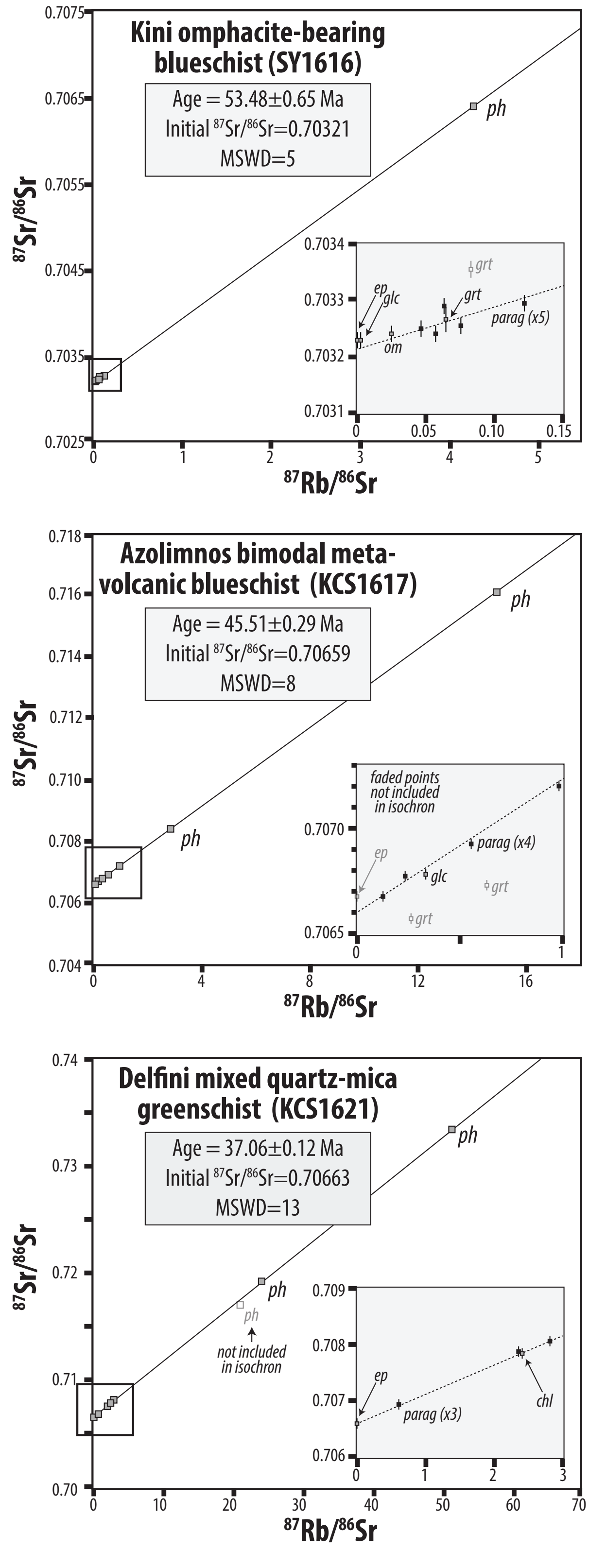

Figure 9: Multi-mineral Rb-Sr isochrons from a Kini omphacite-blueschist (SY1616), Azolimnos quartz-mica blueschist (KCS1617), and Delfini quartz-mica greenschist (KCS1621). Grey insets are zoom-ins of low Rb/Sr separates outlined in black boxes. Faded grey symbols were excluded from isochron calculations. Multiple paragonite separates for each isochron are shown in black symbols. Sample SY1616 records D_S in the northern nappe, KCS1617 records D_{T1} in the central nappe, and KCS1621 records D_{T2} in the central nappe. D_T retrogression pre-dates the onset of regional core complex capture. Mineral abbreviations: ep = epidote, glc = glaucophane, om = omphacite, grt = garnet, parag = paragonite, ph = phengite, chl = chlorite.

6-pt isochrons all yield ages of ∼35-37 Ma with MSWD varying from << 1 (e.g., 3-pt epidote-chlorite-paragonite), to 1 (e.g., 2-pt paragonite-chlorite) to 21 (e.g., 4-pt epidote-chlorite-phengite-phengite). Even the isochrons that are not defined in high-Rb space (i.e., do not contain phengite) yield nearly identical ages to the 7-point isochron (Table A1).

Sample SY1644 is a collection of minerals precipitated in the neck of a brittlely-boudinaged epidote-rich lens from Delfini, and sample SY1402 is a greenschist facies reaction rind at the margin of an epidote-rich lens from Lotos. These samples are representative of semi-brittle boudinage associated with D_{T2} stretching (e.g., Fig. 5L). These samples yield ages with reasonable uncertainties, but extremely high MSWDs. Sample SY1644 yielded an age of 36.1 ± 2.6 Ma (MSWD = 82) based on a 3-point isochron defined by epidote, actinolite, and phengite, and sample SY1402 yielded an age of 34.9 ± 5.8 Ma (MSWD = 76000) based on a 5-point isochron defined by apatite and 4 phengites (Table 2). For both samples, 2-pt isochrons yield ∼36 Ma and ∼29-36 Ma, respectively (MSWD=1; Table A1). We consider these data qualitative, but these ages are similar to and trend slightly younger than KCS1621, which is consistent with our structural observations.

6.2 Synthesis of previously published metamorphic geochronology

We compiled all available metamorphic geochronology (to our knowledge, from 1987 through 2019) for Syros, and took inventory of the descriptions of deformation fabrics and metamorphic textures provided by the authors, to re-evaluate the significance of Eocene ages in the context of subduction vs. exhumation. A full compilation is shown in Supplementary Figure A1 and Table A2. We applied several qualitative filters to the dataset to derive a subset of ages that we can confidently attribute to fabric-forming events. The filters are justified as follows:

Zircon U-Pb ages are robust records of igneous crystallization, but as metamorphic ages, can be difficult to place in pro- or retrograde context (Liu et al., 2006; Tomaschek et al., 2003; Yakymchuk et al., 2017). We include U-Pb ages from Tomaschek et al. (2003) for comparison with other ages, but we do not rely on it for island-scale interpretations. *Garnet Lu-Hf and Sm-Nd* are considered reliable indicators of 'peak' subduction ages (i.e., maximum depths) (Kendall, 2016; Lagos et al., 2007), because HP/LT garnets tend to grow rapidly following reaction overstepping (Baxter & Caddick, 2013; Dragovic et al., 2012, 2015). Kendall (2016) and Lagos et al. (2007) both reported evidence for rapid, pulsed garnet growth near peak conditions, in the form of overlapping 'bulk' and 'rim' Sm-Nd ages, and tight clustering of Lu-Hf ages even though samples exhibited different Lu zoning profiles and distributions between their cores and rims, respectively (see also Skora et al. (2006)). This refutes the possibility that garnet cores grew significantly earlier than their rims somewhere along the prograde path. One garnet age from Kini reported by Kendall (2016) was removed from the final compilation because of its extremely low radiogenic component and therefore large uncertainty.

White mica Ar/Ar has potential to capture timing of metamorphism during fabric development. However, this system is highly susceptible to disequilibrium, partial (re-) crystallization and mixed ages, and/or unpredictable loss or gain of radiogenic products, making it difficult to interpret the geological significance of an age (Bröcker et al., 2013; Laurent et al., 2016; Lister & Forster, 2016; Maluski et al., 1987). For the final dataset, we only included five Ar/Ar step-heating ages with strong plateaus from micro-drilled grains which all had clear micro-textural context (Laurent et al., 2017), and one strong plateau age from a well-characterized marble shear zone (Rogowitz et al., 2014). We acknowledge that in other HP terranes, even strong plateau ages have been previously attributed to excess Ar (Sherlock & Arnaud, 1999). However, the Ar ages included in this study overlap within reported error of independent Rb-Sr isochrons from rocks at the same locality and/or similar structural levels, which suggests that at least locally, excess Ar is absent (or apparently absent; cf. Ruffet et al. (1995)). *Rb-Sr isochrons* are typically considered

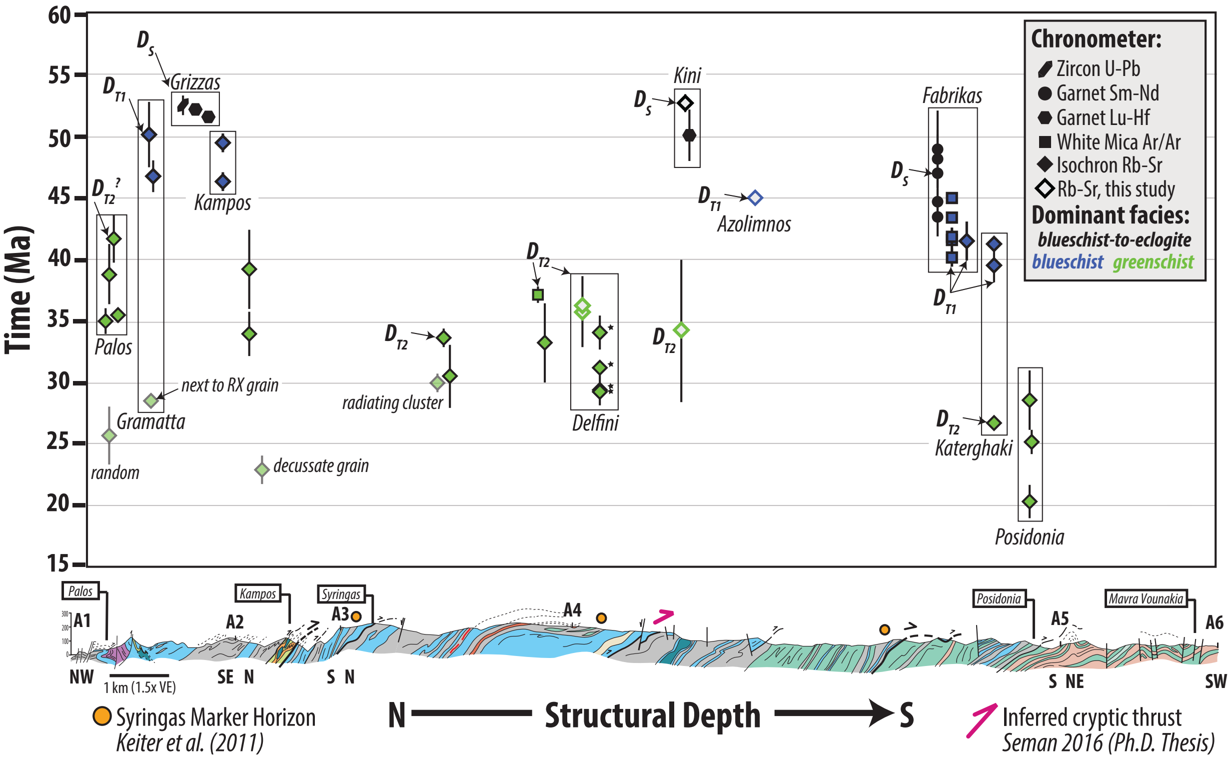

Figure 10: Metamorphic age vs. structural depth for the Syros nappe stack. The cross-section line A1-A6 is shown in Figure 2 and modified from Keiter et al. (2011). Only locations that crop out on the cross section line are labeled in white boxes; in the upper panel, other locations are indicated that project into or out of the page at the structural level shown (e.g. Kini is a normal fault-bounded block on the west side of the island and therefore is not shown on the cross section). Only ages that were confidently linked to the deformation scheme outlined in this paper are included. Clusters of ages outlined in black boxes are derived from the same locality, and collapse onto a single point on the cross section. Delfini symbols marked with stars were reported as blueschist-facies fabrics by Cliff et al. (2016); however, local preservation of glaucophane under greenschist facies conditions can be due to CO_2-bearing fluids. Pink half arrows mark the locations of inferred imbricate ductile thrusts; black half arrows indicate interpreted nappe-delimiting ductile shear zones, which were likely reworked as extensional structures during exhumation.

good indicators of fabric ages when the selected fabrics, and minerals defining them, are well-characterized (Bröcker & Enders, 2001; Bröcker et al., 2013; Skelton et al., 2019). Furthermore, constructing a Rb-Sr isochron directly tests the assumption that selected minerals were in isotopic equilibrium during metamorphism, which validates interpretation of Rb-Sr ages as deformation-metamorphism events. Micro-drilling of white micas and co-genetic Sr-rich phases (epidote or calcite) also provide strong textural context for regressed ages (Cliff et al., 2016).

In some cases, we propose different interpretations of published data based on our own structural observations. Skelton et al. (2019), for example, interpreted three of their Rb-Sr isochrons from Fabrikas as peak metamorphic ages (i.e., D_S), but we interpret Fabrikas fabrics to relate to D_{T1-2}, associated with early exhumation (cf. Fig. 4K). This revised interpretation is supported by previous petrologic observations of eclogite breakdown to blueschist, replacement of glaucophane by actinolite, and core-to-rim decrease in celadonite component of foliation-forming phengitic white mica (Kotowski & Behr, 2019; Laurent et al., 2018) (see also Fig. 7), and structural studies that interpret Fabrikas to record dominantly extensional top-to-the-E, exhumation-related deformation immediately beneath the Vari Detachment. Furthermore, top-E extensional kinematics at Fabrikas clearly contrast with other localities where prograde, top-S-SW deformation is preserved (compare stereonets for Kini with Fabrikas in Fig. 4). Cliff et al. (2016) analyzed micro-drilled phengites from blueschist-to-greenschist facies (i.e., D_{T1} to D_{T2}) extensional fabrics in calc-schists and quartz-mica schists. Four of their samples from Delfini were described as blueschist-facies (black stars in Fig. 10); however, our observations point to penetrative greenschist facies deformation at Delfini (D_{T2}). Glaucophane is locally preserved in abundance in calc-schists at Delfini, and elsewhere on Syros. Rather than reflecting blueschist facies conditions during deformation, this could be due to a glaucophane-stabilizing, CO_2-bearing fluid under greenschist facies P-T conditions (Kleine et al., 2014), or channelized fluid flow at lithological boundaries leading to heterogeneous retrogression (Breeding et al., 2003). Finally, Rogowitz et al. (2014) dated phengites from a top-E extensional greenschist facies marble shear zone, and hypothesized the ages would be Miocene in accordance with the regional 'M2'. They interpreted their Eocene ages as evidence that Miocene deformation did not reset the isotopic signature. However, our results suggest their ages capture a true Eocene recrystallization event (e.g., strong E-W stretching during greenschist facies D_{T2}).

In Figure 10, the refined compilation (n=43) and new Rb-Sr geochronology (n=5) are projected onto the cross-section line drawn in Figure 2. Where possible, ages are labeled according to fabric generation. Faded data points were assigned textural identities but do not record penetrative strain (e.g., randomly oriented, radiating cluster). Key observations from new and compiled geochronology include:

1. D_S, blueschist-to-eclogite facies deformation-metamorphism spans ∼53 to ∼45 Ma, and is captured by a multi-mineral Rb-Sr isochron (this study, Kini), and Lu-Hf and Sm-Nd garnet ages
2. D_S ages are oldest and well-clustered at Grizzas and Kini (∼53-52 Ma), and younger and potentially more widespread at Fabrikas (∼48-42 Ma).
3. D_{T1}, retrograde blueschist facies deformation-metamorphism spans ∼50-40 Ma (Rb-Sr isochrons and Ar/Ar single grain analyses) and youngs with structural depth, i.e., from Kampos, to Azolimnos, to Fabrikas.
4. D_{T2}, retrograde greenschist facies deformation-metamorphism spans ∼42-20 Ma (all Rb-Sr) and youngs with structural depth, i.e., from Palos (∼43-35 Ma), to Delfini (∼35-28 Ma), to Posidonia (∼28-20 Ma).
5. Rocks that presently occupy different structural levels developed distinct fabric generations contemporaneously. Examples include: Fabrikas D_S and Kampos D_{T1} (∼50-45 Ma), Fabrikas D_{T1} and Palos D_{T2} (∼43-38 Ma), and Posidonia D_{T2} and non-penetrative greenschist metamorphism in the north (faded symbols, ∼25-20 Ma). In other words, retrograde blueschist and greenschist facies deformation-metamorphism occurred first in the structurally highest units and progressed structurally downwards with time.

7 Synthesis of structural and petrologic data and interpreted Deformation-Metamorphism history

7.1 D_R P-T conditions

We interpret the D_R fabric as the oldest recognizable in the CBU, and that it formed under lawsonite-blueschist facies conditions based on several lines of evidence: (1) D_R inclusion trail mineralogy (e.g., glaucophane, omphacite, phengite); (2) pseudomorphs of D_{R-S} lawsonite included in D_S garnets from meta-basites on Syros (also seen on Sifnos) (Okrusch

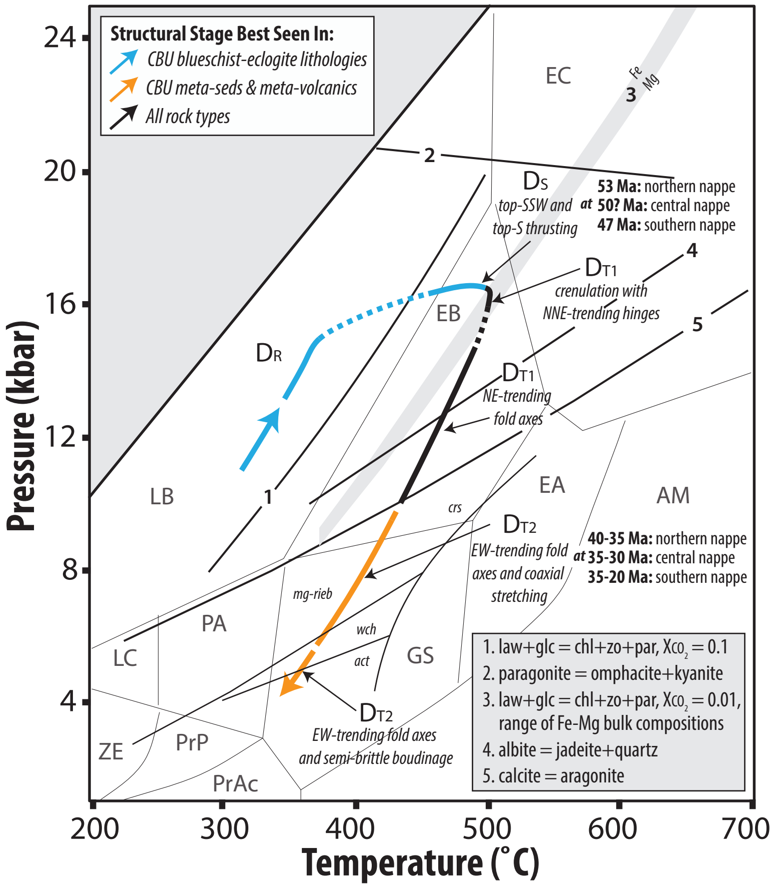

Figure 11: Preferred, schematic P-T-D-t path for the CBU, consistent with observations and analytical results from this study. The shape of the path is modified from Schumacher et al. (2008). Amphibole stability fields constraining D$_{T2}$ temperatures are from Otsuki and Banno (1990). The timing of metamorphism labeled along the P-T loop corresponds to progressive subduction and exhumation of three distinct tectonic slices (the northern, central, and southern nappes; see Sections 6, 7 and Fig. 10). Mineral abbreviations: crs = crossite (sodic amphibole), mg-rieb = magnesio-riebeckite, wch = winchite, act = actinolite. Facies fields defined in Figure 3.

& Bröcker, 1990; Ridley, 1982); and (3) syn-kinematic D$_{R-S}$ omphacite blasts recording up-pressure, core-to-rim zonations marked by increasing jadeite component (Fig. 7A) (cf. Thompson, 1974). Lawsonite and epidote appear to have both been stable in mafic bulk compositions during D$_R$, with lawsonite growing later on the prograde path under higher-pressure conditions (cf. Ballevre et al., 2003). This is consistent with textural observations of lawsonite growing late, syn- and post-tectonic with respect to the S$_R$ foliation, incorporating inclusions of garnet (which also grows near peak pressures, cf. Baxter and Caddick (2013); Dragovic et al. (2012, 2015)), and being included by garnet.

7.2 D$_S$ deformation and P-T conditions

Deformation stage D$_S$ captures peak metamorphic conditions, and produced: (1) an axial plane schistosity, S$_S$, associated with tight to isoclinal folds (F$_S$) that fold S$_R$, record asymmetric top-to-the-S-SW sense of shear, and have S-SW-plunging fold axes; (2) SSW-to-S-plunging mineral lineations; (3) a blueschist-to-eclogite facies fabric containing syn-kinematic garnet, omphacite, and (now pseudomorphed) lawsonite porphyroblasts; and (4) chemical zonations in glaucophane and omphacite that record syn-kinematic increase in pressure and temperature. New and compiled metamorphic geochronology demonstrate that different structural levels of the CBU on Syros experienced peak conditions and D_S deformation at different times (i.e. younging with structural depth, cf Fig. 10; discussed further below). However, it appears that each tectonic slice experienced similar P-T trajectories, including peak P-T, despite subducting at different times.

We do not provide new quantitative constraints on D_S metamorphic conditions, but peak P-T for the D_S fabric shown in Figure 11 are consistent with our petrologic observations and previous studies and are justified as follows. Peak temperatures have been calculated from garnet-omphacite major element exchange for mafic blueschists and eclogites (450-550°C) (Laurent et al., 2018; Okrusch & Bröcker, 1990; Rosenbaum et al., 2002; Schliestedt, 1986); the upper limit of glaucophane stability in marble (∼500°C at ∼15-16 kbar; Schumacher et al. (2008)); and calculated lawsonite-out reactions that predict up-temperature, prograde dehydration according to the reaction *lawsonite = epidote + paragonite +* H_2O) at ∼400-500°C over ∼12-20 kbar (depending on bulk rock and fluid composition) (Evans, 1990; Liou, 1971; Philippon et al., 2011; Schumacher et al., 2008) (Fig. 11). Raman Spectroscopy of Carbonaceous Material from graphite schists suggests slightly higher temperatures of ∼540-560°C (Laurent et al., 2018). Observed porphyroblast stability (e.g. lawsonite pseudomorph inclusions in garnets and vice versa), amphibole chemistry, and the volumetric dominance of glaucophane-bearing marbles throughout the CBU on Syros are generally consistent with peak T of ∼500-550°C.

Reported peak pressures for D_S are variable in the literature, and challenging to reconcile. Early conventional thermobarometry suggested peak P of ∼12-18 kbar in mafic blueschists and eclogites (Dixon, 1976; Okrusch et al., 1978; Okrusch & Bröcker, 1990; Schliestedt, 1986). These pressures are supported by recent solid inclusion quartz-in-garnet barometry constraining garnet growth at Kini, Kalamisia, Delfini, and Lotos to ∼13-17 kbar (Behr et al., 2018; Cisneros et al., in press). However, more recent thermodynamic modeling accounting for garnet fractionation suggests rocks reached ∼22-24 kbar (Laurent et al., 2018; Skelton et al., 2019; Trotet, Jolivet, & Vidal, 2001). We consider this unlikely based on the abundance of S_S paragonite and absence of kyanite in meta-mafic rocks, which suggests that the upper stability limit of paragonite at ∼20-23 kbar was not reached (Okrusch & Bröcker, 1990; Schliestedt, 1986; Skelton et al., 2019) (Fig. 11), although we acknowledge that the kyanite-in reaction is strongly dependent on bulk rock composition (cf. Laurent et al., 2018). Large differences in P-T estimates between traditional phase equilibria and recent thermodynamic modeling may reflect arbitrary choices of thin section domains selected as representative bulk compositions (e.g., Lanari & Engi, 2017). This effect has been demonstrated for CBU lithologies on Syros (see Fig. 15 in Laurent et al., 2018) and is especially likely in garnet-bearing rocks, due to the strong disequilibrium effect that garnet exerts on local bulk composition (Lanari et al., 2017; Lanari & Engi, 2017; Lanari & Duesterhoeft, 2018). It is also possible that higher-P conditions are real, but have not yet been sampled by solid inclusion techniques.

7.3 D_T deformation and P-T conditions

D_T represents retrograde deformation under blueschist-to-greenschist facies conditions during exhumation. D_T is distinguished by: (1) transposition of the S_S foliation during formation of upright, open to tight F_T folds and progressive new (S_T) fabric development; (2) lineation orientations that rotate from N-NE (D_{T1}) to E-W (D_{T2}) with progressive strain and (in general) increasing greenschist facies retrogression; (3) dominantly coaxial, but locally non-coaxial deformation; and (4) chemical zonations in amphibole tracking syn-kinematic decrease in pressure and temperature during development of a composite, reworked foliation (e.g. S_S is locally deformed and metamorphosed during D_T).

During D_T, foliation-forming amphiboles transition from glaucophane to (magnesio) riebeckite, to winchite, to actinolite. The progressive decrease of total Al, Na_B, and $(Na+K)_A$ in amphibole indicates that P and T decreased as D_T evolved. Glaucophane coronas that develop around eclogite pods during D_{T1} are chemically similar to syn-D_S glaucophane, and retrogressed glaucophane records decreasing Al^{vi} (KCS53, KCS52B) and Na_B (KCS53) from core to rim, and a minor increase in $(Na+K)_A$ as (Fig. 8, Fig. B1). These signatures indicate decompression and potentially slight warming (Ernst & Liu, 1998; Laird & Albee, 1981; Moody et al., 1983; Raase, 1974; Robinson, 1982), at the subduction-to-exhumation transition.

D_{T2} is characterized by foliation-forming calcic amphiboles, and local relicts of sodic amphiboles are found as inclusions in porphyroblasts. The transition from sodic-to-calcic amphibole recorded here indicates cooling during decompression (Brown, 1977; Ernst & Liu, 1998; Laird & Albee, 1981; Maruyama et al., 1983; Moody et al., 1983; Otsuki & Banno, 1990; Schmidt, 1992; Thompson, 1974) through albite-epidote blueschist facies and eventually greenschist facies conditions (Fig. 11). This P-T trend is supported by the abundance of albite and titanite overgrowths on rutile, boudin neck quartz-calcite oxygen isotope temperatures and quartz-in-epidote inclusion barometry (Cisneros et al., in press), and decreases from core-to-rim in celadonite component of foliation-forming white micas (Laurent et al., 2018). While we cannot rule out an initial phase of isothermal decompression at high pressures, our documented amphibole geochemical zonations support cooling during decompression at moderate pressures and do not support a positive thermal excursion into the epidote-amphibolite facies field (e.g., edenite, pargasite, crossite), as suggested by Laurent et al. (2018), Lister and Forster (2016), and Trotet, Jolivet, and Vidal (2001) P-T-D paths. Notably, Aravadinou et al. (2016) reported syn-kinematic amphibole zonations from retrograde fabrics in the CBU on Sifnos that also support exhumation along a cooling-during-decompression pathway (see also Schmädicke and Will (2003)).

8 A new tectonic model for the CBU on Syros

Here we synthesize protolith age constraints, and our structural, petrologic, and geochronologic data, and propose a revised tectonic model for the CBU on Syros. First we present a pre-subduction configuration, then discuss a stepwise reconstruction capturing progressive subduction, underplating, and exhumation, leading to the three-part tectonic stack exposed on Syros today.

8.1 Pre-subduction configuration

Figure 12 builds on previous work (e.g., Papanikolaou, 1987, 2013; Ring et al., 2010; Van Hinsbergen et al., 2020) and illustrates a highly schematic paleogeographic setting for the CBU on Syros and Southern Cyclades immediately prior to subduction at ∼60 Ma. Peri-Gondwanan Cycladic Basement, cross-cut by Carboniferous magmatism (∼315 on Syros, Tomaschek et al. (2008); 330-305 in Southern Cyclades, Flansburg et al. (2019)), was rifted in the Triassic (∼240 Ma, Keay (1998); Löwen et al. (2015)). Syn-rift bimodal volcanics and sediments intruded and blanketed the hyper-extended margin; these will become the diagnostic marker horizons referred to as banded tuffitic schists and bimodal meta-volcanics mapped by Keiter et al. (2011) (orange and dark grey in Fig. 12; cf. Fig. 2). Rifting was followed by passive margin sedimentation of psammites, debris flows, and carbonates from the Triassic (∼230) through the Cretaceous (∼75 Ma) (Löwen et al., 2015; Poulaki et al., 2019; Seman, 2016; Seman et al., 2017). Carbonates interbedded with clastic sediments may be the protolith for the Syringas Marker Horizon (Keiter et al., 2011). Cretaceous rifting (∼80 Ma, Tomaschek et al. (2003)) dissected the hyper-extended basement and passive margin sedimentary sequence, forming a small oceanic-affinity (backarc?) basin (Bonneau, 1984; Cooperdock et al., 2018; Fu et al., 2012; Keiter et al., 2011).

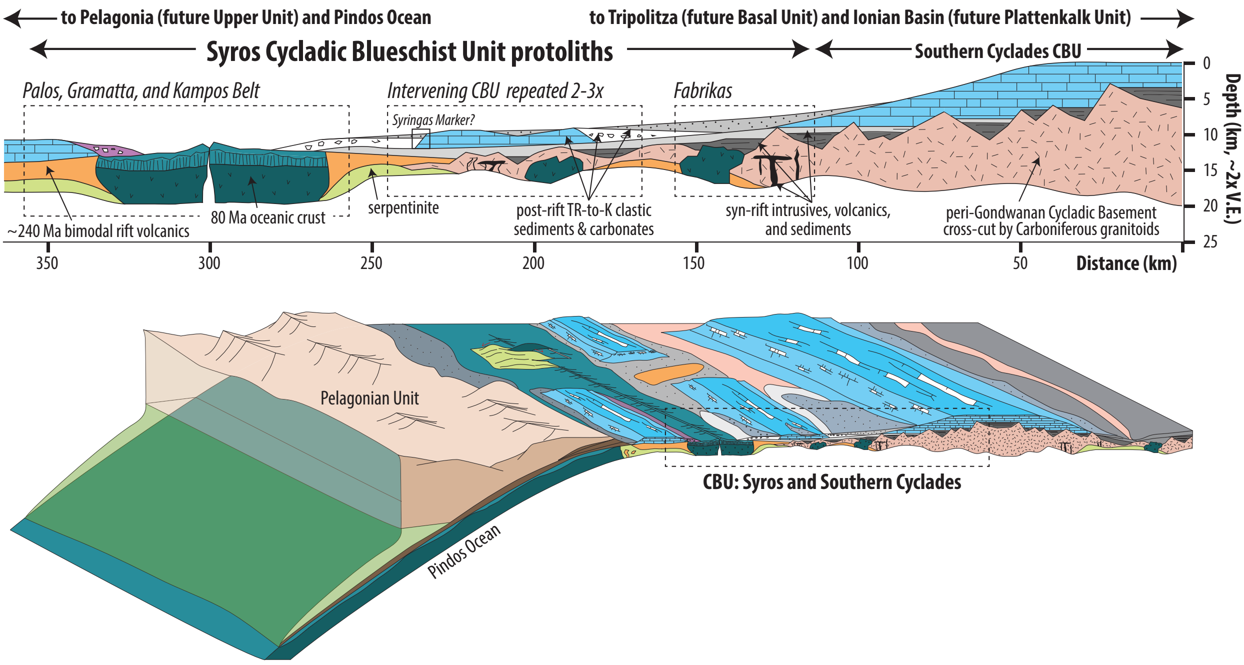

Figure 12: Schematic paleogeographic reconstruction of the CBU, with emphasis on lithologies exposed on Syros at ~60 Ma. The zoomed-in cross section is modified from Seman (2016). Stepwise evolution of the CBU during subduction is shown in the next figure.

The most interpretive part of Figure 12 is the locations of mafic igneous rocks. These rocks could reflect off-axis, shallow intrusions related to Cretaceous rifting, or older mafic igneous rocks related to Triassic rifting; protolith ages have not been determined for Kini, Vaporia, Kalamisia, or Fabrikas mafic rocks. Regardless of their origin, the key point is that protoliths for mafic blueschists and eclogites were distributed throughout the CBU before subduction, rather than only coming from the small ocean basin in the north. While the precise locations and sources of these mafic volcanics are unknown, this interpretation is supported by different ages of peak metamorphism in blueschists and eclogites that crop out at Kampos/Kini and Fabrikas (see Fig. 10 and discussion below).

This paleogeographic interpretation allows us to split the CBU on Syros into three sub-domains characterized by distinct, but related, protolith assemblages (dashed boxes in Fig. 12). These sub-domains are the precursors to each of three main tectonic slices that comprise the structural pile on Syros today.

8.2 Peak subduction of the Palos-Gramatta-Kampos nappe (~53 Ma)

The Palos-Gramatta-Kampos nappe (northern nappe) comprises Cretaceous oceanic lithosphere intruded into Triassic bimodal rift volcanics and Triassic-to-Cretaceous sediments (Fig. 12). Our view of this structurally highest subunit differs from that of Laurent et al. (2016)'s 'Kampos subunit' in that it does not solely comprise meta-mafic lithologies, and it does not include the map-scale meta-mafic lenses at Vaporia, Kalamisia, and Fabrikas (see also Section 9). Garnet Lu-Hf from Grizzas and new Rb-Sr isochrons from Kini yield identical ages of D_S fabric development within error, suggesting that Kini was originally subducted as part of the northern nappe (Fig. 10), and was down-dropped by late-stage, high-angle normal faults to its present position (cf. Keiter et al., 2011; Ridley, 1984).

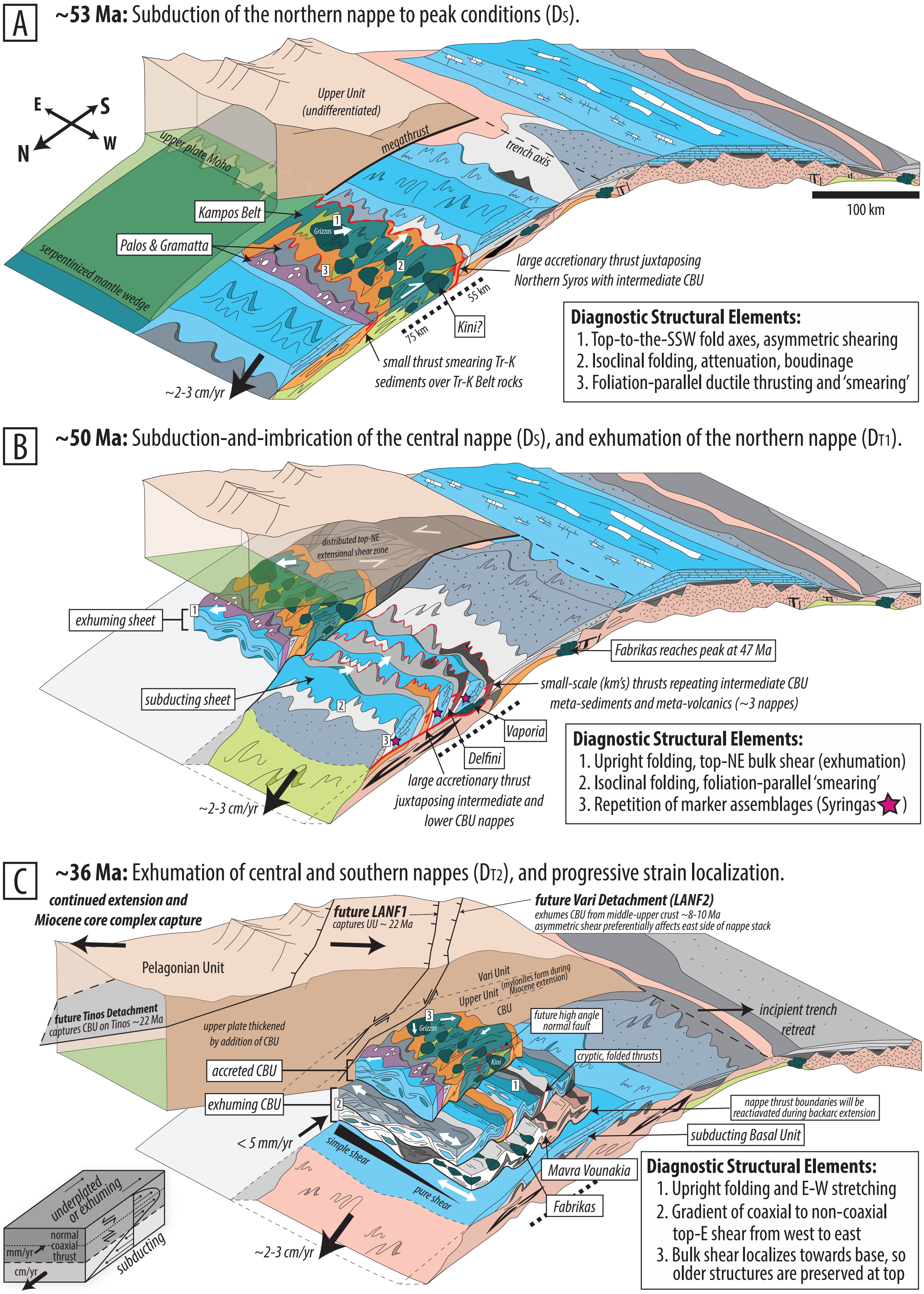

Figure 13: Caption on next page.

Figure 13: (Previous page.) Block diagrams illustrating the structural evolution and timing of subduction and exhumation recorded by the three tectonic slices in the Syros nappe stack. Compare stepwise subduction of sub-units to the paleogeography in Figure 12. Horizontal scaling is equivalent to subduction rates of ~2-3 cm/yr and diagrams are roughly 2x vertically exaggerated. The thickness of the interface is exaggerated for clarity.

Prograde-to-peak subduction was characterized by extremely high top-to-the-SSW asymmetric shear strain and at least two stages of foliation development under blueschist-to-eclogite-facies conditions (D_R and D_S; Fig. 13A). Metamorphism led to the formation of blueschists *and* eclogites under identical P-T conditions, reflecting differences in bulk composition and/or protolith texture (Kotowski & Behr, 2019; Skelton et al., 2019). Subduction-related strain was very heterogeneous. This is evidenced by rheologically strong meta-gabbros at Grizzas and Kini that preserve primary igneous features (Keiter et al., 2004, 2011; Kotowski & Behr, 2019; Laurent et al., 2016). Furthermore, early prograde SW-plunging fold axes and mineral lineations are preserved at Grizzas, Kini, and locally along Kampos Belt. Girdled glaucophane lineations (e.g., Kini, Kampos) record continuous kinematic rotation from SW to N-S during subduction. Top-to-the-SW and top-to-the-S asymmetric thrusting are diagnostic of subduction kinematics (Blake Jr et al., 1981; Keiter et al., 2004; Laurent et al., 2016; Philippon et al., 2011; Ridley, 1984), indicated by SW-verging thrusts on mainland Greece (Jacobshagen, 1986). Despite the extremely high shear strains during subduction, Seman (2016) was able to identify a relict young-on-old depositional relationship preserved between Kampos Belt meta-igneous rocks and the overlying Gramatta meta-sedimentary package. This relationship, seen in the detrital zircon U-Pb geochronologic record, suggests that the contact between the two units has not been substantially disturbed during subduction and exhumation. However, some small-offset ductile thrusting likely 'smeared' the Palos-Gramatta meta-sedimentary rocks along the top of Kampos Belt volcanics (e.g., small thrust in Fig. 13A).

The northern nappe was underplated after D_S development and before D_T exhumation, removing it from the active subduction interface. Detrital zircon U-Pb data support independent structural observations that suggest a large thrust separates the northern nappe from the central nappe beneath it (Keiter et al., 2004; Laurent et al., 2016; Seman, 2016) (Fig. 13A; structurally highest black thrust in cross section in Fig. 10) . This thrust placed Triassic and Cretaceous igneous rocks (Kampos) atop Cretaceous (Syringas) sediments and allowed the underplated nappe to exhume, while subduction of the intermediate nappe occurred beneath it.

8.3 Subduction-and-imbrication of the Syringas-Azolimnos nappe and blueschist facies exhumation of the northern nappe (~50 Ma)

The Syringas-Vaporia-Azolimnos nappe (central nappe) occupies the central portion of the island and comprises interbedded Triassic-to-Cretaceous meta-sedimentary schists, meta-volcanic schists, and meta-carbonates (Fig. 12). In contrast to Laurent et al. (2016)'s central Chroussa subunit, we suggest that Vaporia and Kalamisia meta-mafic lenses belong to this central slice and record primary intrusive and/or depositional relationships with surrounding CBU meta-sediments (cf. Keiter et al. (2011)). The timing of peak D_S during subduction of the central nappe is unknown, but based on this tectonic model and the well-constrained ages of peak subduction in the northern and southern nappes, it likely reached peak conditions at ~50 Ma (this is testable with garnet geochronology from Delfini, Vaporia, or Kalamisia). D_S in the central nappe is largely overprinted during subsequent exhumation-related deformation, but early fabrics are reminiscent of D_S in the northern nappe and similarly consist of isoclinal folds and strong cleavage development (e.g., textural relicts at Azolimnos). While D_S developed in the central nappe, D_{T1} exhumation-related blueschist facies fabrics formed at the same time in the northern nappe (Fig. 10, 13B).

Detrital zircon U-Pb geochronology and Maximum Depositional Ages (MDAs) of meta-sedimentary rocks in the central nappe reveal several old-on-young stratigraphic inversions, which suggest imbrication occurred along cryptic ductile thrusts during subduction (Seman, 2016) (pink thrusts in Fig. 10, pink stars in Fig. 13B). For example, Seman (2016) documented an old-on-young stratigraphic inversion where Triassic meta-volcanics at Delfini are thrust atop Cretaceous meta-sediments east of Kini (Fig. 2). Even though these structures cannot be seen in the field, the presence and locations of inferred thrusts are further supported by the repeated Syringas Marker Horizon, which never appears overturned (orange circles and pink stars in Fig. 10 and 13B, respectively) and repetition of Triassic bimodal meta-volcanic sequences (orange and dark grey in Figs. 2 and 13B). Thus, we propose that the central nappe is bounded by larger nappe-delimiting thrusts to its north and south, and also comprises smaller-scale thrusts accommodating internal imbrication of CBU meta-sedimentary rocks, shown in the cross section in Figures 2 and 10.

During peak subduction of the central nappe (D_S), D_{T1} deformation occurred in the northern nappe, and was characterized by upright folding, crenulation cleavage development, and NE-trending fold axes and mineral lineations. This kinematic transition is marked by ~120-180° rotation in dominant mineral lineations and fold axis orientations from the S-SW to the N-NE. We interpret the crenulation cleavage formed during D_{T1} to be a signature of the 'subduction-to-exhumation transition,' when rocks 'turn the corner' in the subduction channel, based on the observation that crenulation lineations are decorated by high-pressure phases with compositions similar to peak D_S blueschist-to-eclogite facies conditions (Kini, Figs. 6E). D_{T1} and subsequent strain localized in weaker CBU meta-sediments during exhumation (e.g., Palos, Gramatta), whereas prograde subduction-related fabrics are locally preserved in rheologically strong meta-gabbros at Grizzas and Kini. These observations support previous structural studies that suggest exhumation-related deformation progressively localized towards the bottom of the structural pile, leading to more pervasive greenschist facies overprints in the south of the island (Laurent et al., 2016; Lister & Forster, 2016; Ring et al., 2020).

The structural base of the central nappe is difficult to pinpoint. However, metamorphic geochronology suggests that it is somewhere below Azolimnos and must be above the Fabrikas tectonostratigraphic horizon, which comprises the third and lowermost nappe. The presence of a nappe-bounding thrust is also consistent with progressive southward facies changes in the rock types, as carbonate horizons thin substantially and paragneissic material crops out at the island's southern tip, as well as the presence of thrust fault-bounded marble klippe exposed locally on the southern portion of the island (Figs. 2 and 10). Laurent et al. (2016) traced a nappe-bounding shear zone across the island based on the observed intensity of greenschist overprinting and the disappearance of marbles, and suggested its western extent crops out as splaying shear zones above and below the Delfini peninsula (i.e. their 'Achaldi-Delfini shear zone'). If this is the case, then new and compiled geochronology suggests that greenschist facies overprinting in the southern slice spanned ~36-20 Ma. Alternatively, if the nappe-bounding shear zone occupies a slightly deeper structural level (i.e. right beneath Delfini peninsula, such that Delfini represents the lowermost portion of the central nappe that is heavily retrogressed under greenschist facies conditions), then D_{T1-2} development in the central slice is slightly older (~35-30 Ma) than in the southern slice (~30-25 Ma). This ductile nappe-bounding structure accommodated underplating of the central nappe at ~50 Ma while the southern nappe was still subducting, and was subsequently reworked during exhumation.

8.4 Peak subduction of the Fabrikas nappe and blueschist facies exhumation of the central nappe (∼48-43 Ma)

The Fabrikas nappe (southern nappe) comprises Triassic meta-sedimentary schists, meta-volcanic schists, and thinner meta-carbonate horizons compared to the central nappe (cf. Keiter et al., 2011); this meta-sedimentary sequence was spatially associated with mafic igneous rocks with unknown crystallization ages (Fig. 12). The primary difference between our southern slice and Laurent et al. (2016)'s Posidonia subunit is that it contains the Fabrikas meta-mafic lens, which they placed in the structurally highest Kampos subunit. Otherwise, our structural measurements and metamorphic observations are similar. Peak subduction of the Fabrikas nappe is well-constrained at ∼48-43 Ma by garnet Sm-Nd crystallization ages (Kendall, 2016). A weighted mean of Fabrikas garnet ages using Isoplot (Ludwig et al., 2010), weighted by assigned uncertainties, is 45.1±2.9 Ma (2 sigma) (Fig. 10) and is distinctly younger than peak subduction at ∼53 Ma of the northern nappe. The subduction-to-exhumation transition, or underplating event, of the southern nappe is bracketed by peak subduction recorded by garnet Sm-Nd ages and blueschist facies retrogression recorded by Rb-Sr multi mineral isochrons, and occurred somewhere between ∼42-39 Ma (Skelton et al., 2019).

Between ∼48-45 Ma, rocks of the central nappe exhumed in the subduction channel under blueschist facies conditions. Retrograde blueschist fabrics at Azolimnos, well-constrained at ∼45 Ma, overlap with garnet Sm-Nd ages at Fabrikas but are older than retrograde blueschist fabrics at Fabrikas, which directly supports the separation of the central and southern tectonic slices. At this time, mafic blueschists and eclogites and surrounding meta-sedimentary schists in the central nappe developed identical D_{T1-2} structures (e.g., Vaporia and overlying meta-sedimentary rocks, and Kalamisia and Azolimnos; Fig. 4). This indicates that during D_{T1-2}, mafic blueschists and eclogites and surrounding meta-sedimentary rocks were exhumed together, and in some places, strain was partitioned between them. Therefore, even if mafic blueschists and eclogites reached higher pressures on their prograde path, they must have been partially exhumed and juxtaposed with CBU meta-sediments by ∼45 Ma to explain concordant exhumation-related structures.

8.5 Exhumation of the Syros nappe-stack in the subduction channel under greenschist facies conditions (through ∼20 Ma)

Between ∼44-20 Ma, greenschist facies D_{T2} fabrics continuously developed throughout the accreted CBU stack, as each underplated nappe was exhumed in series from north to south. Retrograde greenschist facies deformation-metamorphism occurred first in the structurally highest northern nappe, and migrated structurally downward through time (see also Ring et al. (2020) and Roche et al. (2016)). Exhumation imparted penetrative deformation that progressively transposed older fabrics under blueschist facies (D_{T1}) and eventually greenschist facies (D_{T2}) conditions. Previous geochronology and our new Rb-Sr isochron from Delfini suggest that fabrics formed during blueschist-to-greenschist facies retrogression can be precisely dated if appropriate mineral assemblages are targeted. Furthermore, exhumation-related D_{T1} and D_{T2} strain was dominantly coaxial and well-distributed. This is evident from symmetric strain shadows on garnets, ductile pinching of partially retrogressed eclogites at Agios Dimitrios, and outcrop-scale greenschist facies folds with sub-horizontal E-W trending hinge lines with hinge-parallel symmetric boudinage of competent blueschist and epidote-rich lenses (e.g., Delfini and Lotos; Figs. 5, C1).

The youngest dynamic D_{T2} greenschist facies fabrics associated with subduction channel exhumation are ∼25-20 Ma and are recorded in the southern nappe (Fig. 10). At this time, greenschist facies metamorphism continued in the northern and central nappes, but was not associated with penetrative strain (e.g., random grains, radiating clusters, decussate textures; Cliff et al. (2016)). These observations indicate strain progressively localized towards the base of the stack through time. Patchy, static metamorphism in the northern and central nappes may reflect local fluid availability as deformation migrated structurally downward.

8.6 Upper plate extension and core complex capture

Slab rollback accelerated ~23-21 Ma, which is constrained by dating of detachment faults and supra-detachment sedimentary basins that developed in response to upper crustal extension (Gessner et al., 2013; Ring et al., 2010) . Rollback led to core complex capture and southward migration of the volcanic arc through the former forearc (e.g., the Tinos granite, 14.6 ± 0.2 Ma, Bolhar et al. (2010)). CBU rocks were exhumed in the footwall of the North and West Cycladic Detachment Systems and related smaller-scale structures during 'post-orogenic' exhumation (Jolivet et al., 2010; Soukis & Stockli, 2013). On Syros, the Vari Detachment was reactivated as a semi-brittle to brittle extensional structure and accommodated late stages of exhumation (Fig. 2).

Soukis and Stockli (2013) presented low-temperature zircon and apatite (U-Th)/He thermochronology, and concluded that the southern Syros CBU was juxtaposed with two structurally higher upper-plate units, the Upper Unit (intermediate structural level) and Vari Unit (structurally highest), along at least two semi-brittle detachment faults (Fig. 13C, labeled as future structures). While the Tinos Detachment exhumed CBU rocks between ~22-19 on what would become neighboring Tinos Island, low-angle normal faults juxtaposed the Vari and Upper Units on Syros. Exhumation of the Vari and Upper Units at ~13-15 Ma was roughly coeval with magmatism on Tinos but the Syros CBU exhumed later, ~8-10 Ma, beneath the Vari Detachment (Soukis & Stockli, 2013). Final exhumation of the CBU on Syros occurred in multiple, temporally distinct, rapid episodes of unroofing. Exhumation beneath the Vari Detachment was rapid, but only accommodated the final ~6-9 km of vertical exhumation (Ring et al., 2003).

9 Implications

The tectonic model described above has several similarities and differences compared to previous tectonic models. First, our results agree with previous studies suggesting that Syros is composed of distinct tectonic slices that reached peak conditions at different times (Laurent et al., 2017; Lister & Forster, 2016; Ring et al., 2020; Uunk et al., 2018) . However, while some previous work has identified two slices in the north and south (Ring et al., 2020; Uunk et al., 2018), our data indicate that there may be a third slice in between. The timing of subduction of Fabrikas rocks provides key constraints on how many tectonic slices exist. Skelton et al. (2019) interpreted their Rb-Sr isochrons as records of peak subduction at ~40 Ma, which is younger than garnet crystallization ages presented by Kendall (2016). If Fabrikas did reach peak conditions at ~40 Ma, this supports the inference of a central slice above Fabrikas, because our new Rb-Sr isochron from Azolimnos indicates that rocks occupying a higher structural level above Fabrikas experienced blueschist facies retrogression at ~45 Ma, and therefore must have reached peak conditions before that. If the garnet crystallization ages presented by Kendall (2016) are accurate records of peak subduction of the southern Fabrikas nappe unit (e.g. weighted mean at ~45 Ma), then this also supports the interpretation of an intermediate slice, which was exhuming at the same time as Fabrikas nappe reached peak conditions. Future structural and geochronologic investigations should target garnet-bearing lithologies within the proposed central nappe to constrain the timing of peak subduction in this intermediate structural unit. Our study places quantitative constraints bracketing the timing of subduction of each slice, demonstrates that deformation occurred continuously throughout the Eocene and Oligocene, and illustrates that subduction- and exhumation-related fabrics developed contemporaneously at different structural levels.

Furthermore, we argue that mafic blueschists and eclogites do not exclusively occupy the structurally highest tectonic slice, in contrast to Laurent et al. (2016) and Trotet, Jolivet, and Vidal (2001). Rather, protoliths for mafic blueschists and eclogites were present throughout the CBU before subduction and therefore appear to record primary relationships (cf. Keiter et al., 2011). This implies that the mafic blueschists and eclogites at Vaporia, Kalamisia and Fabrikas are not separated from surrounding schists and marbles by shear zones and/or detachments, as shown for the 'Kampos subunit' of Laurent et al. (2016). The primary observations supporting that Fabrikas cannot belong to the same subducting unit are that Fabrikas meta-volcanics record peak metamorphism that is distinctly younger than that of Kampos and Kini, Fabrikas crops out towards the southern end (i.e. bottom) of the north-dipping structural pile, and Fabrikas meta-volcanics are associated with more meta-carbonate and meta-clastic sedimentary lithologies than Kampos and Kini suggesting they represent subduction of different protolith assemblages. Moreover, the fact that Fabrikas occupies the immediate footwall of the Vari Detachment does not necessarily imply that it belongs to the structurally highest unit. Even though the Vari Detachment has been interpreted as the paleo-subduction channel roof, continuous ductile extension along a shallowly to moderately dipping structure throughout the Eo(?)-Oligocene, in addition to the proposed 6-9 km of semi-brittle exhumation accommodated by $\sim$20 km of localized slip in the Miocene (Ring et al., 2003),can easily explain tectonic removal of the uppermost units. This process would juxtapose structurally deeper CBU units with the Upper Unit in the hanging wall.

Our observations indicate that prograde textures are locally preserved in mafic blueschists and eclogites (cf. Keiter et al., 2004), but the majority of the Syros CBU has been overprinted during subduction channel exhumation (cf. Bond et al., 2007; Rosenbaum et al., 2002; Trotet, Vidal, & Jolivet, 2001). Heterogeneous rock types that occupy a given nappe were subducted and exhumed together, and therefore experienced identical P-T paths (in contrast to Trotet, Vidal, and Jolivet (2001); Trotet, Jolivet, and Vidal (2001)). Therefore, differences in strain, metamorphic mineral assemblages, and/or preserved kinematics between mafic blueschists and eclogites and meta-sedimentary rocks can be attributed to relative strengths, bulk composition, and fluid availability (and composition) during metamorphism (see Schmädicke and Will (2003) for a similar discussion of P-T paths and retrogression of the CBU on Sifnos).

Exhumation from peak depths was accommodated by well-distributed, ductile coaxial thinning throughout the bulk stack (cf. Bond et al., 2007; Rosenbaum et al., 2002) and resulted in penetrative Eocene-Oligocene blueschist and greenschist facies retrogression, unrelated to regional Miocene greenschist facies deformation. Velocity vectors across a dipping planar shear zone (i.e. non-downward tapering) can yield simultaneous subduction and return flow depending on the balance between down-dip shear traction (Couette flow), and up-dip buoyancy (Poiseulle flow) (Beaumont et al., 2009; Raimbourg et al., 2007; Warren et al., 2008; Xia & Platt, 2017), thus giving rise to the subduction channel. Calculated flow vectors predict that subduction imparts non-coaxial shear strain (e.g., Fig. 13A) and immense strain rate gradients across the shear zone, resulting in heterogeneous distributions of finite strain, as documented in blueschist-eclogite lithologies at Grizzas and Kini. Exhumation vectors are characterized by two opposite shear senses that switch across the axis of maximum exhumation velocity (Gerya et al., 2002; Raimbourg et al., 2007; Xia & Platt, 2017). Therefore, in the center of the upward-translating portion of the channel, exhumation is slow and kinematics are effectively coaxial, consistent with the rates and distribution of strain during exhumation of the Syros nappes (Fig. 13B,C).

Non-coaxial deformation on the eastern and southeastern side of the island can be attributed to proximity to the Vari Detachment, which is thought to have operated as the extensional subduction channel roof (Aravadinou & Xypolias, 2017; Laurent et al., 2016; Ring et al., 2020) . Compiled metamorphic geochronology and new Rb-Sr ages allow us to calculate exhumation rates of 1.5-5 mm/yr (= 1.5-5 km/Myr) for each underplated nappe. These rates are roughly an order of magnitude slower than subduction for the Hellenides, and are consistent with buoyancy-driven, channelized return flow in a distributed shear zone (Burov et al., 2014; Gerya et al., 2002; Warren et al., 2008). Furthermore, mm/yr exhumation rates are not consistent with fast rates (comparable to subduction rates) predicted for exhumation along deep-reaching, highly-localized detachments in a downward-tapering 'extrusion wedge' (e.g., Ring & Reischmann, 2002; Ring et al., 2020), nor with forced return flow and melange-like mixing in a low-viscosity wedge (Cloos, 1982; Gerya et al., 2002). Thus, between ∼50 and ∼25 Ma, return flow in the subduction channel accomplished *at least* 35 km, and potentially as much as 55 km of vertical exhumation from maximum depths to the greenschist facies middle crust (∼4 kbar, ∼15 km), accounting for ∼75-80% of CBU exhumation.

On a regional scale, subduction, underplating, and syn-subduction exhumation were fundamental processes during construction of the greater Attic-Cycladic Complex (e.g., Jolivet et al., 2003; Laurent et al., 2017; Lister & Forster, 2016; Ring & Layer, 2003; Ring et al., 2020; Trotet, Jolivet, & Vidal, 2001). CBU rocks on Sifnos have garnet crystallization ages of ∼47-45 Ma (Dragovic et al., 2012, 2015), comparable to the base of the Syros stack. The Basal Unit exposed on Evia and Samos reached peak conditions at ∼24-22Ma (Ring et al., 2001; Ring & Reischmann, 2002; Ring & Layer, 2003), contemporaneous with late stages of syn-subduction greenschist facies exhumation at the base of the CBU on Syros (Fig. 10). The structurally deeper Phyllite-Quartzite Nappe and Plattenkalk unit exposed on Crete experienced HP/LT metamorphism between ∼24-20 Ma (Seidel et al., 1982; Thomson et al., 1999), which also overlaps with latest stages of greenschist facies exhumation on Syros (Fig. 10). Extension and core complex capture that initiated during trench rollback reworked the ACC to its present configuration, and locally reactivated nappe-bounding thrusts as extensional structures (e.g., Vari Detachment on Syros).

10 Conclusions

Structural analysis, metamorphic petrology, and new and compiled geochronology demonstrate that exhumed HP/LT rocks on Syros Island (Cyclades, Greece) record progressive subduction, underplating, and return flow of three separate tectonic slices. Each nappe records a similar structural and metamorphic history, despite subducting at different times. Prograde subduction and underplating of each tectonic slice was characterized by asymmetric top-to-the-SSW and top-to-the-S shear strain, and was reached at ∼53-52 Ma (northern nappe), ∼50 Ma? (central nappe) and ∼47-45 Ma (southern nappe). Prograde deformation and metamorphism is locally preserved in the northern and central nappes, but the majority of the island's meta-sedimentary lithologies were retrogressed during syn-orogenic blueschist-to-greenschist facies exhumation. The subduction-to-exhumation transition in each nappe is marked by systematic kinematic changes: dominant transport directions rotated from roughly N-S (syn-subduction), to NE (post-underplating, at the subduction-to-exhumation transition), to E-W (return flow) and the strain geometry switched from asymmetric to coaxial. Progressive subduction of structurally deeper nappes occurred contemporaneously with exhumation of structurally higher nappes throughout the Eocene and Oligocene, capturing syn-subduction exhumation in the Hellenic subduction channel shear zone. Subduction channel return flow proceeded at ∼1.5-5 mm/yr, which is an order of magnitude slower than subduction, and accounted for ∼80% of the vertical exhumation of the CBU. Continuous subduction, punctuated underplating, and syn-subduction exhumation appear to be fundamental processes during construction of the Attic-Cycladic Complex in the Central and Southern Cyclades.

Acknowledgments

This work was funded by an NSF Graduate Research Fellowship awarded to A.K., an NSF Career Grant (EAR-1555346) awarded to W.B., an NSF Grant (EAR-1725110) awarded to W.B., J.B., and D.S., a Jackson School Seed Grant awarded to J.B., W.B., and D.S., Jackson School Graduate Research Fellowships awarded to A.K. and M.C, and Ford

Foundation fellowship awarded to M.C. Many thanks to Staci Loewy and Aaron Satkoski (JSG, UT Austin) for help with Rb-Sr chemistry and isotope analyses, James Maner for assistance with the microprobe, and Emily Mixon for help with mineral separation. This project was part of A.K.'s Ph.D. dissertation and benefited from many conversations with Mark Cloos and Spencer Seman. The authors are grateful to Valentin Laurent and Uwe Ring for thoughtful and constructive reviews that improved this manuscript. The data that support the conclusions of this article are presented in the main text and in the supporting information. Quantitative microprobe analyses are available on the EarthChem repository (https://doi.org/10.26022/IEDA/111827). Structural data and Rb-Sr geochronologic data are available on the ETH repository (https://doi.org/10.3929/ethz-b-000463143). The authors declare no conflicts of interest.

Appendix A Geochronology

A1 Rb-Sr Methods and Sample Descriptions

Cm-sized pieces of rock were cut out from hand samples to isolate specific fabrics corresponding to progressive stages of deformation-metamorphism as outlined in Section 5. Samples were crushed with a small hammer between sheets of paper, and ground gently with a mini metal rock crusher to separate mineral aggregates. Samples were sieved and separated by grain size. Grain size fractions 125-250 μm and 250-500μm were frantzed to separate minerals based on magnetic susceptibility. The first pass was done with strongest magnetic setting ($\sim$1.8 Amperes) to remove all non-magnetics (e.g., quartz). Subsequent passes were done starting at the lowest setting where minerals started to magnetically separate (typically $\sim$0.2-0.4 A); separates were repeatedly passed through the Frantz at increments of $\sim$0.1-0.2 A. Magnetic fractions were then cleaned by hand, by either negative or positive picking of phases of interest, including garnet, glaucophane, epidote, and white micas (and apatite and chlorite for retrograde fabrics). White mica separates were cleaned of inclusions by gently smearing them in a mortar and pestle and washing them through a sieve with ethanol. SY1616 was collected from float blocks at Kini Beach immediately beneath in-place blueschist-to-eclogite facies cliff faces. The sample is representative of D_S in blueschist-eclogite lithologies. The foliation is defined by glaucophane, epidote, phengite, paragonite, and rutile, with porphyroblasts of garnet and omphacite. Glaucophane, epidote, omphacite, and phengite define the lineation. A similar rock type is shown in Figure 7A. The prograde fabric was targeted for geochronology.

KCS1617 was collected from Azolimnos (approximate location: 37° 24'43.86"N, 24° 57'55.42"E). The sample records an older D_S cleavage cross-cut by the D_{T1} upright crenulation. The mineral assemblage includes glaucophane, epidote, quartz, phengite, paragonite, garnet, rutile, titanite, and oxides. The D_{T1} fabric was cut out of the sample using a diamond-tipped rock saw and targeted for geochronology.

KCS1621 was collected from the southern side of Delfini Beach (approximate location: 37°27'14.61"N, 24°53'51.23"E). The sample is representative of D_{T2}. The foliation is defined by quartz, phengite, paragonite and the lineation is defined by porphyroblasts of epidote and actinolite. This sample is interbedded with quartz-rich schists that have a blue amphibole lineation decimeters to meters above and below. The greenschist-facies fabric was targeted for geochronology.

SY1402 was collected from Lotos (approximate location: 37°26'36.64"N, 24°53'48.87"E). The sample is representative of D_{T2}, during penetrative greenschist-facies deformation and transposition of older fabrics, and some rocks surpass the ductile-to-brittle transition. The sample collected for geochronology is a reaction rind at the margin of a brittlely boudinaged epidote-rich lens, and includes actinolite, chlorite, epidote, phengite, paragonite, and apatite. SY1644 was collected from the southern side of Delfini, very close to KCS1621. The sample is representative of D_{T2}, as rocks locally surpass the ductile-to-brittle transition. Minerals collected for geochronology were precipitated within the boudin neck of a brittlely boudinaged epidote-rich lens including actinolite, epidote, white mica, and calcite.

A2 Compilation and treatment of previous geochronology on Syros

Figure A1 and Table A2 show a compilation of published metamorphic geochronology for the island of Syros (through 2019), comprising 185 individual published ages from 16 studies and 5 chronometers. Applying filters discussed in Section 6.2 to the dataset shown in Figure 3B reduces the compilation from 89 (excludes igneous zircon) to 44 data points, which are plotted in Figure 10. The refined dataset comprises 65 individual ages (some presented as weighted means) that include 44 single-grain analyses and 21 isochrons. The single-grain analyses include 6 ^{40}Ar/^{39}Ar white mica (Rogowitz et al., 2014; Laurent et al., 2017), 37 ^{87}Rb/^{86}Sr white mica (Cliff et al., 2016), and 1 U-Pb SHRIMP zircon age

Sample ID and Summary	Phases defining the isochron	Initial Sr	Age	Uncertainty	MSWD	n
SY1616: Kini omphacite-epidote blueschist	paragonite-phengite	0.7032083	53.53	0.17	1	2
	glaucophane-phengite	0.7032228	53.29	0.17	1	2
	omphacite-phengite	0.7032158	53.41	0.17	1	2
	garnet-phengite	0.703212	53.47	0.21	1	2
	epidote-garnet-phengite	0.7032199	53.34	0.15	0.91	3
	epidote-omphacite-phengite	0.7032198	53.34	0.14	0.64	3
	epidote-garnet-omphacite-phengite	0.7032183	53.36	0.14	0.56	4
	glaucophane-omphacite-garnet-phengite	0.7032179	54.37	0.14	0.46	4
	omphacite-paragonite-garnet-phengite	0.7032121	53.47	0.14	0.28	4
	paragonite(x4)-phengite	0.7031964	53.73	0.13	1.4	5
	** ep-glauc-omph-parag-grt ** NO PHENG	0.703221	59.07	8.57	1.7	5
KCS1617: Azolimnos glaucophane-mica blueschist	epidote-phengite	0.7066671	45.14	0.05	1	2
	glaucophane-phengite	0.7065696	45.61	0.1	1	2
	paragonite-phengite	0.7065964	45.48	0.05	1	2
	paragonite-phengite-phengite	0.7065992	45.47	0.05	0.41	3
	glaucophane-phengite-phengite	0.7065829	45.56	0.61	8.8	3
	epidote-phengite-phengite	0.706643	45.23	0.05	31	3
	** glaucophane-paragonite(x4) ** NO PHENG	0.7066026	43.44	0.76	10	5
	paragonite(x4)-phengite	0.7065951	45.48	0.13	9.4	5
	8 point isochron (all data, except garnet)	0.7066036	45.43	0.04	23	8
KCS1621: Delfini actinolite-mica greenschist	** paragonite-chlorite ** NO PHENG	0.7066492	35.64	0.39	1	2
	paragonite-chlorite-phengite	0.7066201	37.04	0.015	13	3
	** epidote-chlorite-paragonite ** NO PHENG	0.7066492	35.64	0.39	7.90E-25	3
	epidote-phengite-phengite	0.7067163	36.9	0.03	6.30E-24	3
	epidote-chlorite-phengite(x2)	0.7066195	37.06	0.02	21	4
	epidote-paragonite-phengite(x2)	0.7066498	37.02	0.02	9.8	4
	** epidote-chlorite-paragonite(x3) ** NO PHENG	0.7066471	36.19	0.29	7.9	5
	paragonite(x3)-phengite(x2)	0.7066348	37.05	0.014	16	5
	chlorite-paragonite(x3)-phengite(x2)	0.7066266	37.06	0.013	16	6
	epidote-chlorite-paragonite(x3)-phengite(x2)	0.7066266	37.06	0.013	13	7
	8 point isochron (all data)	0.7065941	36.91	0.013	440	8
SY1644: Delfini mineralization in epidosite boudin neck	epidote-white mica	0.7066098	36.16	0.03	1	2
	actinolite-white mica	0.7067006	35.94	0.03	1	2
SY1402: Lotos reaction rim around epidosite pod	apatite-phengite1	0.704965	36.49	0.01	1	2
	apatite-phengite2	0.704965	35.94	0.01	1	2
	apatite-phengite3	0.704965	33.18	0.011	1	2
	apatite-phengite4	0.704966	29.43	0.014	1	2

Table A1: Evaluating the robustness of Rb-Sr ages. Various isochrons are calculated for each sample discussed in-text, for different combinations of (assumed) co-genetic phases. MSWD values are a reflection of anaytical uncertainty and the goodness of fit of all data points on a given isochron; therefore, any two-point isochron by definition has an MSWD of 1.

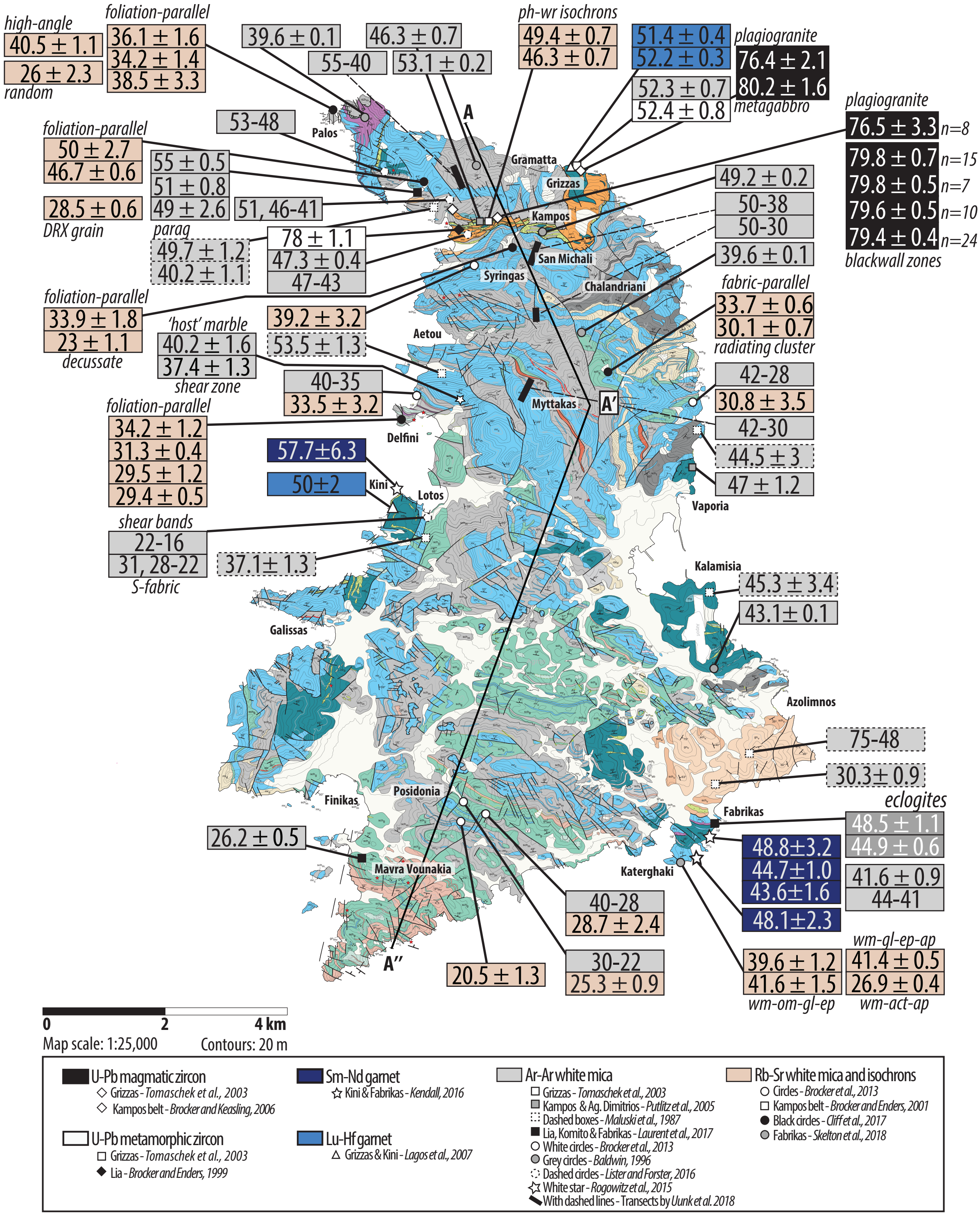

Figure A1: Compilation of the locations and ages from published metamorphic geochronology (and magmatic ages from Kampos), from references listed in grey box and discussed in Section 2. Samples are projected onto the cross-section line A-A'-A" as shown in Figure 10. Sample locations are coded by color and shape according to citation, and box colors around reported ages correspond to different chronometers. Abbreviations for boxes with notes indicating the sample's micro-structural and/or lithologic context are as follows: DRX = dynamically recrystallized; wm=white mica, ph=phengite, om=omphacite, gl=glaucophane, ep=epidote, act=actinolie, ap=apatite, wr=whole rock.

#	Method	Closure Temp	Sample Name and Description	GPS Coordinates^	Location	Age	Uncertainty	Notes	Interpretation*	Ref.
1	**U-Pb zircon**	>750˚C	metagabbro		Grizzas	80.2	1.6		magmatic crystallization (protolith)	[1]
2			meta-plagiogranite dyke		Grizzas	76.4	2.1		magmatic crystallization (protolith)	[1]
3			meta-plagiogranite breccia		Grizzas	52.4	0.8	skeletal rims, low Th/U	HP metamorphism	[1]
4			1081 omphacitite		Kampos belt	78	1		interpreted as HP met, but likely magmatic	[2]
5			4017 plagiogranite in meta-gabbro	37°29.704'N, 024°54.005'E	Kampos belt	77	1	oscillatory zoned zircons	interpreted as HP met, but likely magmatic	[3]
6						76.1	1.2			[3]
7						76.6	1.3			[3]
8						76.6	1.1			[3]
9						76.9	1.1			[3]
10						75	1.2			[3]
11						76.1	1.3			[3]
12						78	1.1			[3]
					average	76.5	3.3			
13			3148 Jadetite: albite + jadeite; accessories	37°29.362'N, 024°54.335'E	Kampos belt blackwall zone	80.3	0.9	oscillatory zoned zircons (likely		[3]
14			titanite, allanite, zircon, white mica, chlorite,			78.7	0.9	magmatic, or seafloor		[3]
15			apatite			80.0	0.9	metasomatism)		[3]
16						78.6	0.7			[3]
17						78.2	0.8			[3]
18						80.6	0.8			[3]
19						78.6	0.7			[3]
20						79.4	0.9			[3]
21						80.7	0.7			[3]
22						79.9	0.7			[3]
23						80.6	0.7			[3]
24						79.8	0.6			[3]
25						77.3	1.4			[3]
26						80.8	0.7			[3]
27						82.9	2.2			[3]
					average	79.8	3.8			
					reported weighted mean	79.8	0.7			
28			3149 Omphacitite: omph, alb, wm, ttn, chl,	37°29.362'N, 024°54.335'E	Kampos belt blackwall zone	79.7	0.5	oscillatory zoned zircons (likely		[3]
29			opaques			79.9	0.3	magmatic, or seafloor		[3]
30						78.5	0.8	metasomatism)		[3]
31						78.4	0.4			[3]
32						76.7	0.5			[3]
33						79.9	1.0			[3]
34						77.6	1.0			[3]
					average	78.7	1.8			
					reported weighted mean	79.8	0.5			
35			3151 Glaucophanite: glaucophane; subordinate	37°29.362'N, 024°54.335'E	Kampos belt blackwall zone	78.9	0.8	oscillatory zoned zircons (likely		[3]
36			amounts of omph, rt, ttn, zrc, all, wm, bt			79.9	0.8	magmatic, or seafloor		[3]
37						78.9	1.2	metasomatism)		[3]
38						79.1	1.2			[3]
39						82.2	1.3			[3]
40						80.0	0.8			[3]
41						78.4	0.7			[3]
42						79.2	0.7			[3]
43						80.3	0.9			[3]
44						80.6	1.0			[3]
					average	79.8	3.0			[3]
					reported weighted mean	79.6	0.5			
45			3152-A Chlorite Actinolite Zone: chl, act, rt,	37°29.362'N, 024°54.335'E	Kampos belt blackwall zone	77.5	1.8	oscillatory zoned zircons (likely		[3]
46			zrc, wm, ap			80.4	1.3	magmatic, or seafloor		[3]
47						82.3	2.0	metasomatism)		[3]
48						78.5	1.1			[3]
49						80.4	2.1			[3]
50						77.7	1.4			[3]
51						78.2	1.3			[3]
52						79.7	0.7			[3]
53						81.3	1.1			[3]
54						80.0	1.8			[3]
55						78.9	1.1			[3]
56						84.0	3.7			[3]
57						79.9	1.0			[3]
58						81.1	0.8			[3]
					average	80.0	6.2			
59			3152-B Chlorite-Actinolite Zone:	37°29.362'N, 024°54.335'E	Kampos belt blackwall zone	76.2	1.3	oscillatory zoned zircons (likely		[3]
60						81.3	1.0	magmatic, or seafloor		[3]
61						79.5	1.0	metasomatism)		[3]
62						78.4	1.1			[3]
63						76.9	1.3			[3]
64						73.1	0.7			[3]
65						79.6	0.5			[3]
66						79.3	1.3			[3]
67						78.5	0.8			[3]
68						79.1	0.7			[3]
					average	78.2	3.2			[3]
					reported weighted mean	79.4	0.4			
69	**Sm/Nd garnet**	600-700˚C	06MSY-6E rutile-bearing eclogite		Kini	57.7	6.3	8 grt-leachate-wr isochron	garnet growth	[4]
70			14RSY-8A mica-rich eclogite		Fabrikas	48.8	3.2	4 grt-wr isochron	garnet growth	[4]
71			14BSY-35D mica-rich eclogite, float		Fabrikas	48.1	2.3	bulk; grt-grt-grt-wr isochron	garnet growth	[4]
72			14BSY-35D mica-rich eclogite, float		Fabrikas	47.1	3	rim of garnet, microdrilled; rim-rim-rim pwd-matrix isochron	garnet growth	[4]
73			14BSY-38A, eclogite boudin in quartz schist matrix		Fabrikas	44.7	1	5 grt-wr isochron	garnet growth	[4]
74			14BSY-37A eclogite, float		Fabrikas	43.6	1.6	5 grt-wr isochron	garnet growth	[4]
75	**Lu/Hf garnet**	600˚C	Ag31: meta-igneous breccia		Grizzas	52.2	0.3	wr-zrn-ttn-'leftover'-4grt isochron; table top digestion	early garnet crystallization (Lu fractionation)	[5]

Table A2: Compilation of published metamorphic geochronology for Syros Island. Data are plotted against closure temperature in Figure 3B. References: (1) Tomaschek et al. (2003), (2) Bröcker and Enders (1999), (3) Bröcker and Keasling (2006), (4) Kendall (2016), (5) Lagos et al. (2007)...

76			Ag85: meta-igneous breccia		Grizzas	51.4	0.4	wr-omph-'leftover'-4grt isochron; table top digestion	early garnet crystallization (Lu fractionation)	[5]
77			Ap21: glaucophane eclogite		Kini	50	2	wr-omph-'leftover'-3grt isochron; table top digestion	early garnet crystallization (Lu fractionation)	[5]
78	**Rb-Sr WM**	~500˚C +/- 50	5243 Ph-Chl-Ab-Qz-Ep-Cal-Ttn-Gr schist	N 37˚ 23.501' E 24˚ 54.633'	South Central, Posidonia	28.7	2.4	ph-cal isochron	ages record continuous (partial) resetting of isotopic systematics and/or (re)crystallization of white mica during exhumation and greenschist facies retrogression	[6]
79	**& isochrons**		5244 Ph-Chl-Ab-Qz-Ep-Cal-Ttn schist	N 37˚ 23.265' E 24˚ 54.365'	South Central, Posidonia	20.5	1.3	ph-ep-ab isochron		[6]
80			5246 Ph-Pg-Chl-Ab-Qz-Ep-Cal-Ttn schist	N 37˚ 23.643' E 24˚ 54.151'	South Central, Posidonia	25.3	0.9	ph-ep-cal isochron		[6]
81			5267 Ph-Chl-Ab-Qz-Cal-Ttn schist	N 37˚ 27.734' E 24˚ 53.898'	N. Delfini	33.5	3.2	ph-cal isochron		[6]
82			SYR015 Ph-Pg-Chl-Ab-Qz-Ep-Cal-Ttn schist	N 37˚ 27.497' E 24˚ 56.767'	N. of Agios Dimitrios	30.8	2.9	ph-par-ep isochron		[6]
83			5831 Ph-Chl-Ab-Qz-Ep-Cal-Ttn-Act schist	N 37˚ 28.808' E 24˚ 54.723'	Syringas (S. of Kampos)	39.2	3.2	ph-ep-ab-cal isochron		[6]
84			1081 Omphacitite		Kampos belt	49.4	0.7	ph-wr isochron	interpretation not provided in text; likely crystallization and/or incipient recrystallization	[7]
85			1083 Omphacitite		Kampos belt	46.3	0.7	ph-wr isochron		[7]
86			63286 - calcschist, cal-ph-glc-qz-ab		Palos, Diapori	35.2	1	4 fabric-parallel phengites, 1 randomly oriented aggregate, 2 calcite	Purposefully targeted extensional blueschist- and greenschist-facies fabrics. Phengites were microdrilled from specific microstructures in calc schists and metabasites. Interpreted as "continuous deformation on a regional scale" and exhumation-related (re-)crystallization.	[8]
87						37.4	0.8	*single phengite*		[8]
88						34.4	0.8	*single phengite*		[8]
89						37.5	1.7	*single phengite*		[8]
						36.1	**1.6**	mean of above 4 grains		
90						26	2.3	*randomly oriented phengite*		[8]
91			63297 - calcschist, cal-ph-glc-ep-qz-ab		Palos, Diapori	35.6	0.5	4 fabric-parallel phengites, 1 grain at high angle to fabric, 3 calcite		[8]
92						32.2	0.3	*single phengite*		[8]
93						34.6	1.1	*single phengite*		[8]
94						34.4	0.5	*single phengite*		[8]
						34.2	**1.4**	mean of above 4 grains		
95						40.5	1.1	*high angle phengite, wrapped by foliation-parallel phengites*		[8]
96			63300 - calcschist, cal-ph-glc-chl-qz-ab		Palos, Diapori	41.8	2	4 fabric-parallel phengites, 1 calcite		[8]
97						37.1	0.4	*single phengite*		[8]
98						40.5	0.4	*single phengite*		[8]
99						34.4	0.5	*single phengite*		[8]
						38.5	**3.3**	mean of above 4 grains		
100			63287a - calcschist, cal-ph-grt-dol-glc-qtz-ep-ttn		Grammata	52.5	0.8	6 fabric-parallel phengites, 4 calcite		[8]
101						52.1	1.1	*single phengite*		[8]
102						46.9	2.3	*single phengite*		[8]
103						48.6	0.5	*single phengite*		[8]
						50	**2.7**	mean of above 4 grains		
104			63287b			47.1	0.6	*single phengite*		[8]
105						46.2	1.3	*single phengite*		[8]
						46.7	**0.6**	mean of above 2 grains		
106			63287a			28.5	0.6	*single phengite; has fine grained recrystallized phengite next to it*		[8]
			S97/234 - greenschist, ab-chl-ph-ep-qz-cal, rare glc		N. Oros Syringas			4 fabric-parallel phengites + 3 ep; 1 grain from decussate pressure shadow adjacent to garnet		
107						33.6	0.4	pseudomorph		[8]
108						29.4	2.3	*single phengite*		[8]
109						34	0.5	*single phengite*		[8]
						33.9	**1.8**	weghted mean of above 3 grains		
110						23	1.1	*decussate phengite*		[8]
111			63301 - greenschist, qz-ph-chl-ab-cal-dol-ttn-ap-pg		Foinikia	30.1	0.7	*decussate/radiating cluster at high angle to fabric*; plus 2 cal + 2 ttn		[8]
112						33.7	0.6	*composite fabric-parallel sample*		[8]
			63310 - blueschist, ep-glc-ph-cal-qz-ab-ttn-tour-chl		Delfini			2 phengite composite samples		
113						31.3	0.4	aligned with schistosity; 3 ep + 2 cal		[8]
114						29.5	1.2	*composite #2*		[8]
115			63314 - blueschist, ph-glc-qz-ep-ttn-chl-ab-cal-ap		Delfini	34	1.7	8 fabric-parallel phengites, 1 epidote, 1 apatite, 2 ttn, lots of ep inclusions		[8]
116						39.5	3.1	*single phengite*		[8]
117						33.9	1.2	*single phengite*		[8]
118						36.3	1.3	*single phengite*		[8]
119						34.3	1.2	*single phengite*		[8]
120						33.7	0.6	*single phengite*		[8]
						34.2	**1.3**	regression of above six grains w. epidote		
121						29.7	0.7	*single phengite*		[8]
122						29.2	0.7	*single phengite*		[8]
						29.4	**0.5**	weighted mean of youngest grains		
				GPS points approximated from map, not provided in text						
123			15-SY-03 glaucophane eclogite	37°23'20.99"N 24°57'13.35"E	Fabrikas	39.6	1.2	4wm-omph-glauc-ep isochron	Interpreted as peak metamorphism, but probably 'reworked' during exhumation	[9]
124			15-SY-05 glaucophane eclogite		Fabrikas	41.6	1.5	4wm-omph-glauc-ep-ap isochron		[9]
125			15-SY-01-02 epidote blueschist	37°23'17.66"N 24°57'9.50"E	Fabrikas	41.36	0.45	4wm-glauc-ep-ap isochron		[9]
126			17 FB 05 greenschist		Fabrikas	26.9	0.4	wm-act-ap isochron	greenschist recrystallization	[9]
127	**Ar/Ar WM**	~400-450˚C	AG144 and BSY260 meta-plagiogranite dyke & breccia		Grizzas	52.3	0.7	Ar steps yield apparent ages between 30-54 Ma	prograde crystallization?	[1]
128		550˚C (Ref. 11)								
129			SY01 metachert		North of Delfini	53.5	1.3		prograde?	[10]
130			SY15 metatuff		North of Ag. Dimitrios	44.5	3		(partial) resetting and/or recrystallization	[10]
131			SY30F eclogitic metagabbro		W. Kampos belt	40.2	1.1		(partial) resetting and/or recrystallization	[10]
132			SY501 omphacitic metagabbro		North of Fabrikas	30.3	0.9		(partial) resetting and/or recrystallization	[10]
133			SY7 calcschist-metatuff		East of Kini	37.1	1.3		(partial) resetting and/or recrystallization	[10]
134			SY66 omphacitic metagabbro		Airport	45.3	3.4		(partial) resetting and/or recrystallization	[10]
135			SY08 calcschist		W. Kampos belt	49.7	1.2	paragonite	Prograde? Or partial resetting?	[10]
136			SY20 metagranite		Vari	48 to 75		no Eocene HP history in Vari Unit	Metamorphic crystallization	[10]
137			S07-14 Grt-Omph blueschist	37.4992/24.8935	Grammata	50.84	0.84	single grain (2)	peak conditions	[11]

Table A2: Continued. References: (6) Bröcker et al. (2013), (7) Bröcker and Enders (2001), (8) Cliff et al. (2016), (9) Skelton et al. (2019), (10) Maluski et al. (1987), (11) Laurent et al. (2017)...

138				49.44	2.62		peak conditions	[11]
139	S07-16 Grt-Chl micaschist	37.4992/24.8935	Grammata	55.04	0.56	concentrate	peak conditions	[11]
140	S07-01 Gln-Ep micaschist	37.3891/24.9534	Fabrikas	41.65	0.95	single grain	recrystallization	[11]
141	S07-02 Blueschist	37.3891/24.9534	Fabrikas	43.51	0.56	single grain (2)	recrystallization	[11]
142				41.95	0.77		recrystallization	[11]
143	S07-04 Gln eclogite	37.3891/24.9534	Fabrikas	44.89	0.65	single grain	recrystallization	[11]
144	S07-04bis Gln eclogite	37.3891/24.9534	Fabrikas	40.29	0.73	single grain	recrystallization	[11]
145	S07-jojo Gln eclogite	37.3891/24.9534	Fabrikas	48.5	1.1	in situ (10), inverse isochron from eclogitic foliation and blueschist shear band combined (ages not resolvably different)	recrystallization	[11]
146	S07-17 Alb-Chl micaschist	37.3791/24.8819	NW of Komito Beach	26.12	0.52	single grain	recrystallization	[11]
147	5267 Ph-Chl-Ab-Qz-Cal-Ttn schist	N 37˚ 27.734' E 24˚ 53.898'	N. Delfini	35-40		10 grains	Ar ages span 41-27; Rb-Sr ages span 34-20	[6]
148	SYR015 Ph-Pg-Chl-Ab-Qz-Ep-Cal-Ttn schist	N 37˚ 27.497' E 24˚ 56.767'	N. of Agios Dimitrios	28-42		12 grains, excludes 1 outlier	Ages record continuous (partial) resetting of isotopic	[6]
149	5243 Ph-Chl-Ab-Qz-Ep-Cal-Ttn-Gr schist	N 37˚ 23.501' E 24˚ 54.633'	South Central, Posidonia	28-40		12 grains	systematics and/or (re)crystallization of white mica	[6]
150	5246 Ph-Pg-Chl-Ab-Qz-Ep-Cal-Ttn schist	N 37˚ 23.643' E 24˚ 54.151'	South Central, Posidonia	22-30		13 grains	during exhumation and greenschist facies	[6]
151	89646 quartzite		Palos	39.6	0.1	total fusion age, gradient in apparent ages 31 to 41.2	partial loss profile and/or recrystallization after HP eve	[12]
152	89644 glaucophane-marble schist		Kampos belt	53.1	0.2	phengite, total fusion age, graident 52.4 to 55	HP event	[12]
153	89642 retrograde eclogite		Kampos belt	49.2	0.2	phengite, flat spectra, weighted mean	HP event	[12]
154	89645 retrograde blueschist		Central	39.6	0.1	total fusion age, gradient 34.8 to 42.4	partial loss profile and/or recrystallization after HP event	[12]
155	89649 retrograde blueschist		Airport	43.05	0.12	total fusion age, gradient 40 to 44.2	partial loss profile and/or recrystallization after HP event	[12]
156	SY-7 phengite-rich eclogite		Kampos belt	46.3	0.7	in-situ UV-laser ablation; weighted mean laser fusion ages (n=27)	paper says prograde; could be partially reset, some ages are older (50-52)	[13]
157	SY-25 omphacite-rich meta-gabbro		Agios Dimitrios	47	1.2	in-situ UV-laser ablation; weighted mean laser fusion ages (n=30)	paper says prograde; our observations of Ag. Dim indicate this is likely recrystallization and/or neo-crystallization	[13]
							All ages from [14] are interpreted as crystallization ages related to different microstructures using the 'method of asymptotes and limits'	
158	AG10-31 garnet mica schist	37° 30.081'N 24° 53.173'E	N. of Gramatta	53-48		Δ1B + early Δ1C decussate + post-Δ1C shear zone, pheng-muscovite	timing of Δ1B event	[14]
159	AG10-14 garnet mica schist	37° 29.613'N 24° 54.295'E	N. Kampos belt	51, 46-41		Δ1B + Δ1C + post-Δ1C, older phengite component, younger muscovite component	muscovite component records Δ1C growth and post-Δ1C shearing	[14]
160	AG10-15 Δ1C white mica in boudin neck	37° 29.537'N 24° 54.416'E	Kampos belt	43-47		late Δ1C porphyroblastic white mica, from dilational zone next to mega-boudin		[14]
161	AG10-16 early Δ1C decussate wm + titanite	37° 29.546'N 24° 54.404'E	Kampos belt	47.3	0.4	early Δ1C decussate white mica, from edge of mega-boudin		[14]
162	AG10-26S wm-qz-ab-chl-calc greenschist	37° 26.582'N 24° 54.166'E	E. of Kini, roads above Lotos	31, 28-22		Dominant fabric in greenschist facies schist (post-Δ1D and Δ2)	older phengite component; younger muscovite component	[14]
163	AG10-26C wm-qz-ab-chl-calc greenschist	37° 26.582'N 24° 54.166'E	E. of Kini, roads above Lotos	16-22		Extensional shear bands cutting greenschist fabric (relict post-Δ1D + Δ2 + post-Δ2)	muscovite component	[14]
	Kampos transect - *graphite-rich Lws-Grt blueschists and micaschists, with intercalated calcite and siliceous layers*		N. of Kampos belt			*single grain fusion experiments*		
164	12SR100: graphite-rich Lws-Grt-Gln micaschist, static gscht.	N37° 29.855', E24° 54.369'		55-48		broad uniform age		[15]
165	12SR57: siliceous marble; Phg+Gln+ Ep+Qz+ Ttn+Chl	N37° 29.856', E24° 54.220'		55-48		broad uniform age		[15]
166	12SR02: graphite-rich Lws(ps)-Grt-Gln micaschist; ttn in foliation	N37° 29.942', E24° 54.566'		52-45		wide uniform age		[15]
167	12SR97: Phg+Qz+Ep+Ttn bearing marble	N37° 29.827', E24° 54.628'		52-45		wide uniform age		[15]
168	12SR03: phg-bearing marble with columnar aragonite pseudomorphs	N37° 29.821', E24° 54.744'		55-40		heterogeneous		[15]
	San Michalis transect - *marble-schist-marble sequence, middle unit contains pyrite-bearing schists and gneisses, graphite-rich Lws-Grt-Gln micaschists and quartzitic rocks, locally with static greenschist overprint*		S. of Kampos belt			*single grain fusion experiments*		
169	12SR96: Lws-Grt-Gln micaschist, static gscht	N37°29.393', E24°54.891'		49-45		narrow range		[15]
170	12SR04: Lws-Grt-Gln micaschist, static gscht	N37°29.359', E24°55.125'		48-40		heterogeneous		[15]
171	12SR13b: carbonated and brecciated blueschist; Ctd-Gln, Ep	N37°29.328', E24°55.223'		48-40		heterogeneous		[15]
172	12SR92: Phg-bearing marble; aragonite pseudomorphs	N37°29.395', E24°54.975'		48-40		heterogeneous		[15]
173	12SR93: Phg-bearing marble; aragonite pseudomorphs	N37°29.343', E24°54.904'		50-38		heterogeneous		[15]
	Syringas transect 1 and 2 *- intercalated schist-marble sequence; vary from felsic to Ep-blueschists to pervasively overprinted greenschists*		Sy1 west coast; Sy2 central			*single grain fusion experiments*		
174	12SR78: crenulated felsic mica schist	N37°28.830', E24°53.901'		48-42		narrow uniform age		[15]
175	12SR82: calcschist, Phg+Qz+Chl	N37° 28.666', E24° 55.119'		38-31		intermediate		[15]
176	12SR81: Phg-bearing marble, aragonite pseudon	N37° 28.664', E24° 55.118'		50-40		heterogeneous		[15]
	Myttakas transect *- upper and lower marbles bookending felsic schists and gneisses and intermediate-mafic rocks ranging from ep-grt blueschists to pervasively overprinted greenschists*		NE of Delfini, central			*single grain fusion experiments*		
177	12SR19: Phg-bearing marble	N37°27.889', E24°55.225'		40-39		narrow uniform age		[15]
178	12SR16: Ep-Ab blueschist (+Grt), partial greenschist overprint	N37°27.796', E24°55.147'		40-39		narrow uniform age		[15]
179	12SR20: felsic Ab gneiss; Phg+Qz foliation, Ab porphyroblasts	N37°27.871', E24°55.199'		42-30		heterogeneous		[15]

Table A2: Continued. References: (12) Baldwin (1996), (13) Putlitz et al. (2005), (14) Lister and Forster (2016), (15) Uunk et al. (2018) ...

180	12SR18b: intermediate-to-mafic Grt-Ep blueschist; Phg+Gln+Ep matrix	N37°27.841', E24°55.174'		42-30		heterogeneous		[15]
181	12SR18a: blueschist, static greenschist; Phg+Qz matrix	N37°27.811', E24°55.171'		42-30		heterogeneous		[15]
182	12SR17: greenschist mylonite, fine-grained Act+Chl matrix, Ab blasts	N37°27.798', E24°55.154'		42-30		heterogeneous		[15]
183	12SR15: siliceous marble, Ep+Phg+Qz, aragonite pseudomorphs	N37°27.808', E24°55.101'		42-30		heterogeneous		[15]
184	Calcite marble, host rock	?	N. of Delfini	40.2	1.6	Si apfu 3.4-3.6, EW stretching	Authors hypothesized these would be Miocene due to strong EW stretching. Interpreted Eocene ages as evidence that the phengite was not reset during Miocene deformation; our results suggest these could be DT2 greenschist deformation	[16]
185	Calcite marble, shear zone			37.4	1.3			

Table A2: Continued. References: (16) Rogowitz et al. (2014)

which is a weighted mean of 7 analyses (Tomaschek et al., 2003). The isochrons include 5 Sm-Nd garnet-whole rock (Kendall, 2016), 3 Lu-Hf garnet-omphacite-whole rock (Lagos et al., 2007), 10 multi-mineral and 2 phengite-whole rock ^{87}Rb/^{86}Sr (Bröcker & Enders, 2001; Bröcker et al., 2013; Skelton et al., 2019). . The ^{40}Ar/^{39}Ar ages included in the final compilation are strong plateaus from step-heating experiments of grains extracted from well-characterized microstructural domains (Laurent et al., 2017). We excluded: 1 Sm-Nd isochron with low ^{147}Sm/^{144}Nd ratio and potential for contamination due to the presence of an off-isochron inclusion (cf. Kendall, 2016); 50 ^{40}Ar/^{39}Ar ages, and one 10-pt inverse ^{40}Ar/^{39}Ar isochron that exhibit one or more of the complications described in Section 6.2 (Maluski et al., 1987; Baldwin, 1996; Tomaschek et al., 2003; Putlitz et al., 2005; Bröcker et al., 2013; Lister & Forster, 2016; Laurent et al., 2017; Uunk et al., 2018). We removed the 10-pt isochron from the final compilation because its 10 points combine measurements from an eclogitic foliation and a blueschist cross-cutting shear band which overlap within error, so this age cannot be conclusively interpreted as either peak eclogite facies nor early retrograde blueschist facies. It is likely a mixing line between these two 'events.'

Lagos et al. (2007) presented Lu-Hf garnet growth ages from meta-igneous rocks at Grizzas and Kini, showing that those blueschist-eclogite localities reached peak metamorphic conditions at 51.9±1.4 Ma and 50±2 Ma, respectively. New fabric ages from Kini blueschists (this study, 52.62 ± 0.64 Ma) overlap with garnet growth ages at Grizzas and Kini, and with the SHRIMP age determined by Tomaschek et al. (2003) for Grizzas metamorphic zircons.

Fabrikas eclogites record Sm-Nd garnet crystallization ages of ∼45±3 Ma (Kendall, 2016). 'Bulk' garnet ages (48.1±2.3 Ma) overlap within error with 'rim' ages (47.1±3 Ma), providing evidence for rapid, pulsed garnet crystallization that is distinctly younger than Grizzas and Kini. A weighted mean of Fabrikas garnet ages using Isoplot (Ludwig et al., 2010), weighted by assigned uncertainties, is 45.1±2.9 Ma (two sigma). Garnet growth ages are consistent with ^{40}Ar/^{39}Ar ages of foliation-forming white mica in Fabrikas glaucophane-bearing eclogites (48.5±1.1 Ma to 44.9±0.6 Ma, Laurent et al. (2017)).

Retrograde blueschist-facies fabric ages range from ∼50-40 Ma, and are captured by: (1) Phengite-whole rock Rb-Sr isochrons from omphacitites at Kampos (49.4±0.7 Ma and 46.3±0.7 Ma, Bröcker and Enders (2001)) and Rb-Sr ages of micro-drilled phengites from glaucophane-bearing calcschists at Gramatta (50.5±3.1 Ma and 47.3±1.2 Ma, Cliff et al. (2016)); (2) A new multi-mineral Rb-Sr isochron from Azolimnos (44.71 ± 0.43 Ma, this study); (3) A Rb-Sr isochron from omphacite-blueschists (41.5±1.5 Ma, Skelton et al. (2019)) and ^{40}Ar/^{39}Ar ages of foliation-forming white mica in retrogressed Fabrikas eclogites and bluechists (44.9±0.65 Ma to 40.3±0.7 Ma, n=4, Laurent et al. (2017)).

Retrograde greenschist-facies fabric ages range from ∼42-36 Ma, and are captured by Rb-Sr multi-mineral isochrons and Rb-Sr ages of foliation-forming micro-drilled phengites from greenschists and calcschists from the following locations: (1) Palos (40.5±1.1 Ma to 34.2±1.4 Ma, Cliff et al. (2016)); (2) Syringas (39.2±3.2 Ma, Bröcker et al. (2013); 33.9±1.8 Ma Cliff et al. (2016)); (3) North of Delfini (33.7±0.6 Ma, Cliff et al. (2016); 33.5±3.2 Ma and 30.8±2.9 Ma, Bröcker et al. (2013)); (4) Delfini (34.2±1.3 Ma to 29.4±0.5 Ma; Cliff et al. (2016); 36.47±0.11 Ma, this study); (5) Fabrikas (26.9±0.4 Ma, Skelton et al. (2019)); and (6) Posidonia (28.7±2.4 Ma, 25.4±0.9 Ma, 20.5±1.3 Ma, Bröcker et al. (2013)).

Appendix B Electron Microprobe Techniques and Data Treatment

B1 Qualitative X-Ray Mapping

Qualitative X-Ray compositional maps were acquired on the JEOL JXA-8200 electron microprobe at the University of Texas at Austin. Polished 30 μm thin sections were analyzed using a 15 kV accelerating voltage, focused beam, 300 nA current, 6 μm step size, and 1 ms dwell time. X-ray maps for Si, Al, Ca, Mg, Fe, Na, K, Mn, Ti, and P were collected. Post-

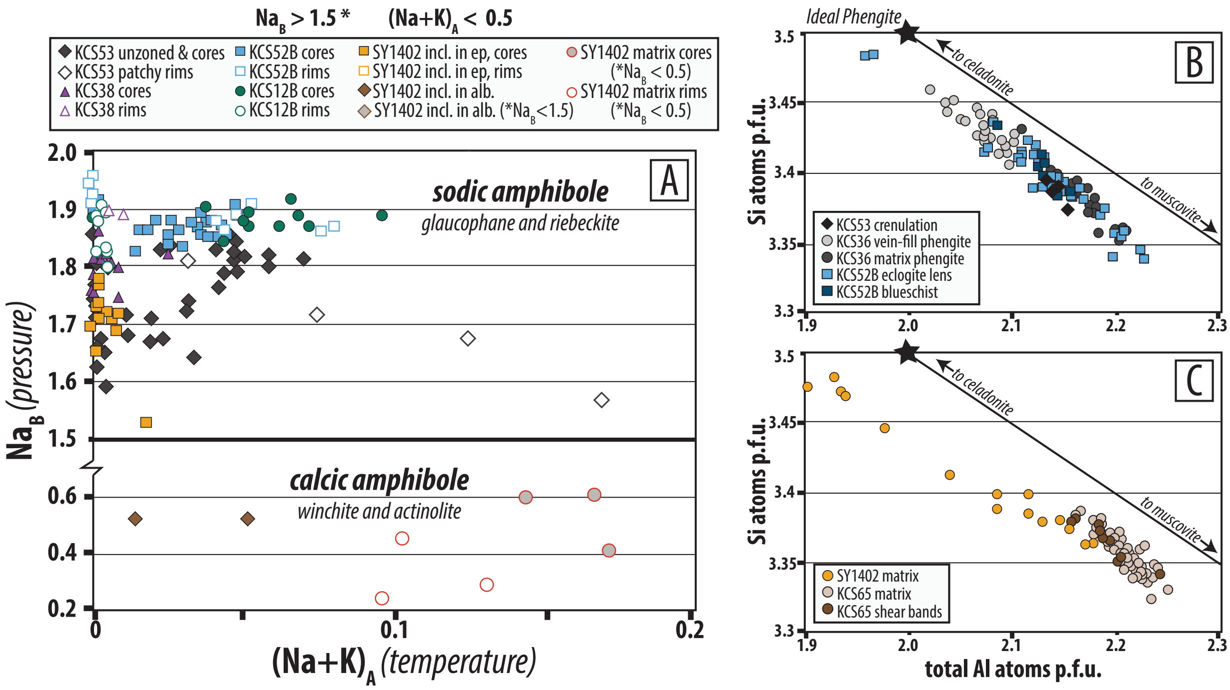

Figure B1: Quantitative EPMA results for (A) amphiboles and (B,C) white micas. (A) Na_B and $(Na+K)_A$ in amphibole are qualitative indicators of pressure and temperature, respectively. Temperature is less reliable since all of these amphiboles are very 'cold' (i.e., crystallize at <500°). Sodic amphiboles correspond to D_S and D_{T1}, and calcic amphiboles correspond to D_{T2}; see text for significance of core-rim zonations and compositional trends during deformation. (B) D_S and D_{T1} white mica chemistry. Elevated Si apfu indicates HP metamorphism. (C) D_{T2} white mica chemistry. Grains cluster towards a lower Si apfu on average, which reflects more pervasive recrystallization under lower P conditions. Intergrown phengite and paragonite is common during all deformation stages. CBU samples do not contain the limiting assemblage required for Si-in-phengite geobarometry calibrated by (Massonne & Schreyer, 1987). However, they do contain other stable Fe-Mg buffering phases (e.g., epidote, amphibole), so within a given sample and between samples of similar bulk compositions, Si variability is a reasonable measure of *relative* changes in pressure, not absolute. Samples in (B) are all meta-mafics, SY1402 in (C) is meta-mafic, KCS65 in (C) is a quartz-rich mixed meta-volcanic/meta-sediment.

processing to produce false color compositional maps creation was done in ImageJ software by merging element channels with assigned colors.

B2 Quantitative Point Analyses

Quantitative analyses were collected for representative amphiboles and micas on the JEOL JXA-8200 electron microprobe at the University of Texas at Austin. Samples were selected to cover the range of interpreted structural contexts determined during field work and microstructural analysis. Polished 30 μm thin sections were analyzed using a 15 kV accelerating voltage, a 1μm beam diameter amphibole and a 10μm beam diameter for mica, 10 nA current, and counting time 30 s for all elements. Synthetic compounds and homogeneous minerals were used as standards, and secondary standards were analyzed throughout analytical procedures. Data were processed using the JEOL ZAF procedure.

Sample:	**KCS53**	***n=30***	**KCS53**	***n=6***	**KCS53**	***n=4***	**KCS53**	***n=10***	**KCS38**	***n=14***	**KCS38**	***n=2***	**KCS52B**	***n=21***	**KCS52B**	***n=4***	**KCS52B**	***n=8***	**KCS52B**	***n=3***
Context:	*matrix cores*		*cren. limb cores*		*cren. limb rims*		*cren. hinges*		*matrix cores*		*matrix rims*		*ecl, cores*		*ecl, rims*		*matrix cores*		*matrix rims*	
SiO2	58.71	0.54	58.67	0.32	57.09	1.04	58.60	0.18	59.25	0.22	58.87	0.30	58.54	0.49	58.07	0.20	58.53	0.33	58.03	0.42
Al2O3	11.23	0.20	11.07	0.05	11.00	0.12	11.07	0.15	11.78	0.26	11.59	0.13	10.83	0.72	10.11	0.10	11.26	0.20	10.72	0.43
K2O	0.01	0.01	0.01	0.01	0.03	0.02	0.01	0.01	0.01	0.01	0.00	0.00	0.00	0.01	0.00	0.00	0.01	0.00	0.00	0.00
Na2O	6.54	0.24	7.06	0.11	6.80	0.29	7.13	0.11	6.93	0.16	7.21	0.04	7.20	0.10	7.13	0.01	7.26	0.09	7.22	0.09
CaO	0.97	0.38	0.80	0.14	1.54	0.87	0.70	0.23	0.91	0.16	0.20	0.01	0.32	0.18	0.13	0.04	0.34	0.12	0.12	0.08
MnO	0.06	0.04	0.04	0.01	0.10	0.05	0.05	0.02	0.03	0.02	0.09	0.01	0.11	0.08	0.19	0.02	0.06	0.03	0.17	0.06
FeO	9.16	0.55	9.02	0.18	10.19	0.53	9.33	0.43	7.71	0.50	11.05	0.53	11.09	2.27	14.25	0.23	9.39	0.79	11.95	0.66
MgO	11.43	0.37	11.64	0.21	11.30	0.62	11.52	0.41	11.65	0.51	9.67	0.28	10.28	1.16	8.68	0.04	11.04	0.50	9.59	0.48
TiO2	0.03	0.03	0.00	0.01	0.02	0.03	0.02	0.03	0.02	0.02	0.03	0.01	0.01	0.02	0.02	0.02	0.01	0.02	0.01	0.02
Cr2O3	0.02	0.02	0.02	0.02	0.00	0.00	0.02	0.02	0.01	0.02	0.00	0.00	0.01	0.02	0.03	0.01	0.02	0.02	0.00	0.01
Total	97.89	0.47	98.30	0.26	98.05	0.13	98.44	0.25	98.29	0.49	98.68	0.26	98.37	0.27	98.58	0.15	97.88	0.31	97.79	0.71
Si	7.96	0.05	7.94	0.03	7.81	0.12	7.92	0.03	7.97	0.05	8.00	0.00	7.97	0.02	7.99	0.02	7.96	0.02	7.97	0.02
Al (iv)	0.04	0.04	0.06	0.03	0.19	0.12	0.08	0.03	0.04	0.04	0.00	0.00	0.03	0.02	0.01	0.02	0.04	0.02	0.03	0.02
K (A)	0.00	0.00	0.00	0.00	0.00	0.00	0.00	0.00	0.00	0.00	0.00	0.00	0.00	0.00	0.00	0.00	0.00	0.00	0.00	0.00
Na (A)	0.01	0.01	0.04	0.01	0.10	0.05	0.05	0.01	0.01	0.01	0.01	0.00	0.02	0.02	0.00	0.00	0.04	0.01	0.01	0.02
Na (B)	1.71	0.06	1.81	0.02	1.70	0.12	1.82	0.03	1.80	0.04	1.89	0.00	1.88	0.04	1.90	0.00	1.88	0.02	1.91	0.04
Ca (B)	0.14	0.06	0.12	0.02	0.23	0.13	0.10	0.03	0.13	0.02	0.03	0.00	0.05	0.03	0.02	0.01	0.05	0.02	0.02	0.01
Mn (B, 2+)	0.01	0.00	0.00	0.00	0.01	0.01	0.01	0.00	0.00	0.00	0.01	0.00	0.01	0.01	0.02	0.00	0.01	0.00	0.02	0.01
Fe (B, 2+)	0.11	0.04	0.07	0.01	0.06	0.01	0.07	0.02	0.04	0.04	0.07	0.00	0.06	0.03	0.05	0.01	0.07	0.02	0.05	0.04
Fe (C, 2+)	0.91	0.06	0.82	0.05	0.91	0.09	0.83	0.08	0.81	0.09	1.16	0.05	1.02	0.19	1.32	0.04	0.89	0.09	1.11	0.05
Fe (C, 3+)	0.02	0.03	0.13	0.04	0.20	0.05	0.16	0.04	0.01	0.02	0.03	0.01	0.19	0.13	0.27	0.05	0.11	0.03	0.21	0.10
Al (C, vi)	1.75	0.05	1.70	0.03	1.58	0.10	1.69	0.04	1.83	0.02	1.85	0.01	1.71	0.09	1.63	0.03	1.76	0.03	1.71	0.04
Mg (C)	2.31	0.07	2.35	0.05	2.31	0.13	2.32	0.08	2.34	0.09	1.96	0.05	2.08	0.22	1.78	0.01	2.24	0.09	1.97	0.08
Type	***Glaucophane***		***Glaucophane***		***Glaucophane***		***Glaucophane***		***Glaucophane***		***Glaucophane***		***Glaucophane***		***Mg-Riebeckite***		***Glaucophane***		***Glaucophane***	

Table B1: Amphibole mineral chemistry. Reported values are averages of the number of spots indicated by n values for each sample and micro-textural context. Uncertainties reflect the range of measured values for each micro-textural context as indicated. Cations per formula unit are calculated for ideal element partitioning for 23 Oxygen atoms.

Sample:	**KCS52B** ***n=6***	**KCS52B** ***n=7***	**KCS12B** ***n=11***	**KCS12B** ***n=8***	**SY1402** ***n=8***	**SY1402** ***n=10***	**SY1402** ***n=1***	**SY1402** ***n=2***	**SY1402** ***n=3***	**SY1402** ***n=2***
Context:	*ps, cores*	*ps, rims*	*matrix cores*	*matrix rims*	*incl. in ep, cores*	*incl. in ep, rims*	*incl. in alb (A)*	*incl. in alb (B)*	*matrix cores*	*matrix rims*
SiO2	58.58 0.20	57.72 0.42	56.32 0.22	54.03 0.63	57.78 0.15	57.30 0.69	58.28	56.52 1.24	54.13 0.26	54.93 0.96
Al2O3	11.35 0.13	10.65 0.44	10.72 0.38	4.92 1.61	8.12 0.87	8.45 1.28	8.05	2.80 0.89	3.12 0.16	2.23 0.60
K2O	0.00 0.01	0.00 0.00	0.00 0.00	0.02 0.01	0.02 0.01	0.03 0.03	0.05	0.19 0.14	0.12 0.03	0.09 0.03
Na2O	7.18 0.06	7.24 0.08	7.09 0.14	6.65 0.22	6.50 0.21	6.39 0.33	6.45	1.89 0.06	2.49 0.40	1.32 0.17
CaO	0.48 0.06	0.24 0.13	0.29 0.11	0.66 0.33	0.73 0.33	0.93 0.88	1.14	8.92 0.23	8.58 0.99	10.80 0.26
MnO	0.05 0.01	0.14 0.06	0.06 0.03	0.14 0.03	0.15 0.07	0.16 0.07	0.21	0.32 0.01	0.40 0.05	0.38 0.03
FeO	9.08 0.27	12.51 1.43	16.93 0.49	25.10 2.03	15.28 1.08	15.55 1.60	14.41	12.24 1.06	15.64 1.74	12.16 0.79
MgO	11.23 0.34	9.45 0.66	6.50 0.20	5.85 0.25	9.74 0.48	9.29 0.87	10.32	14.93 1.43	13.92 1.11	16.77 0.74
TiO2	0.01 0.02	0.01 0.03	0.02 0.03	0.02 0.02	0.02 0.03	0.03 0.03	0.00	0.00 0.00	0.02 0.01	0.01 0.01
Cr2O3	0.00 0.00	0.01 0.02	0.01 0.01	0.00 0.00	0.00 0.00	0.00 0.00	0.00	0.00 0.00	0.00 0.00	0.00 0.00
Total	97.92 0.45	97.93 0.33	97.92 0.29	97.35 0.36	98.33 0.41	98.11 0.62	98.91	97.80 0.85	98.42 0.20	98.69 0.42
Si	7.95 0.02	7.95 0.02	7.93 0.04	7.85 0.04	8.01 0.04	7.98 0.07	8.01	8.01 0.05	7.73 0.06	7.74 0.08
Al (iv)	0.05 0.02	0.05 0.02	0.07 0.04	0.15 0.04	0.01 0.02	0.03 0.05	0.00	0.02 0.02	0.27 0.06	0.26 0.08
K (A)	0.00 0.00	0.00 0.00	0.00 0.00	0.00 0.00	0.00 0.00	0.01 0.00	0.01	0.03 0.03	0.02 0.00	0.02 0.00
Na (A)	0.03 0.01	0.04 0.03	0.05 0.02	0.00 0.00	0.00 0.00	0.00 0.00	0.00	0.00 0.00	0.14 0.02	0.10 0.02
Na (B)	1.86 0.01	1.89 0.03	1.88 0.02	1.87 0.05	1.75 0.05	1.73 0.09	1.72	0.52 0.01	0.55 0.12	0.26 0.03
Ca (B)	0.07 0.01	0.04 0.02	0.04 0.02	0.10 0.05	0.11 0.05	0.14 0.13	0.17	1.35 0.01	1.31 0.15	1.63 0.03
Mn (B, 2+)	0.01 0.00	0.02 0.01	0.01 0.00	0.02 0.00	0.02 0.01	0.02 0.01	0.02	0.04 0.00	0.05 0.01	0.05 0.00
Fe (B, 2+)	0.07 0.02	0.06 0.02	0.07 0.02	0.01 0.01	0.11 0.02	0.10 0.04	0.08	0.05 0.03	0.09 0.03	0.06 0.00
Fe (C, 2+)	0.86 0.06	1.16 0.15	1.74 0.06	1.71 0.06	1.28 0.12	1.35 0.15	1.20	1.36 0.16	1.38 0.16	1.07 0.05
Fe (C, 3+)	0.10 0.03	0.22 0.08	0.18 0.03	1.33 0.28	0.39 0.16	0.36 0.18	0.38	0.03 0.05	0.40 0.05	0.30 0.06
Al (C, vi)	1.77 0.02	1.68 0.06	1.71 0.04	0.69 0.29	1.32 0.13	1.36 0.17	1.31	0.45 0.13	0.26 0.05	0.11 0.03
Mg (C)	2.27 0.06	1.94 0.12	1.36 0.04	1.27 0.05	2.01 0.10	1.93 0.17	2.12	3.15 0.25	2.96 0.23	3.52 0.13
Type	***Glaucophane***	***Glaucophane***	***Riebeckite***	***Riebeckite***	***Mg-Riebeckite***	***Mg-Riebeckite***	***Mg-Riebeckite***	***Winchite***	***Fe-Winchite***	***Actinolite***

Table B1: Continued. Amphibole mineral chemistry. Reported values are averages of the number of spots indicated by n values for each sample and micro-textural context. Uncertainties reflect the range of measured values for each micro-textural context as indicated. Cations per formula unit are calculated for ideal element partitioning for 23 Oxygen atoms.

B3 Mineral classification and formula unit calculations

Quantitative point analyses for amphiboles and white micas were converted from oxide percentage to atoms per formula unit on the basis of 22O + 2OH, and 10O + 2OH Oxygen atoms, respectively. Amphibole sub-groups and species were determined following recommendations of the Commission on New Minerals Nomenclature and Classification (CNMNC) of the International Mineralogical Association (IMA) (Hawthorne et al., 2012), and species names follow the (Leake et al., 1997) classification scheme. Classifications did not assume initial M-site$^{3+}/\sigma$M-site ratios, so ferric iron components were estimated based on charge balance by adjusting valences of Fe and Mn by automatically normalizing the cations. Data shown here commonly fell into the "sum Si to Ca=15", "sum Si to Mg=13", and "sum Si to Na=15" normalization schemes (Hawthorne et al., 2012). Hydroxyl contents were not estimated using OH=2-2Ti, and initial H_2O contents were not required for calculations. White mica ferric iron was ignored in formula calculations.

Appendix C Supplemental Field Photos

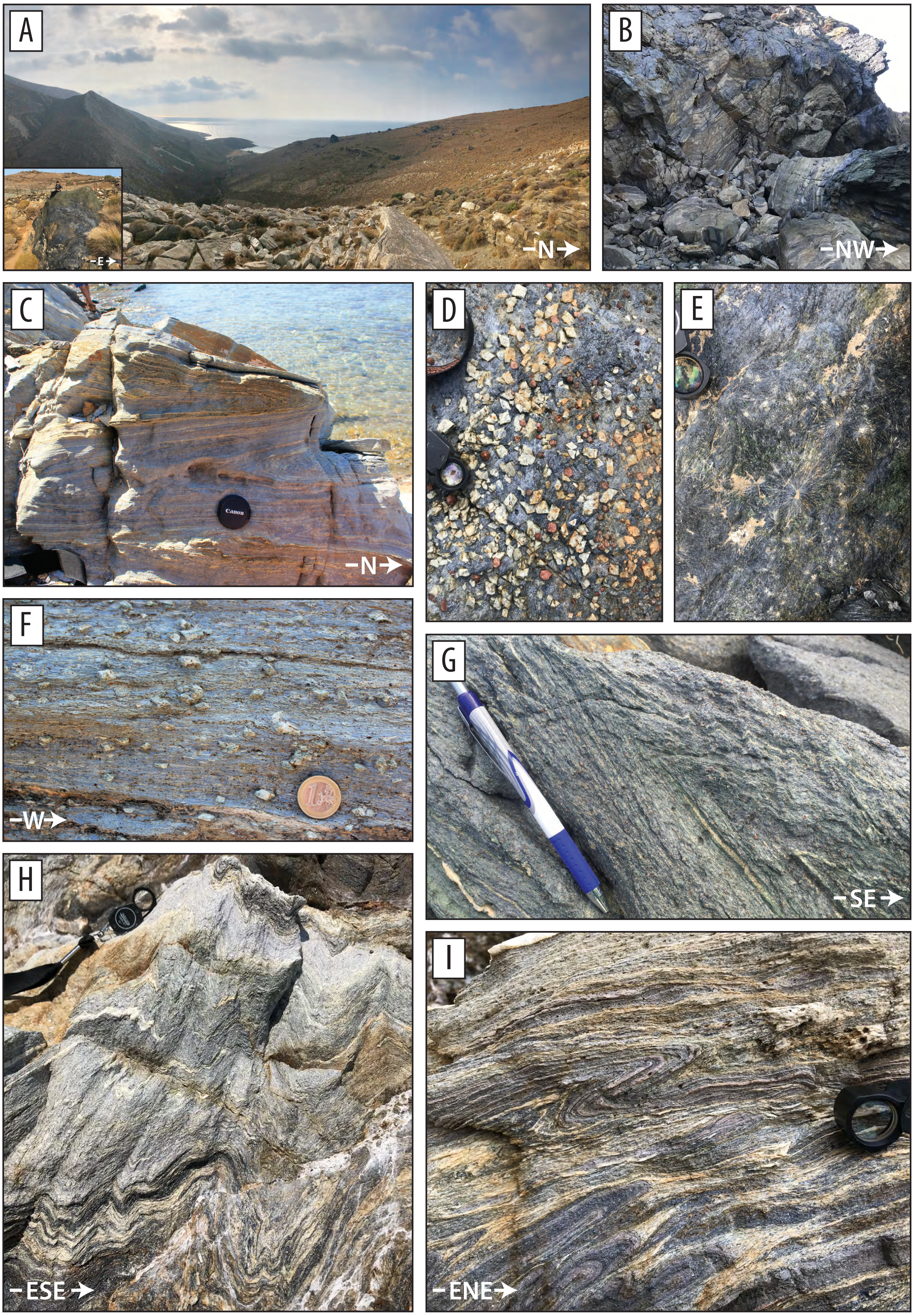

Figure C1: Caption to follow.

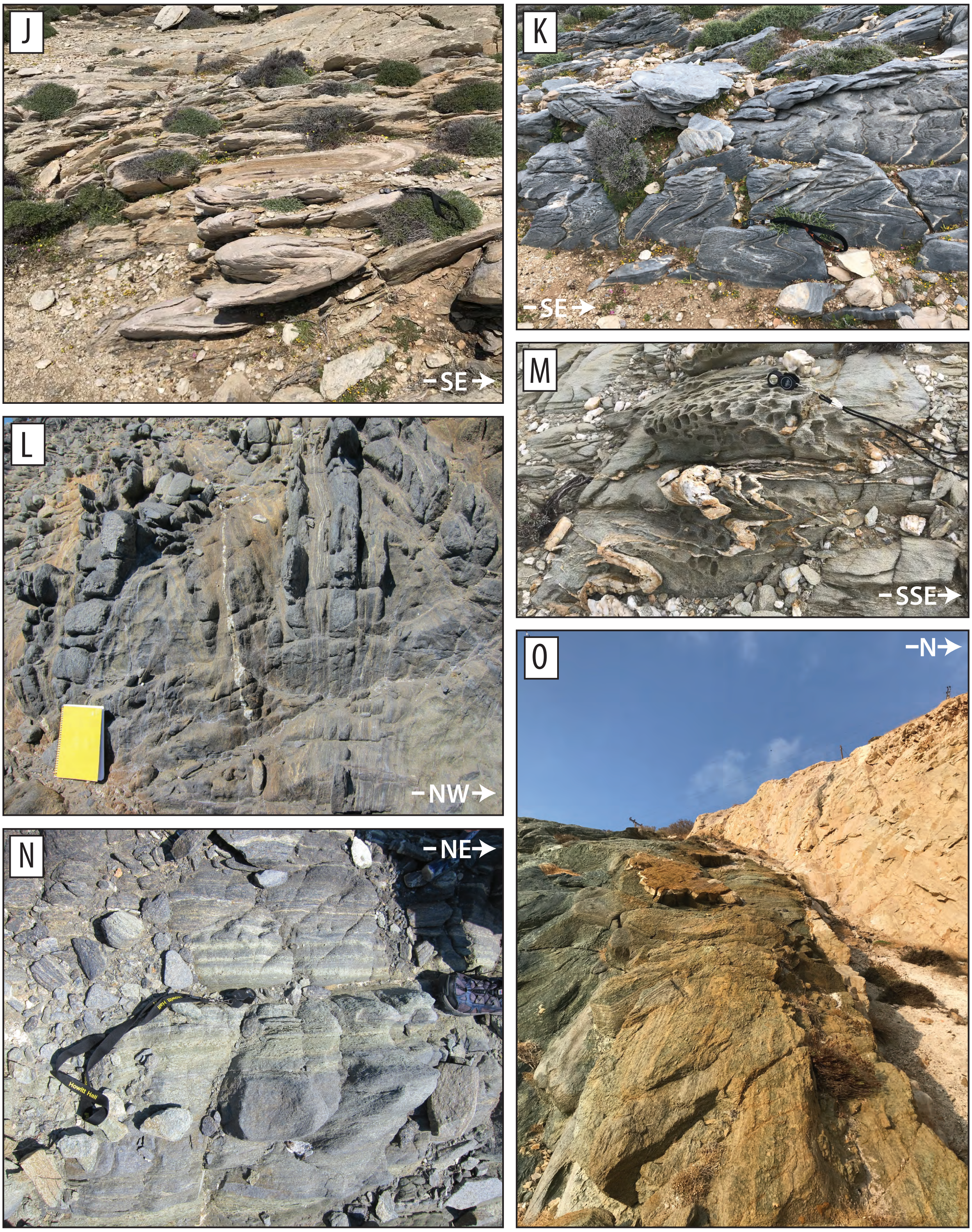

Figure C1: Caption to follow.

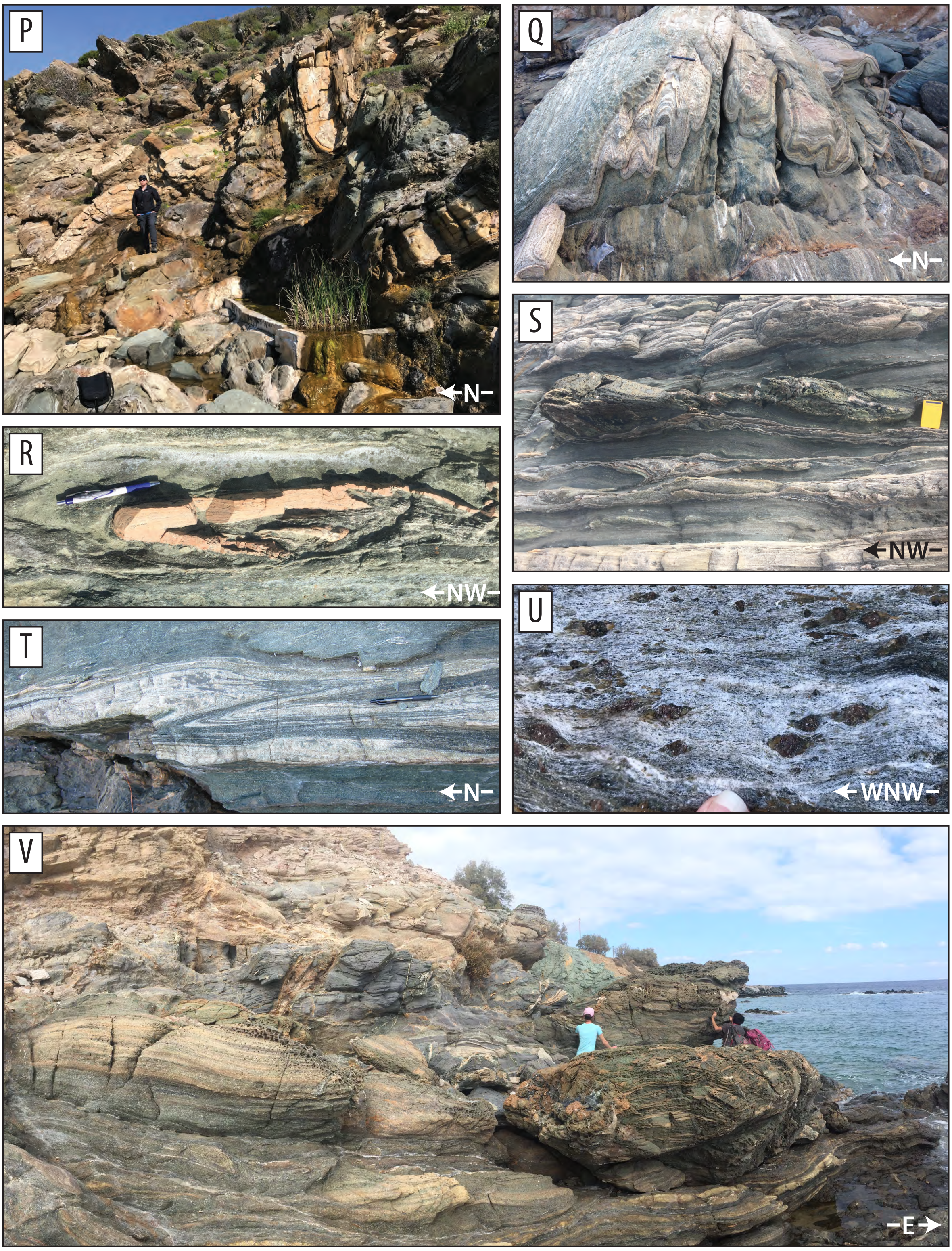

Figure C1: Caption next page.

Figure C1: (Previous pages.) Supplemental field photographs. (A) Eclogitic meta-gabbro 'blocks' pepper the Kampos Belt landscape, and are wrapped by coherent bimodal meta-volcanics (cropping out as resistant ledges in the background). Marbles in the foreground dip down towards the coastline and are structurally concordant with Belt rocks. This is a thrust contact that may have been reworked slightly during exhumation via extension, but we did not see evidence for strongly localized top-to-the-ENE shear. Inset shows example of Kampos meta-gabbro block with glaucophanite carapace. (B) Example of upright, shallowly NNE-plunging D_S folds on the shoreline W of Kampos Belt. (C) Lia Beach isoclinally-folded blueschists; the older, folded foliation is relict D_R, and isoclinal folding developed during D_S. (D) Unstrained cm-sized lawsonite pseudomorphs in Grizzas blueschist. (E) Zoom-in to margin of a Kampos Belt block showing static, radiating clusters of blue and green amphibole. (F) Unstrained D_S lawsonite pseudomorphs in Lia blueschists. (G) D_{T1} crenulation cross-cutting D_S at Kini. (H) The cores of D_{T1} upright folds in Azolimnos schists have strong axial planar cleavages associated with blueschist-to-greenschist facies retrogression. (I) Earlier D_S fabrics in Azolimnos schists record asymmetric shear in isoclinally-folded schists; pinkish layers are meta-cherts. (J) Isoclinal folds in marbles (foreground) and meta-conglomerates (background) and in meta-mafic greenschists (M) on Palos Peninsula mimic the map-scale folding seen in Fig. 2. (K) Sub-horizontal axial planar cleavages form in dolomitic blue-grey marbles during exhumation-related flattening (coaxial strain). (L) Upright D_{T1} folding at Kalamisia is associated with hinge-parallel greenschist retrogression (N) selectively permeating foliation-parallel layers. (O) Fault contact between marbles and blueschist-eclogite lithologies at Agios Dimitrios. Stretching is directly down-dip (essentially out of the page) and parallel to mullion hinges developed along the contact. Structures on either side of this contact are homogeneous. (P-S, U) Multiple generations of folding at Delfini. (P) Upright D_{T2} folding (discussed in text) develops an axial planar cleavage and hinge-parallel stretching and mineral lineations defined by quartz, epidote, and actinolite (Q). Older D_S foliations contain axial planes of isoclinal folds, best seen by salmon-colored meta-cherts (R) and compositional banding (T). Hinge:limb thickness variations locally exceed 20:1 (T, Lotos). (S) Along the limbs of upright folds like (P), coaxial stretching leads to boudinage of competent lenses. These structures record top-WNW shear, but top-ESE structures occur in roughly equal proportions. (U) Symmetric quartz-filled pressure shadows on delta-type D_S garnet porphyroblasts. (V) Asymmetric, non-coaxial strain during exhumation is limited to localities proximal to the Vari Detachment, like this example from Fabrikas.

References

Agard, P., Plunder, A., Angiboust, S., Bonnet, G., & Ruh, J. (2018). The subduction plate interface: rock record and mechanical coupling (from long to short timescales). *Lithos*, *320*, 537–566.

Altherr, R., Kreuzer, H., Lenz, H., Wendt, I., Harre, W., & Dürr, S. (1994). Further evidence for a Late Cretaceous low-pressure/high-temperature terrane in the Cyclades, Greece. *Chemie der Erde*, *54*, 319–28.

Andriessen, P., Boelrijk, N., Hebeda, E. H., Priem, H., Verdurnen, E., & Verschure, R. H. (1979). Dating the events of metamorphism and granitic magmatism in the Alpine orogen of Naxos (Cyclades, Greece). *Contributions to Mineralogy and Petrology*, *69*(3), 215–225. doi: 10.1007/BF00372323

Angiboust, S., Agard, P., Glodny, J., Omrani, J., & Oncken, O. (2016). Zagros blueschists: Episodic underplating and long-lived cooling of a subduction zone. *Earth and Planetary Science Letters*, *443*, 48–58.

Aoki, K., Itaya, T., Shibuya, T., Masago, H., Kon, Y., Terabayashi, M., … Maruyama, S. (2008). The youngest blueschist belt in sw japan: Implication for the exhumation of the cretaceous sanbagawa high-p/t metamorphic belt. *Journal of Metamorphic Geology*, *26*(5), 583–602.

Aravadinou, E., & Xypolias, P. (2017). Evolution of a passive crustal-scale detachment (Syros, Aegean region): Insights from structural and petrofabric analyses in the hanging-wall. *Journal of Structural Geology*, *103*, 57–74.

Aravadinou, E., Xypolias, P., Chatzaras, V., Iliopoulos, I., & Gerogiannis, N. (2016). Ductile nappe stacking and refolding in the cycladic blueschist unit: insights from sifnos island (south aegean sea). *International Journal of Earth Sciences*, *105*(7), 2075–2096.

Avigad, D., & Garfunkel, Z. (1989). Low-angle faults above and below a blueschist belt—Tinos Island, Cyclades, Greece. *Terra Nova*, *1*(2), 182–187.

Avigad, D., & Garfunkel, Z. (1991). Uplift and exhumation of high-pressure metamorphic terrains: the example of the Cycladic blueschist belt (Aegean Sea). *Tectonophysics*, *188*, 357–372.

Baldwin, S. L. (1996). Contrasting PTt histories for blueschists from the western Baja Terrane and the Aegean: Effects of synsubduction exhumation and backarc extension. *Washington DC American Geophysical Union Geophysical Monograph Series*, *96*, 135–141.

Ballevre, M., Pitra, P., & Bohn, M. (2003). Lawsonite growth in the epidote blueschists from the Ile de Groix (Armorican Massif, France): a potential geobarometer. *Journal of metamorphic Geology*, *21*(7), 723–735.

Baxter, E. F., & Caddick, M. J. (2013). Garnet growth as a proxy for progressive subduction zone dehydration. *Geology*, *41*(6), 643–646.

Beaumont, C., Jamieson, R. A., Butler, J., & Warren, C. (2009). Crustal structure: A key constraint on the mechanism of ultra-high-pressure rock exhumation. *Earth and Planetary Science Letters*, *287*(1-2), 116–129.

Behr, W. M., Kotowski, A. J., & Ashley, K. T. (2018). Dehydration-induced rheological heterogeneity and the deep tremor source in warm subduction zones. *Geology*, *46*(5), 475–478.

Behr, W. M., & Platt, J. P. (2012). Kinematic and thermal evolution during two-stage exhumation of a Mediterranean subduction complex. *Tectonics*, *31*(4). doi: 10.1029/2012TC003121

Blake Jr, M. C., Bonneau, M., Geyssant, J., Kienast, J., Lepvrier, C., H., & Papanikolaou, D. (1981). A geologic reconnaissance of the Cycladic blueschist belt, Greece. *Geological Society of America Bulletin*, *92*(5), 247–254.

Bolhar, R., Ring, U., & Allen, C. M. (2010). An integrated zircon geochronological and geochemical investigation into the miocene plutonic evolution of the cyclades, aegean sea, greece: Part 1: Geochronology. *Contributions to Mineralogy and Petrology*, *160*(5), 719–742.

Bolhar, R., Ring, U., & Ireland, T. (2017). Zircon in amphibolites from naxos, aegean sea, greece: origin, significance and tectonic setting. *Journal of Metamorphic Geology*, *35*(4), 413–434.

Bond, C. E., Butler, R. W. H., & Dixon, J. E. (2007). Co-axial horizontal stretching within extending orogens: the exhumation of HP rocks on Syros (Cyclades) revisited. *Geological Society, London, Special Publications*, *272*(1), 203–222. Retrieved from `http://sp.lyellcollection.org/content/272/1/203.abstract` doi: 10.1144/GSL.SP.2007.272.01.12

Bonneau, M. (1984). Correlation of the Hellenide nappes in the south-east Aegean and their tectonic reconstruction. *Geological Society, London, Special Publications*, *17*(1), 517–527. Retrieved from `http://sp.lyellcollection.org/lookup/doi/10.1144/GSL.SP.1984.017.01.38` doi: 10.1144/GSL.SP.1984.017.01.38

Breeding, C. M., Ague, J. J., Bröcker, M., & Bolton, E. W. (2003). Blueschist preservation in a retrograded, high-pressure, low-temperature metamorphic terrane, Tinos, Greece: Implications for fluid flow paths in subduction zones. *Geochemistry, Geophysics, Geosystems*, *4*(1). doi: 10.1029/2002GC000380

Brichau, S., Ring, U., Carter, A., Monie, P., Bolhar, R., Stockli, D. F., & Brunel, M. (2007, jan). Extensional faulting on Tinos Island, Aegean Sea, Greece: How many detachments? *Tectonics*, *26*(4). Retrieved from `papers3://publication/uuid/06DAB232-CF25-4D35-A7EB-F6A69A4DF869`

Bröcker, M. (1990). Blueschist-to-greenschist transition in metabasites from Tinos Island, Cyclades, Greece: compositional control or fluid infiltration? *Lithos*, *25*, 25–39.

Bröcker, M., Baldwin, S., & Arkudas, R. (2013). The geological significance of 40Ar/39Ar and Rb-Sr white mica ages from Syros and Sifnos, Greece: A record of continuous (re)crystallization during exhumation? *Journal of Metamorphic Geology*, *31*(6), 629–646. doi: 10.1111/jmg.12037

Bröcker, M., & Enders, M. (1999, mar). U–Pb zircon geochronology of unusual eclogite-facies rocks from Syros and Tinos (Cyclades, Greece). *Geological Magazine*, *136*(02), 111–118. Retrieved from `http://journals.cambridge.org.ezproxy.lib.utexas.edu/action/displayAbstract?aid=4743papers3://publication/uuid/ED377DC1-48F0-4823-835A-AD3673F219AF`

Bröcker, M., & Enders, M. (2001, jun). Unusual bulk-rock compositions in eclogite-facies rocks from Syros and Tinos (Cyclades, Greece): implications for U–Pb zircon geochronology. *Chemical Geology*, *175*(3-4), 581–603. Retrieved from `http://linkinghub.elsevier.com/retrieve/pii/S0009254100003697file:///Users/Behr-admin/Dropbox/Papers/Library.papers3/Articles/Br{\%}25C3{\%}25B6cker/2001/Br{\%}25C3{\%}25B6cker{\_}ChemicalGeology{\_}2001.pdfpapers3://publication/doi/10.1016/S0009-2541(00)00369-7`

Bröcker, M., & Keasling, A. (2006, aug). Ionprobe U-Pb zircon ages from the high-pressure/low-temperature mélange of Syros, Greece: age diversity and the importance of pre-Eocene subduction. *Journal of Metamorphic Geology*, *24*(7), 615–631. Retrieved from `http://doi.wiley.com/10.1111/j.1525-1314.2006.00658.xfile:///Users/Behr-admin/Dropbox/Papers/Library.papers3/Articles/Br{\%}25C3{\%}25B6cker/2006/Br{\%}25C3{\%}25B6cker{\_}JournalofMetamorphicGeology{\_}2006.pdfpapers3://publication/doi/10.1111/j.1525-1314.2006.00658.x`

Bröcker, M., Kreuzer, H., Matthews, A., & Okrusch, M. (1993). 40Ar/39Ar and oxygen isotope studies of polymetamorphism from Tinos Island, Cycladic blueschist belt, Greece. *Journal of Metamorphic Geology*, *11*, 223–240.

Brown, E. (1977). The crossite content of ca-amphibole as a guide to pressure of metamorphism. *Journal of Petrology*, *18*(1), 53–72.

Brun, J.-P. P., & Faccenna, C. (2008, jan). Exhumation of high-pressure rocks driven by slab rollback. *Earth and Planetary Science Letters*, *272*, 1–7. Retrieved from `http://linkinghub.elsevier.com/retrieve/pii/S0012821X08001416papers3://publication/uuid/E8FE17E1-C60B-4AC9-8C9F-4435EA549A1D`

Bulle, F., Bröcker, M., Gärtner, C., & Keasling, A. (2010). Geochemistry and geochronology of HP mélanges from Tinos and Andros, Cycladic blueschist belt, Greece. *Lithos*, *117*(1-4), 61–81.

Burov, E., Francois, T., Yamato, P., & Wolf, S. (2014). Mechanisms of continental subduction and exhumation of HP and UHP rocks. *Gondwana Research*, *25*(2), 464–493.

Calvert, A. J., Preston, L. A., & Farahbod, A. M. (2011). Sedimentary underplating at the cascadia mantle-wedge corner revealed by seismic imaging. *Nature Geoscience*, *4*(8), 545–548.

Chemenda, A., Mattauer, M., Malavieille, J., & Bokun, A. (1995, jan). A mechanism for syn-collisional rock exhumation and associated normal faulting: Results from physical modelling. *Earth and Planetary Science Letters*, *132*, 225–232. Retrieved from `http://linkinghub.elsevier.com/retrieve/pii/0012821X9500042Bpapers3://publication/uuid/24846994-FAB6-4147-8883-2A2B9B1D53B5`

Cisneros, M., Barnes, J., Behr, W. M., Kotowski, A. J., Stockli, D., & Soukis, K. (in press). Insights from elastic thermobarometry into exhumation of high-pressure metamorphic rocks from syros, greece. *Solid Earth*.

Cliff, R. A., Bond, C. E., Butler, R. W. H., & Dixon, J. E. (2016, dec). Geochronological challenges posed by continuously developing tectonometamorphic systems; insights from Rb–Sr mica ages from the Cycladic Blueschist Belt, Syros (Greece). *J. Metamorph. Geol.*, doi:10.1111/jmg.12228. Retrieved from `http://doi.wiley.com/10.1111/jmg.12228` doi: 10.1111/jmg.12228

Cliff, R. A., & Meffan-Main, S. (2003, jan). Evidence from Rb-Sr microsampling geochronology for the timing of Alpine deformation in the Sonnblick Dome, SE Tauern Window, Austria. *Geochronology: Linking the Isotopic Record with Petrology and Textures*, 159. Retrieved from `papers3://publication/uuid/08ECF850-E95C-4774-B506-7043EE2BE72A`

Cloos, M. (1982, jan). Flow melanges: Numerical modeling and geologic constraints on their origin in the Franciscan subduction complex, California. *GSA Bulletin*, *93*(4), 330. Retrieved from `http://bulletin.geoscienceworld.org/cgi/content/abstract/93/4/330papers3://publication/uuid/388347B7-1AC8-4B74-B3B6-DC5C0E39C06A`

Cloos, M. (1986). Blueschists in the Franciscan Complex of California: Petrotectonic constraints on uplift mechanisms. In *Blueschists and eclogites* (Vol. 164, pp. 77–93). Geological Society of America Memoir.

Cooperdock, E. H., Raia, N. H., Barnes, J. D., Stockli, D. F., & Schwarzenbach, E. M. (2018). Tectonic origin of serpentinites on Syros, Greece: Geochemical signatures of abyssal origin preserved in a HP/LT subduction complex. *Lithos*, *296*, 352–364.

Dixon, J. E. (1976). Glaucophane schists of Syros, Greece. *Bulletin de la Société géologique de France*, *7*(2), 280.

Dixon, J. E., & Ridley, J. (1987). Syros. In *Chemical transport in metasomatic processes* (Vol. 218, pp. 489–501). Reidel Publishing Company Dordrecht.

Dragovic, B., Baxter, E. F., & Caddick, M. J. (2015). Pulsed dehydration and garnet growth during subduction revealed by zoned garnet geochronology and thermodynamic modeling, Sifnos, Greece. *Earth and Planetary Science Letters*, *413*, 111–122.

Dragovic, B., Samanta, L. M., Baxter, E. F., & Selverstone, J. (2012). Using garnet to constrain the duration and rate of water-releasing metamorphic reactions during subduction: An example from Sifnos, Greece. *Chemical Geology*, *314*, 9–22.

Dürr, S., Altherr, R., Keller, J., Okrusch, M., & Seidel, E. (1978). The median Aegean crystalline belt: stratigraphy, structure, metamorphism, magmatism. *Alps, Apennines, Hellenides*, *38*, 455–476.

Ernst, W., & Liu, J. (1998). Experimental phase-equilibrium study of Al-and Ti-contents of calcic amphibole in MORB—a semiquantitative thermobarometer. *American mineralogist*, *83*(9-10), 952–969.

Evans, B. W. (1990). Phase relations of epidote-blueschists. *Lithos*, *25*(1-3), 3–23. doi: 10.1016/0024-4937(90)90003-J

Fagereng, Å., Savage, H., Morgan, J., Wang, M., Meneghini, F., Barnes, P., ... others (2019). Mixed deformation styles observed on a shallow subduction thrust, hikurangi

margin, new zealand. *Geology*, *47*(9), 872–876.
Flansburg, M. E., Stockli, D. F., Poulaki, E. M., & Soukis, K. (2019). Tectono-magmatic and stratigraphic evolution of the Cycladic Basement, Ios Island, Greece. *Tectonics*.
Forster, M., Koudashev, O., Nie, R., Yeung, S., & Lister, G. (2020). 40ar/39ar thermochronology in the ios basement terrane resolves the tectonic significance of the south cyclades shear zone. *Geological Society, London, Special Publications*, *487*(1), 291–313.
Forster, M., & Lister, G. (2005). Several distinct tectono-metamorphic slices in the Cycladic eclogite–blueschist belt, Greece. *Contributions to Mineralogy and Petrology*, *150*(5), 523–545.
Forster, M., & Lister, G. (2008). Tectonic sequence diagrams and the structural evolution of schists and gneisses in multiply deformed terranes. *Journal of the Geological Society*, *165*(5), 923–939.
Freeman, S., Inger, S., Butler, R., & Cliff, R. A. (1997, jan). Dating deformation using Rb-Sr in white mica: Greenschist facies deformation ages .... *Tectonics*. Retrieved from `http://europa.agu.org/?uri=/journals/tc/96TC02477.xml{\&}view=articlepapers3://publication/uuid/E7B4274F-FDB0-40E7-8266-BBD52B38F230`
Fu, B., Bröcker, M., Ireland, T., Holden, P., & Kinsley, L. P. (2015). Zircon U–Pb, O, and Hf isotopic constraints on Mesozoic magmatism in the Cyclades, Aegean Sea, Greece. *International Journal of Earth Sciences*, *104*(1), 75–87.
Fu, B., Paul, B., Cliff, J., Bröcker, M., & Bulle, F. (2012). O-Hf isotope constraints on the origin of zircon in high-pressure melange blocks and associated matrix rocks from Tinos and Syros, Greece. *European Journal of Mineralogy*, *24*(2), 277–287.
Gautier, P., Brun, J.-P., & Jolivet, L. (1993). Structure and kinematics of upper cenozoic extensional detachment on naxos and paros (cyclades islands, greece). *Tectonics*, *12*(5), 1180–1194.
Gerya, T. V., & Stöckhert, B. (2002, jan). Exhumation rates of high pressure metamorphic rocks in subduction channels: the effect of rheology. *Geophysical Research Letters*, *29*(8), 1261. Retrieved from `papers3://publication/uuid/B673D8A0-155B-43D0-B5CF-7026FE19896B`
Gerya, T. V., Stöckhert, B., & Perchuk, A. L. (2002, jan). Exhumation of high-pressure metamorphic rocks in a subduction channel: A numerical simulation. *Tectonics*, *21*(6), doi:10.1029/2002TC001406. Retrieved from `http://www.agu.org/pubs/crossref/2002/2002TC001406.shtmlpapers3://publication/doi/10.1029/2002TC001406`
Gessner, K., Gallardo, L. A., Markwitz, V., Ring, U., & Thomson, S. N. (2013). What caused the denudation of the menderes massif: Review of crustal evolution, lithosphere structure, and dynamic topography in southwest turkey. *Gondwana research*, *24*(1), 243–274.
Glodny, J., Austrheim, H., Molina, J. F., Rusin, A. I., & Seward, D. (2003). Rb/sr record of fluid-rock interaction in eclogites: The marun-keu complex, polar urals, russia. *Geochimica et Cosmochimica Acta*, *67*(22), 4353–4371.
Glodny, J., Kühn, A., & Austrheim, H. (2008, jan). Diffusion versus recrystallization processes in Rb–Sr geochronology: Isotopic relics in .... *Geochimica et Cosmochimica Acta*. Retrieved from `http://linkinghub.elsevier.com/retrieve/pii/S0016703707006345papers3://publication/uuid/9FE00F83-E636-43B0-9933-35B5FCBFE721`
Glodny, J., Ring, U., Kühn, A., Gleissner, P., & Franz, G. (2005, may). Crystallization and very rapid exhumation of the youngest Alpine eclogites (Tauern Window, Eastern Alps) from Rb/Sr mineral assemblage analysis. *Contributions to Mineralogy and Petrology*, *149*(6), 699–712. Retrieved from `http://www.springerlink.com/index/U5PW505180300421.pdfpapers3://publication/doi/10.1007/s00410-005-0676-5`
Grasemann, B., Schneider, D. A., Stockli, D. F., Iglseder, C., Stöckli, D. F., & Iglseder, C. (2012, jan). Miocene bivergent crustal extension in the Aegean: Evidence from the western Cyclades (Greece). *Lithosphere*, *4*(1), 23–

39. Retrieved from http://lithosphere.gsapubs.org/cgi/doi/10.1130/L164.1papers3://publication/doi/10.1130/L164.1

Halama, R., Glodny, J., Konrad-Schmolke, M., & Sudo, M. (2018). Rb-sr and in situ 40ar/39ar dating of exhumation-related shearing and fluid-induced recrystallization in the sesia zone (western alps, italy). *Geosphere*, *14*(4), 1425–1450.

Hawthorne, F. C., Oberti, R., Harlow, G. E., Maresch, W. V., Martin, R. F., Schumacher, J. C., & Welch, M. D. (2012). Nomenclature of the amphibole supergroup. *American Mineralogist*, *97*(11-12), 2031–2048.

Hecht, J. (1985). Geological map of Greece 1: 50 000, Syros island. *Institute of Geology and Mineral Exploration, Athens*.

Huet, B., Labrousse, L., & Jolivet, L. (2009). Thrust or detachment? exhumation processes in the aegean: Insight from a field study on ios (Cyclades, Greece). *Tectonics*, *28*(3). doi: 10.1029/2008TC002397

Inger, S., & Cliff, R. (1994). Timing of metamorphism in the tauern window, eastern alps: Rb-sr ages and fabric formation. *Journal of metamorphic Geology*, *12*(5), 695–707.

Jacobshagen, V. (1986). Geologie von Griechenland: Gebrüder Borntraeger. *Berlin-Stuttgart, 363pp*.

Jolivet, L., & Brun, J. P. (2010). Cenozoic geodynamic evolution of the Aegean. *International Journal of Earth Sciences*, *99*(1), 109–138. doi: 10.1007/s00531-008-0366-4

Jolivet, L., Faccenna, C., Goffé, B., Burov, E. B., & Agard, P. (2003, jan). Subduction tectonics and exhumation of high-pressure metamorphic rocks in the Mediterranean orogens. *American Journal of Science*, *303*(5), 353–409. Retrieved from http://ajsonline.org/cgi/content/abstract/303/5/353papers3://publication/uuid/313C27F4-1B1D-49D2-A7A3-953D704E5793

Jolivet, L., Faccenna, C., Huet, B., Labrousse, L., Le Pourhiet, L., Lacombe, O., . . . Driussi, O. (2013). Aegean tectonics: Strain localisation, slab tearing and trench retreat. *Tectonophysics*, *597-598*, 1–33. doi: 10.1016/j.tecto.2012.06.011

Jolivet, L., Trotet, F., Monie, P., Vidal, O., Goffé, B., Labrousse, L., . . . Ghorbal, B. (2010, jan). Along-strike variations of PT conditions in accretionary wedges and syn-orogenic extension, the HP-LT Phyllite-Quartzite Nappe in Crete and the Peloponnese. *Tectonophysics*, *480*(1-4), 133–148. Retrieved from papers3://publication/uuid/05D78E1D-3C49-4CA6-98C3-97A752D40E1F

Keay, S. (1998). *The geological evolution of the Cyclades, Greece: constraints from SHRIMP U-Pb geochronology* (Unpublished doctoral dissertation).

Keay, S., & Lister, G. (2002). African provenance for the metasediments and metaigneous rocks of the Cyclades, Aegean Sea, Greece. *Geology*, *30*(3), 235–238.

Keiter, M., Ballhaus, C., & Tomaschek, F. (2011). A new geological map of the Island of Syros (Aegean Sea, Greece): Implications for lithostratigraphy and structural history of the Cycladic Blueschist Unit. *Geol. Soc. Am. Spec. Pap.*, *481*, 1–43.

Keiter, M., Piepjohn, K., Ballhaus, C., Lagos, M., & Bode, M. (2004, aug). Structural development of high-pressure metamorphic rocks on Syros island (Cyclades, Greece). *Journal of Structural Geology*, *26*(8), 1433–1445. Retrieved from http://linkinghub.elsevier.com/retrieve/pii/S0191814103002062papers3://publication/doi/10.1016/j.jsg.2003.11.027http://www.sciencedirect.com/science/article/pii/S0191814103002062papers3://publication/uuid/9F769F57-8390-43F0-8D62-C74BBB0F90B4

Kendall, J. (2016). *Sm/nd garnet geochronology and pressure-temperature paths of eclogites from syros, greece: Implications for subduction zone processes and water loss from the subducting slab* (Unpublished doctoral dissertation). Boston College.

Kimura, G., Yamaguchi, A., Hojo, M., Kitamura, Y., Kameda, J., Ujiie, K., . . . Hina, S. (2012). Tectonic mélange as fault rock of subduction plate boundary. *Tectonophysics*, *568*, 25–38.

Kimura, H., Takeda, T., Obara, K., & Kasahara, K. (2010). Seismic evidence for active underplating below the megathrust earthquake zone in japan. *Science*, *329*(5988), 210–212.

Kirchner, K. L., Behr, W. M., Loewy, S., & Stockli, D. F. (2016). Early Miocene subduction in the western Mediterranean, constraints from Rb-Sr multi-mineral isochron geochronology. *Geochem. Geophys. Geosyst.*, *17*(5), doi:10.1002/2015GC006208. doi: 10.1002/2015GC006208

Kleine, B. I., Skelton, A. D., Huet, B., & Pitcairn egu045., I. K. . (2014). Preservation of Blueschist-facies Minerals along a Shear Zone by Coupled Metasomatism and Fast-flowing CO2-bearing Fluids. *Journal of Petrology*, *55*, 1905–1939.

Kotowski, A. J., & Behr, W. M. (2019). Length scales and types of heterogeneities along the deep subduction interface: Insights from exhumed rocks on Syros Island, Greece. *Geosphere*.

Kullerud, L. (1991). On the calculation of isochrons. *Chemical Geology: Isotope Geoscience section*, *87*(2), 115–124.

Lagos, M., Scherer, E. E., Tomaschek, F., Münker, C., Keiter, M., Berndt, J., & Ballhaus, C. (2007, jan). High precision Lu–Hf geochronology of Eocene eclogite-facies rocks from Syros, Cyclades, Greece. *Chemical Geology*, *243*(1), 16–35. Retrieved from `http://www.sciencedirect.com/science/article/pii/S0009254107001751papers3://publication/uuid/77497147-A4FC-4D87-B574-681BE0904700`

Laird, J., & Albee, A. L. (1981). Pressure, temperature, and time indicators in mafic schist; their application to reconstructing the polymetamorphic history of Vermont. *American Journal of Science*, *281*(2), 127–175.

Lanari, P., & Duesterhoeft, E. (2018). Modeling metamorphic rocks using equilibrium thermodynamics and internally consistent databases: past achievements, problems and perspectives. *Journal of petrology*, *60*(1), 19–56.

Lanari, P., & Engi, M. (2017). Local bulk composition effects on metamorphic mineral assemblages. *Reviews in Mineralogy and Geochemistry*, *83*(1), 55–102.

Lanari, P., Giuntoli, F., Loury, C., Burn, M., & Engi, M. (2017). An inverse modeling approach to obtain P–T conditions of metamorphic stages involving garnet growth and resorption. *European Journal of Mineralogy*, *29*(2), 181–199.

Laurent, V., Huet, B., Labrousse, L., Jolivet, L., Monie, P., & Augier, R. (2017). Extraneous argon in high-pressure metamorphic rocks: Distribution, origin and transport in the Cycladic Blueschist Unit (Greece). *Lithos*, *272*, 315–335.

Laurent, V., Jolivet, L., Roche, V., Augier, R., Scaillet, S., & Cardello, G. L. (2016). Strain localization in a fossilized subduction channel: Insights from the Cycladic Blueschist Unit (Syros, Greece). *Tectonophysics*, *672*(150-169). doi: 10.1016/j.tecto.2016.01.036

Laurent, V., Lanari, P., Naïr, I., Augier, R., Lahfid, A., & Jolivet, L. (2018). Exhumation of eclogite and blueschist (Cyclades, Greece): Pressure–Temperature evolution determined by thermobarometry and garnet equilibrium modelling. *Journal of Metamorphic Geology*.

Leake, B. E., Wooley, A. R., Arps, C. E., Birch, W. D., Gilbert, M. C., Grice, J. D., . . . others (1997). Nomenclature of amphiboles; report of the subcommittee on amphiboles of the international mineralogical association commission on new minerals and mineral names. *European Journal of Mineralogy*, *9*(3), 623–651.

Liou, J. (1971). P—T stabilities of laumontite, wairakite, lawsonite, and related minerals in the system CaAl2Si2O8-SiO2-H2O. *Journal of Petrology*, *12*(2), 379–411.

Lister, G., Banga, G., & Feenstra, A. (1984). Metamorphic core complexes of Cordilleran type in the Cyclades, Aegean Sea, Greece. *Geology*, *12*, 221–225.

Lister, G., & Forster, M. (2016). White mica 40Ar/39Ar age spectra and the timing of multiple episodes of high-P metamorphic mineral growth in the Cycladic eclogite–blueschist belt, Syros, Aegean Sea, Greece. *Journal of Metamorphic Geology*, *34*(5), 401–421.

Liu, F., Gerdes, A., Liou, J., Xue, H., & Liang, F. (2006). Shrimp u-pb zircon dating from sulu-dabie dolomitic marble, eastern china: constraints on prograde, ultrahigh-pressure and retrograde metamorphic ages. *Journal of metamorphic Geology*, *24*(7), 569–589.

Löwen, K., Bröcker, M., & Berndt, J. (2015). Depositional ages of clastic metasediments from Samos and Syros, Greece: results of a detrital zircon study. *International Journal of Earth Sciences*, *104*(1), 205–220.

Ludwig, L., Akciz, S., Noriega, G. R., & Zielke, O. (2010, jan). Climate-Modulated Channel Incision and Rupture History of the San .... *Science*. Retrieved from `http://www.public.asu.edu/{~}ozielke/research/data/GrantLudwigEtAl{\_}Science2010.pdfpapers3://publication/uuid/0CE1AAD1-6E4E-4B5C-B6A5-3FE213DAFB23`

Maluski, H., Bonneau, M., & Kienast, J. R. (1987). Dating the metamorphic events in the Cycladic area; 39Ar/40 Ar data from metamorphic rocks of the Island of Syros (Greece). *Bull. Société Géologique Fr.*, *3*, 833–842.

Maruyama, S., Suzuki, K., & Liou, J. (1983). Greenschist–amphibolite transition equilibria at low pressures. *Journal of Petrology*, *24*(4), 583–604.

Massonne, H., & Schreyer, W. (1987). Phengite geobarometry based on the limiting assemblage with K-feldspar, phlogopite, and quartz. *Contributions to Mineralogy and Petrology*, *96*(2), 212–224.

Moody, J. B., Meyer, D., & Jenkins, J. E. (1983). Experimental characterization of the greenschist/amphibolite boundary in mafic systems. *American Journal of Science*, *283*(1), 48–92.

Müller, W., Mancktelow, N. S., & Meier, M. (2000, jan). Rb–Sr microchrons of synkinematic mica in mylonites: an example from the DAV fault of the Eastern Alps. *Earth and Planetary Science Letters*, *180*(3-4), 385–397. Retrieved from `file:///Users/Behr-admin/Dropbox/Papers/Library.papers3/Articles/M{\%}25C3{\%}25BCller/2000/M{\%}25C3{\%}25BCller{\_}EarthandPlanetaryScienceLetters{\_}2000.pdfpapers3://publication/uuid/363451F5-8505-4CFF-ADE2-6E0208DB3E6A`

Okrusch, M., & Bröcker, M. (1990, jan). Eclogites associated with high-grade blueschists in the Cyclades archipelago, Greece; a review. *European Journal of Mineralogy*, *2*(4), 451–478. Retrieved from `http://eurjmin.geoscienceworld.org/content/2/4/451.shortpapers3://publication/uuid/50C6E894-B8CD-4559-9D35-4FFCBA81AA18`

Okrusch, M., Seidel, E., & Davis, E. N. (1978). The assemblage jadeite-quartz in the glaucophane rocks of Sifnos (Cyclades Archipelago, Greece). *N Jb Mineral Abh*, *132*, 284–308.

Otsuki, M., & Banno, S. (1990). Prograde and retrograde metamorphism of hematitebearing basic schists in the sanbagawa belt in central shikoku. *Journal of Metamorphic Geology*, *8*(4), 425–439.

Papanikolaou, D. (1987). Tectonic evolution of the Cycladic blueschist belt (Aegean Sea, Greece). In *Chemical transport in metasomatic processes* (Vol. 218, pp. 429–450).

Papanikolaou, D. (2013, jun). Tectonostratigraphic models of the Alpine terranes and subduction history of the Hellenides. *Tectonophysics*, *595-596*, 1–24. Retrieved from `http://linkinghub.elsevier.com/retrieve/pii/S0040195112004854papers3://publication/doi/10.1016/j.tecto.2012.08.008`

Park, J.-O., Tsuru, T., Takahashi, N., Hori, T., Kodaira, S., Nakanishi, A., ... Kaneda, Y. (2002). A deep strong reflector in the nankai accretionary wedge from multichannel seismic data: Implications for underplating and interseismic shear stress release. *Journal of Geophysical Research: Solid Earth*, *107*(B4), ESE–3.

Pe-Piper, G., Piper, D. J., & Matarangas, D. (2002). Regional implications of geochemistry and style of emplacement of Miocene I-type diorite and granite, Delos, Cyclades, Greece. *Lithos*, *60*(1-2), 47–66.

Philippon, M., Brun, J. P., & Gueydan, F. (2011, jan). Tectonics of the Syros blueschists (Cyclades, Greece): From subduction to Aegean extension. *Tectonics*, *30*, TC4001, doi:10.1029/2010TC002810.

Platt, J. P. (1993, jan). Exhumation of high-pressure rocks: a review of concepts and processes. *Terra Nova*, *5*, 119–133. Retrieved from `http://acad.coloradocollege.edu/dept/gy/ises/docs/Platt{\_}1993{\_}Exhumation.pdfpapers3://publication/uuid/5EBBB563-EB8E-4E5A-8BA8-A49488B06448`

Platt, J. P., Soto, J. I., Whitehouse, M. J., Hurford, A. J., & Kelley, S. P. (1998, jan).

Thermal evolution, rate of exhumation, and tectonic significance of .... *Tectonics*. Retrieved from http://earth.usc.edu/{~}jplatt/pdfs/PlattetalTect1998.pdfpapers3://publication/uuid/9D98D93B-8C39-4333-9426-DDE259D4F338

Platt, J. P., Xia, H., & Schmidt, W. L. (2018). Rheology and stress in subduction zones around the aseismic/seismic transition. *Progress in Earth and Planetary Science*, *5*, 1–12.

Poulaki, E. M., Stockli, D. F., Flansburg, M. E., & Soukis, K. (2019). Zircon u-pb chronostratigraphy and provenance of the cycladic blueschist unit and the nature of the contact with the cycladic basement on sikinos and ios islands, greece. *Tectonics*.

Powell, R., Hergt, J., & Woodhead, J. (2002). Improving isochron calculations with robust statistics and the bootstrap. *Chemical Geology*, *185*(3-4), 191–204.

Putlitz, B., Cosca, M. A., & Schumacher, J. C. (2005, jan). Prograde mica 40Ar/39Ar growth ages recorded in high pressure rocks (Syros, Cyclades, Greece). *Chemical Geology*, *214*(1-2), 79–98. Retrieved from http://linkinghub.elsevier.com/retrieve/pii/S0009254104003547

Raase, P. (1974). Al and Ti contents of hornblende, indicators of pressure and temperature of regional metamorphism. *Contributions to mineralogy and petrology*, *45*(3), 231–236.

Rabillard, A., Jolivet, L., Arbaret, L., Bessière, E., Laurent, V., Menant, A., ... Beaudoin, A. (2018). Synextensional granitoids and detachment systems within cycladic metamorphic core complexes (aegean sea, greece): Toward a regional tectonomagmatic model. *Tectonics*, *37*(8), 2328–2362.

Raimbourg, H., Jolivet, L., & Leroy, Y. (2007). Consequences of progressive eclogitization on crustal exhumation, a mechanical study. *Geophysical Journal International*, *168*(1), 379–401.

Ridley, J. R. (1982). Arcuate lineation trends in a deep level, ductile thrust belt, syros, Greece. *Tectonophysics*, *88*(3-4), 347–360. doi: 10.1016/0040-1951(82)90246-3

Ridley, J. R. (1984, jan). The significance of deformation associated with blueschist facies metamorphism on the Aegean island of Syros. *Geological Society, London, Special Publications*, *17*(1), 545–550.

Ring, U., Glodny, J., Will, T., & Thomson, S. (2007). An Oligocene extrusion wedge of blueschist-facies nappes on Evia, Aegean Sea, Greece: implications for the early exhumation of high-pressure rocks. *Journal of the Geological Society*, *164*, 637–652.

Ring, U., Glodny, J., Will, T., & Thomson, S. (2010, jan). The Hellenic subduction system: high-pressure metamorphism, exhumation, normal faulting, and large-scale extension. *Annual Review of Earth and Planetary Sciences*, *38*, 45–76. Retrieved from http://www.annualreviews.org/doi/abs/10.1146/annurev.earth.050708.170910papers3://publication/doi/10.1146/annurev.earth.050708.170910

Ring, U., Glodny, J., Will, T. M., & Thomson, S. (2011). Normal faulting on sifnos and the south cycladic detachment system, aegean sea, greece. *Journal of the Geological Society*, *168*(3), 751–768.

Ring, U., & Layer, P. W. (2003). High-pressure metamorphism in the Aegean, eastern Mediterranean: Underplating and exhumation from the Late Cretaceous until the Miocene to Recent above the retreating Hellenic subduction zone. *Tectonics*, *22*(3).

Ring, U., Layer, P. W., & Reischmann, T. (2001). Miocene high-pressure metamorphism in the Cyclades and Crete, Aegean Sea, Greece: Evidence for large-magnitude displacement on the Cretan detachment. *Geology*, *29*(5), 395–398. doi: 10.1130/0091-7613(2001)029⟨0395:MHPMIT⟩2.0.CO;2

Ring, U., Pantazides, H., Glodny, J., & Skelton, A. (2020). Forced return flow deep in the subduction channel, syros, greece. *Tectonics*, *39*(1), e2019TC005768.

Ring, U., & Reischmann, T. (2002). The weak and superfast Cretan detachment, Greece: exhumation at subduction rates in extruding wedges. *Journal of the Geological Society*, *159*, 225–228. doi: 10.1144/0016-764901-150

Ring, U., Thomson, S. N., & Bröcker, M. (2003). Fast extension but little exhumation: the Vari detachment in the Cyclades, Greece. *Geological Magazine*, *140*(3), 245–252.

Ring, U., Will, T., Glodny, J., Kumerics, C., Gessner, K., Thomson, S., & Drüppel, K.

(2007, jan). Early exhumation of high-pressure rocks in extrusion wedges: Cycladic blueschist unit in the eastern Aegean, Greece, and Turkey. *Tectonics*, *26*, TC2001. Retrieved from http://www.agu.org/pubs/crossref/2007.../2005TC001872.shtmlpapers3://publication/uuid/11FA1518-AD95-4182-9BE4-2B6413C8D45F

Robertson, A. H. F. (2007). Overview of tectonic settings related to the rifting and opening of Mesozoic ocean basins in the Eastern Tethys: Oman, Himalayas and Eastern Mediterranean regions. *Geological Society, London, Special Publications*, *282*(1), 325–388.

Robinson, P. (1982). Phase relations of metamorphic amphiboles: Natural occurences and theory. *Rev. Mineral.*, *9*, 1–227.

Roche, V., Laurent, V., Cardello, G. L., Jolivet, L., & Scaillet, S. (2016). Anatomy of the cycladic blueschist unit on sifnos island (cyclades, greece). *Journal of Geodynamics*, *97*, 62–87.

Rogowitz, A., Grasemann, B., Huet, B., & Habler, G. (2014). Strain rate dependent calcite microfabric evolution–an experiment carried out by nature. *Journal of Structural Geology*, *69*, 1–17.

Romer, R. L., & Rotzler, J. (2011). The role of element distribution for the isotopic dating of metamorphic minerals. *European Journal of Mineralogy*, *23*(1), 17–33.

Rondenay, S., Abers, G. A., & van Keken, P. E. (2008, jan). Seismic imaging of subduction zone metamorphism. *Geology*, *36*(4), 274–275. Retrieved from http://geology.gsapubs.org/cgi/doi/10.1130/G24112A.1papers3://publication/doi/10.1130/G24112A.1

Rosenbaum, G., Avigad, D., & Sánchez-Gómez, M. (2002, jan). Coaxial flattening at deep levels of orogenic belts: evidence from blueschists and eclogites on Syros and Sifnos (Cyclades, Greece). *Journal of Structural Geology*, *24*, 1451–1462.

Ruffet, G., Féraud, G., Ballèvre, M., & Kiénast, J. R. (1995, jan). Plateau ages and excess argon in phengites: an 40Ar 39Ar laser probe study of Alpine micas (Sesia Zone, Western Alps, northern Italy). *Chemical Geology*, *121*(1-4), 327–343. Retrieved from papers3://publication/uuid/6814706D-6FE8-4CF0-B86A-7D88DAD96861

Schliestedt, M. (1986). Eclogite-blueschist relationships as evidenced by mineral equilibria in the high-pressure metabasic rocks of sifnos (Cycladic Islands), Greece. *Journal of Petrology*, *27*(6), 1437–1459. doi: 10.1093/petrology/27.6.1437

Schmädicke, E., & Will, T. M. (2003). Pressure-Temperature evolution of blueschist facies rocks from Sifnos, Greece, and implications for the exhumation of high-pressure rocks in the Central Aegean. *Journal of Metamorphic Geology*, *21*(8), 799–811. doi: 10.1046/j.1525-1314.2003.00482.x

Schmidt, M. W. (1992). Amphibole composition in tonalite as a function of pressure: an experimental calibration of the Al-in-hornblende barometer. *Contributions to mineralogy and petrology*, *110*(2-3), 304–310.

Schneider, D. A., Grasemann, B., Lion, A., Soukis, K., & Draganits, E. (2018). Geodynamic significance of the Santorini Detachment System (Cyclades, Greece). *Terra Nova*.

Schumacher, J. C., J.B., B., Cheney, J. T., Tonnsen, R. R., Brady, J. B., Cheney, J. T., & Tonnsen, R. R. (2008, aug). Glaucophane-bearing Marbles on Syros, Greece. *J. Petrology*, *49*(9), 1667–1686. Retrieved from http://www.petrology.oxfordjournals.org/cgi/doi/10.1093/petrology/egn042papers3://publication/doi/10.1093/petrology/egn042

Seck, H. A., Koetz, J., Okrusch, M., Seidel, E., & Stosch, H.-G. (1996). Geochemistry of a meta-ophiolite suite: an association of metagabbros, eclogites and glaucophanites on the island of Syros, Greece. *European Journal of Mineralogy*, 607–624.

Seidel, E., Kreuzer, H., & Harre, W. (1982). A late oligocene/early miocene high pressure belt in the external hellenides. *Geologisches Jahrbuch. Reihe E, Geophysik*(23), 165–206.

Seman, S. (2016). *The tectonostratigraphy of the Cycladic Blueschist Unit and new garnet geo/thermochronology techniques* (Unpublished doctoral dissertation).

Seman, S., Stockli, D., & Soukis, K. (2017). The provenance and internal structure of the

Cycladic Blueschist Unit revealed by detrital zircon geochronology, Western Cyclades, Greece. *Tectonics*, *36*(7), 1407–1429.

Sherlock, S. C., & Arnaud, N. O. (1999). Flat plateau and impossible isochrons: Apparent 40ar-39ar geochronology in a high-pressure terrain. *Geochimica et Cosmochimica Acta*, *63*(18), 2835–2838.

Skelton, A., Peillod, A., Glodny, J., Klonowska, I., Månbro, C., Lodin, K., & Ring, U. (2019). Preservation of high-P rocks coupled to rock composition and the absence of metamorphic fluids. *Journal of Metamorphic Geology*.

Skora, S., Baumgartner, L. P., Mahlen, N. J., Johnson, C. M., Pilet, S., & Hellebrand, E. (2006). Diffusion-limited ree uptake by eclogite garnets and its consequences for lu–hf and sm–nd geochronology. *Contributions to Mineralogy and Petrology*, *152*(6), 703–720.

Soukis, K., & Stockli, D. F. (2013, jan). Structural and thermochronometric evidence for multi-stage exhumation of southern Syros, Cycladic islands, Greece. *Tectonophysics*, *595-596*, 148–164. Retrieved from `http://www.sciencedirect.com/science/article/pii/S0040195112002806papers3://publication/uuid/E4EA6C10-9045-4A74-AF9D-0D016D22F6A8`

Sousa, J., Kohn, M. J., Schmitz, M. D., Northrup, C. J., & Spear, F. (2013). Strontium isotope zoning in garnet: implications for metamorphic matrix equilibration, geochronology and phase equilibrium modelling. *Journal of Metamorphic Geology*, *31*(4), 437–452.

Thompson, R. (1974). Some high-pressure pyroxenes. *Mineralogical Magazine*, *39*(307), 768–787.

Thomson, S. N., Stöckhert, B., & Brix, M. R. (1999). Miocene high-pressure metamorphic rocks of crete, greece: rapid exhumation by buoyant escape. *Geological Society, London, Special Publications*, *154*(1), 87–107.

Tomaschek, F., Keiter, M., Kennedy, A. K., & Ballhaus, C. (2008). Pre-Alpine basement within the Northern Cycladic Blueschist Unit on Syros Island, Greece [Präalpines Grundgebirge in der Nördlichen Kykladischen Blauschiefereinheit auf der Insel Syros, Griechenland.]. *Zeitschrift der deutschen Gesellschaft für Geowissenschaften*, *159*(3), 521–531.

Tomaschek, F., Kennedy, A. K., Villa, I. M., Lagos, M., & Ballhaus, C. (2003). Zircons from Syros, Cyclades, Greece—recrystallization and mobilization of zircon during high-pressure metamorphism. *Journal of Petrology*, *44*(11), 1977–2002.

Trotet, F., Jolivet, L., & Vidal, O. (2001). Tectono-metamorphic evolution of Syros and Sifnos islands (Cyclades, Greese). *Tectonophysics*, *338*(2), 179–206. doi: 10.1016/S0040-1951(01)00138-X

Trotet, F., Vidal, O., & Jolivet, L. (2001). Exhumation of Syros and Sifnos metamorphic rocks (Cyclades, Greece). New constraints on the PT paths. *European Journal of Mineralogy*, *13*(5), 901–902.

Ukar, E., Cloos, M., & Vasconcelos, P. (2012). First 40ar-39ar ages from low-t mafic blueschist blocks in a franciscan mélange near san simeon: Implications for initiation of subduction. *The Journal of Geology*, *120*(5), 543–556.

Uunk, B., Brouwer, F., ter Voorde, M., & Wijbrans, J. (2018). Understanding phengite argon closure using single grain fusion age distributions in the Cycladic Blueschist Unit on Syros, Greece. *Earth and Planetary Science Letters*, *484*, 192–203.

Vanderhaeghe, O., & Whitney, D. (2004). Structural development of the naxos migmatite dome. *SPECIAL PAPERS-GEOLOGICAL SOCIETY OF AMERICA*, 211–228.

van der Maar, P. A., & Jansen, J. B. H. (1983). The geology of the polymetamorphic complex of Ios, Cyclades, Greece and its significance for the Cycladic Massif. *Geologische Rundschau*, *72*(1), 283–299.

Van Hinsbergen, D. J., Torsvik, T. H., Schmid, S. M., Maţenco, L. C., Maffione, M., Vissers, R. L., … Spakman, W. (2020). Orogenic architecture of the mediterranean region and kinematic reconstruction of its tectonic evolution since the triassic. *Gondwana Research*, *81*, 79–229.

Vermeesch, P. (2018). Isoplotr: A free and open toolbox for geochronology. *Geoscience Frontiers*, *9*(5), 1479–1493.

Villa, I. M., De Bièvre, P., Holden, N., & Renne, P. (2015). Iupac-iugs recommendation on the half life of 87rb. *Geochimica et Cosmochimica Acta*, *164*, 382–385.

Wakabayashi, J. (1990). Counterclockwise PTt paths from amphibolites, Franciscan Complex, California: Relics from the early stages of subduction zone metamorphism. *The Journal of Geology*, *98*(5), 657–680.

Warren, C. J., Beaumont, C., & Jamieson, R. A. (2008, apr). Formation and exhumation of ultra-high-pressure rocks during continental collision: Role of detachment in the subduction channel. *Geochem. Geophys. Geosyst*, *9*(4). Retrieved from `http://doi.wiley.com/10.1029/2007GC001839papers3://publication/doi/10.1029/2007GC001839`

Wendt, I., & Carl, C. (1991). The statistical distribution of the mean squared weighted deviation. *Chemical Geology: Isotope Geoscience Section*, *86*(4), 275–285.

Wijbrans, J., & McDougall, I. (1988). Metamorphic evolution of the attic cycladic metamorphic belt on naxos (cyclades, greece) utilizing 40ar/39ar age spectrum measurements. *Journal of Metamorphic Geology*, *6*(5), 571–594.

Wijbrans, J. R., Schliestedt, M., & York, D. (1990). Single grain argon laser probe dating of phengites from the blueschist to greenschist transition on Sifnos (Cyclades, Greece). *Contributions to Mineralogy and Petrology*, *104*, 582–593.

Xia, H., & Platt, J. P. (2017). Structural and rheological evolution of the Laramide subduction channel in southern California. *Solid Earth*, *8*(2).

Yakymchuk, C., Clark, C., & White, R. W. (2017). Phase relations, reaction sequences and petrochronology. *Reviews in Mineralogy and Geochemistry*, *83*(1), 13–53.

Appendix A Geochronology

A1 Rb-Sr Methods and Sample Descriptions

Cm-sized pieces of rock were cut out from hand samples to isolate specific fabrics corresponding to progressive stages of deformation-metamorphism as outlined in Section 4. Samples were crushed with a small hammer between sheets of paper, and ground gently with a mini metal rock crusher to separate mineral aggregates. Samples were sieved and separated by grain size. Grain size fractions 125-250 μm and 250-500μm were frantzed to separate minerals based on magnetic susceptibility. The first pass was done with strongest magnetic setting (~1.8 Amperes) to remove all non-magnetics (e.g. quartz). Subsequent passes were done starting at the lowest setting where minerals started to magnetically separate (typically ~0.2-0.4 A); separates were repeatedly passed through the Frantz at increments of ~0.1-0.2 A. Magnetic fractions were then cleaned by hand, by either negative or positive picking of phases of interest, including garnet, glaucophane, epidote, and white micas (and apatite and chlorite for retrograde fabrics). White mica separates were cleaned of inclusions by gently smearing them in a mortar and pestle and washing them through a sieve with ethanol.

SY1616 was collected from float blocks at Kini Beach immediately beneath in-place blueschist-to-eclogite facies cliff faces. The sample is representative of D_S in blueschist-eclogite lithologies. The foliation is defined by glaucophane, epidote, phengite, paragonite, and rutile, with porphyroblasts of garnet and omphacite. Glaucophane, epidote, omphacite, and phengite define the lineation. A similar rock type is shown in Figure 7A. The prograde fabric was targeted for geochronology.

KCS1617 was collected from Azolimnos (approximate location: 37° 24'43.86"N, 24° 57'55.42"E). The sample records an older D_S cleavage cross-cut by the D_{T1} upright crenulation. The mineral assemblage includes glaucophane, epidote, quartz, phengite, paragonite, garnet, rutile, titanite, and oxides. The D_{T1} fabric was cut out of the sample using a diamond-tipped rock saw and targeted for geochronology.

KCS1621 was collected from the southern side of Delfini Beach (approximate location: 37°27'14.61"N, 24°53'51.23"E). The sample is representative of D_{T2}. The foliation is defined by quartz, phengite, paragonite and the lineation is defined by porphyroblasts of epidote and actinolite. This sample is interbedded with quartz-rich schists that have a blue amphibole lineation decimeters to meters above and below. The greenschist-facies fabric was targeted for geochronology.

SY1402 was collected from Lotos (approximate location: 37°26'36.64"N, 24°53'48.87"E). The sample is representative of D_{T2}, during penetrative greenschist-faces deformation and transposition of older fabrics, and some rocks surpass the ductile-to-brittle transition. The sample collected for geochronology is a reaction rind at the margin of a brittlely boudinaged epidote-rich lens, and includes actinolite, chlorite, epidote, phengite, paragonite, and apatite. SY1644 was collected from the southern side of Delfini, very close to KCS1621. The sample is representative of D_{T2}, as rocks locally surpass the ductile-to-brittle transition. Minerals collected for geochronology were precipitated within the boudin neck of a brittlely boudinaged epidote-rich lens including actinolite, epidote, white mica, and calcite.

A2 Compilation of previous geochronology on Syros

Figure A1 and Table A2 show a compilation of published metamorphic geochronology for the island of Syros (through 2019), comprising 185 individual published ages from 16 studies and 5 chronometers. Applying filters discussed in Section 6.2 to the dataset shown in Figure 3B reduces the compilation from 89 (excludes igneous zircon) to 44 data points, which are plotted in Figure 11. The refined dataset comprises 65 individual ages (some presented as weighted means) that include 44 single-grain analyses and 21 isochrons. The single-grain analyses include 6 ^{40}Ar/^{39}Ar white mica (Rogowitz et al., 2015; Laurent et

Sample ID and Summary	Phases defining the isochron	Initial Sr	Age	Uncertainty	MSWD	n
SY1616: Kini omphacite-epidote blueschist	paragonite-phengite	0.7032083	53.53	0.17	1	2
	glaucophane-phengite	0.7032228	53.29	0.17	1	2
	omphacite-phengite	0.7032158	53.41	0.17	1	2
	garnet-phengite	0.703212	53.47	0.21	1	2
	epidote-garnet-phengite	0.7032199	53.34	0.15	0.91	3
	epidote-omphacite-phengite	0.7032198	53.34	0.14	0.64	3
	epidote-garnet-omphacite-phengite	0.7032183	53.36	0.14	0.56	4
	glaucophane-omphacite-garnet-phengite	0.7032179	54.37	0.14	0.46	4
	omphacite-paragonite-garnet-phengite	0.7032121	53.47	0.14	0.28	4
	paragonite(x4)-phengite	0.7031964	53.73	0.13	1.4	5
	** ep-glauc-omph-parag-grt ** NO PHENG	0.703221	59.07	8.57	1.7	5
KCS1617: Azolimnos glaucophane-mica blueschist	epidote-phengite	0.7066671	45.14	0.05	1	2
	glaucophane-phengite	0.7065696	45.61	0.1	1	2
	paragonite-phengite	0.7065964	45.48	0.05	1	2
	paragonite-phengite-phengite	0.7065992	45.47	0.05	0.41	3
	glaucophane-phengite-phengite	0.7065829	45.56	0.61	8.8	3
	epidote-phengite-phengite	0.706643	45.23	0.05	31	3
	** glaucophane-paragonite(x4) ** NO PHENG	0.7066026	43.44	0.76	10	5
	paragonite(x4)-phengite	0.7065951	45.48	0.13	9.4	5
	8 point isochron (all data, except garnet)	0.7066036	45.43	0.04	23	8
KCS1621: Delfini actinolite-mica greenschist	** paragonite-chlorite ** NO PHENG	0.7066492	35.64	0.39	1	2
	paragonite-chlorite-phengite	0.7066201	37.04	0.015	13	3
	** epidote-chlorite-paragonite ** NO PHENG	0.7066492	35.64	0.39	7.90E-25	3
	epidote-phengite-phengite	0.7067163	36.9	0.03	6.30E-24	3
	epidote-chlorite-phengite(x2)	0.7066195	37.06	0.02	21	4
	epidote-paragonite-phengite(x2)	0.7066498	37.02	0.02	9.8	4
	** epidote-chlorite-paragonite(x3) ** NO PHENG	0.7066471	36.19	0.29	7.9	5
	paragonite(x3)-phengite(x2)	0.7066348	37.05	0.014	16	5
	chlorite-paragonite(x3)-phengite(x2)	0.7066266	37.06	0.013	16	6
	epidote-chlorite-paragonite(x3)-phengite(x2)	0.7066266	37.06	0.013	13	7
	8 point isochron (all data)	0.7065941	36.91	0.013	440	8
SY1644: Delfini mineralization in epidosite boudin neck	epidote-white mica	0.7066098	36.16	0.03	1	2
	actinolite-white mica	0.7067006	35.94	0.03	1	2
SY1402: Lotos reaction rim around epidosite pod	apatite-phengite1	0.704965	36.49	0.01	1	2
	apatite-phengite2	0.704965	35.94	0.01	1	2
	apatite-phengite3	0.704965	33.18	0.011	1	2
	apatite-phengite4	0.704966	29.43	0.014	1	2

Table A1: Evaluating the robustness of Rb-Sr ages. Various isochrons are calculated for each sample discussed in-text, for different combinations of (assumed) co-genetic phases. MSWD values are a reflection of anaytical uncertainty and the goodness of fit of all data points on a given isochron; therefore, any two-point isochron by definition has an MSWD of 1.

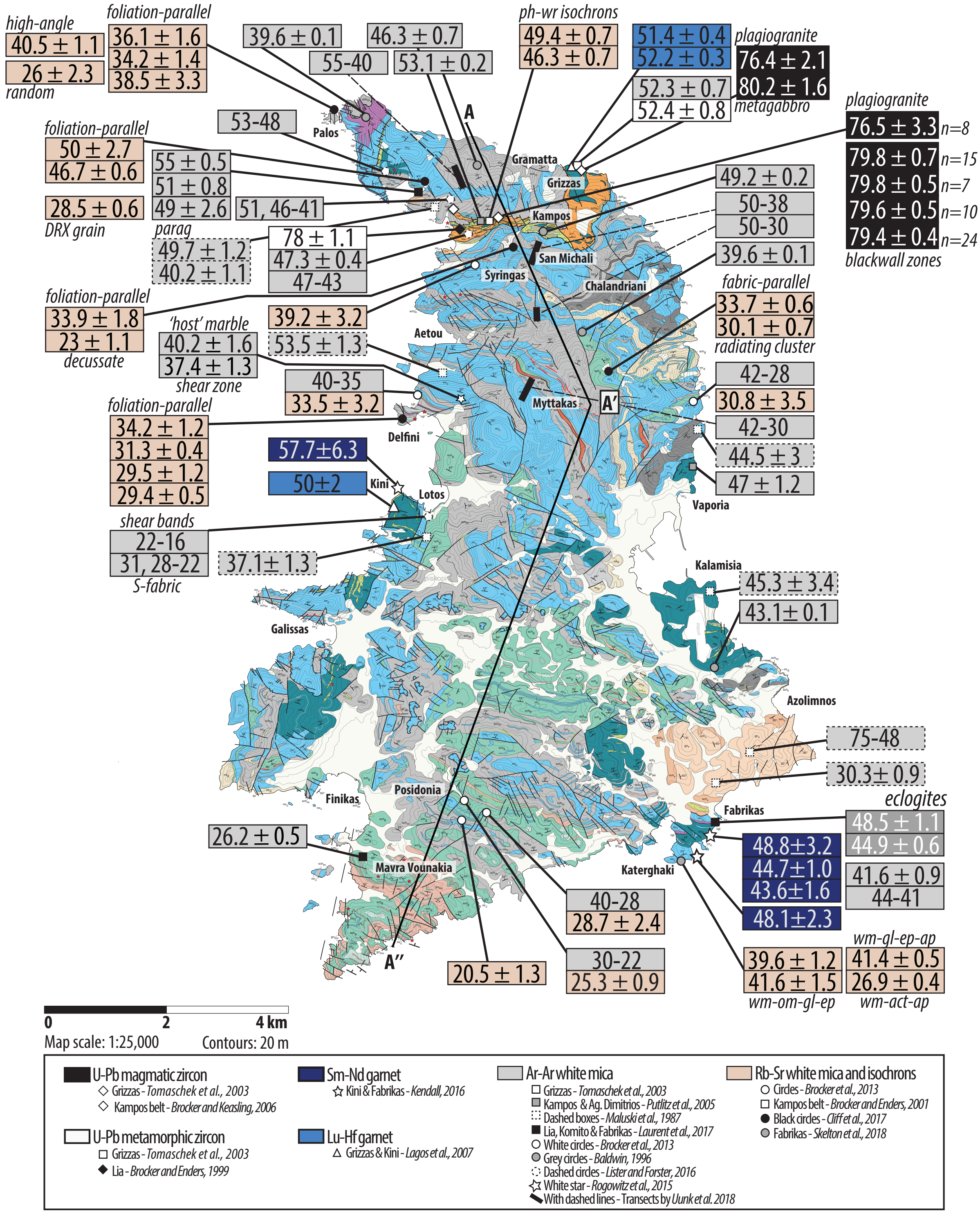

Figure A1: Compilation of the locations and ages from published metamorphic geochronology (and magmatic ages from Kampos), from references listed in grey box and discussed in Section 2. Samples are projected onto the cross-section line A-A'-A" as shown in Figure 11. Sample locations are coded by color and shape according to citation, and box colors around reported ages correspond to different chronometers. Abbreviations for boxes with notes indicating the sample's micro-structural and/or lithologic context are as follows: DRX = dynamically recrystallized; wm=white mica, ph=phengite, om=omphacite, gl=glaucophane, ep=epidote, act=actinolie, ap=apatite, wr=whole rock.

#	Method	Closure Temp	Sample Name and Description	GPS Coordinates^	Location	Age	Uncertainty	Notes	Interpretation*	Ref.
1	**U-Pb zircon**	>750°C	metagabbro		Grizzas	80.2	1.6		magmatic crystallization (protolith)	[1]
2			meta-plagiogranite dyke		Grizzas	76.4	2.1		magmatic crystallization (protolith)	[1]
3			meta-plagiogranite breccia		Grizzas	52.4	0.8	skeletal rims, low Th/U	HP metamorphism	[1]
4			1081 omphacitite		Kampos belt	78	1		interpreted as HP met, but likely magmatic	[2]
5			4017 plagiogranite in meta-gabbro	37°29.704'N, 024°54.005'E	Kampos belt	77	1	oscillatory zoned zircons	interpreted as HP met, but likely magmatic	[3]
6						76.1	1.2			[3]
7						76.6	1.3			[3]
8						76.6	1.1			[3]
9						76.9	1.1			[3]
10						75	1.2			[3]
11						76.1	1.3			[3]
12						78	1.1			[3]
					average	76.5	3.3			
13			3148 Jadetite: albite + jadeite; accessories	37°29.362'N, 024°54.335'E	Kampos belt blackwall zone	80.3	0.9	oscillatory zoned zircons (likely		[3]
14			titanite, allanite, zircon, white mica, chlorite,			78.7	0.9	magmatic, or seafloor		[3]
15			apatite			80.0	0.9	metasomatism)		[3]
16						78.6	0.7			[3]
17						78.2	0.8			[3]
18						80.6	0.8			[3]
19						78.6	0.7			[3]
20						79.4	0.9			[3]
21						80.7	0.7			[3]
22						79.9	0.7			[3]
23						80.6	0.7			[3]
24						79.8	0.6			[3]
25						77.3	1.4			[3]
26						80.8	0.7			[3]
27						82.9	2.2			[3]
					average	79.8	3.8			
					reported weighted mean	79.8	0.7			
28			3149 Omphacitite: omph, alb, wm, ttn, chl,	37°29.362'N, 024°54.335'E	Kampos belt blackwall zone	79.7	0.5	oscillatory zoned zircons (likely		[3]
29			opaques			79.9	0.3	magmatic, or seafloor		[3]
30						78.5	0.8	metasomatism)		[3]
31						78.4	0.4			[3]
32						76.7	0.5			[3]
33						79.9	1.0			[3]
34						77.6	1.0			[3]
					average	78.7	1.8			
					reported weighted mean	79.8	0.5			
35			3151 Glaucophanite: glaucophane; subordinate	37°29.362'N, 024°54.335'E	Kampos belt blackwall zone	78.9	0.8	oscillatory zoned zircons (likely		[3]
36			amounts of omph, rt, ttn, zrc, all, wm, bt			79.9	0.8	magmatic, or seafloor		[3]
37						78.9	1.2	metasomatism)		[3]
38						79.1	1.2			[3]
39						82.2	1.3			[3]
40						80.0	0.8			[3]
41						78.4	0.7			[3]
42						79.2	0.7			[3]
43						80.3	0.9			[3]
44						80.6	1.0			[3]
					average	79.8	3.0			[3]

Table A2: Compilation of published metamorphic geochronology for Syros Island. Data are plotted against closure temperature in Figure 3B. References: (1) Tomaschek et al. (2003), (2) Bröcker and Enders (1999), (3) Bröcker and Keasling (2006)...

					reported weighted mean	79.6	0.5			
45			3152-A Chlorite Actinolite Zone: chl, act, rt,	37°29.362'N, 024°54.335'E	Kampos belt blackwall zone	77.5	1.8	oscillatory zoned zircons (likely		[3]
46			zrc, wm, ap			80.4	1.3	magmatic, or seafloor		[3]
47						82.3	2.0	metasomatism)		[3]
48						78.5	1.1			[3]
49						80.4	2.1			[3]
50						77.7	1.4			[3]
51						78.2	1.3			[3]
52						79.7	0.7			[3]
53						81.3	1.1			[3]
54						80.0	1.8			[3]
55						78.9	1.1			[3]
56						84.0	3.7			[3]
57						79.9	1.0			[3]
58						81.1	0.8			[3]
					average	80.0	6.2			
59			3152-B Chlorite-Actinolite Zone:	37°29.362'N, 024°54.335'E	Kampos belt blackwall zone	76.2	1.3	oscillatory zoned zircons (likely		[3]
60						81.3	1.0	magmatic, or seafloor		[3]
61						79.5	1.0	metasomatism)		[3]
62						78.4	1.1			[3]
63						76.9	1.3			[3]
64						73.1	0.7			[3]
65						79.6	0.5			[3]
66						79.3	1.3			[3]
67						78.5	0.8			[3]
68						79.1	0.7			[3]
					average	78.2	3.2			[3]
					reported weighted mean	79.4	0.4			
69	**Sm/Nd garnet**	600-700°C	06MSY-6E rutile-bearing eclogite		Kini	57.7	6.3	8 grt-leachate-wr isochron	garnet growth	[4]
70			14RSY-8A mica-rich eclogite		Fabrikas	48.8	3.2	4 grt-wr isochron	garnet growth	[4]
71			14BSY-35D mica-rich eclogite, float		Fabrikas	48.1	2.3	bulk; grt-grt-grt-wr isochron	garnet growth	[4]
72			14BSY-35D mica-rich eclogite, float		Fabrikas	47.1	3	rim of garnet, microdrilled; rim-rim-rim pwd-matrix isochron	garnet growth	[4]
73			14BSY-38A, eclogite boudin in quartz schist matrix		Fabrikas	44.7	1	5 grt-wr isochron	garnet growth	[4]
74			14BSY-37A eclogite, float		Fabrikas	43.6	1.6	5 grt-wr isochron	garnet growth	[4]
75	**Lu/Hf garnet**	600°C	Ag31: meta-igneous breccia		Grizzas	52.2	0.3	wr-zrn-ttn-'leftover'-4grt isochron; table top digestion	early garnet crystallization (Lu fractionation)	[5]
76			Ag85: meta-igneous breccia		Grizzas	51.4	0.4	wr-omph-'leftover'-4grt isochron; table top digestion	early garnet crystallization (Lu fractionation)	[5]
77			Ap21: glaucophane eclogite		Kini	50	2	wr-omph-'leftover'-3grt isochron; table top digestion	early garnet crystallization (Lu fractionation)	[5]
78	**Rb-Sr WM**	~500°C +/- 50	5243 Ph-Chl-Ab-Qz-Ep-Cal-Ttn-Gr schist	N 37° 23.501' E 24° 54.633'	South Central, Posidonia	28.7	2.4	ph-cal isochron	ages record continuous (partial) resetting of isotopic	[6]
79	**& isochrons**		5244 Ph-Chl-Ab-Qz-Ep-Cal-Ttn schist	N 37° 23.265' E 24° 54.365'	South Central, Posidonia	20.5	1.3	ph-ep-ab isochron	systematics and/or (re)crystallization of white mica	[6]
80			5246 Ph-Pg-Chl-Ab-Qz-Ep-Cal-Ttn schist	N 37° 23.643' E 24° 54.151'	South Central, Posidonia	25.3	0.9	ph-ep-cal isochron	during exhumation and greenschist facies	[6]
81			5267 Ph-Chl-Ab-Qz-Cal-Ttn schist	N 37° 27.734' E 24° 53.898'	N. Delfini	33.5	3.2	ph-cal isochron	retrogression	[6]
82			SYR015 Ph-Pg-Chl-Ab-Qz-Ep-Cal-Ttn schist	N 37° 27.497' E 24° 56.767'	N. of Agios Dimitrios	30.8	2.9	ph-par-ep isochron		[6]

Table A2: Continued. References: (4) Kendall (2016), (5) Lagos et al. (2007), (6) Bröcker et al. (2013)...

83	5831 Ph-Chl-Ab-Qz-Ep-Cal-Ttn-Act schist	N 37° 28.808' E 24° 54.723'	Syringas (S. of Kampos)	39.2	3.2	ph-ep-ab-cal isochron		[6]
84	1081 Omphacitite		Kampos belt	49.4	0.7	ph-wr isochron	interpretation not provided in text; likely crystallizatio and/or incipient recrystallization	[7]
85	1083 Omphacitite		Kampos belt	46.3	0.7	ph-wr isochron		[7]
86	63286 - calcschist, cal-ph-glc-qz-ab		Palos, Diapori	35.2	1	4 fabric-parallel phengites, 1 randomly oriented aggregate, 2 calcite	Purposefully targeted extensional blueschist- and greenschist-facies fabrics. Phengites were microdrillec from specific microstructures in calc schists and metabasites. Interpreted as "continuous deformation on a regional scale" and exhumation-related (re-)crystallization.	[8]
87				37.4	0.8	*single phengite*		[8]
88				34.4	0.8	*single phengite*		[8]
89				37.5	1.7	*single phengite*		[8]
				36.1	**1.6**	mean of above 4 grains		
90				26	2.3	*randomly oriented phengite*		[8]
91	63297 - calcschist, cal-ph-glc-ep-qz-ab		Palos, Diapori	35.6	0.5	4 fabric-parallel phengites, 1 grain at high angle to fabric, 3 calcite		[8]
92				32.2	0.3	*single phengite*		[8]
93				34.6	1.1	*single phengite*		[8]
94				34.4	0.5	*single phengite*		[8]
				34.2	**1.4**	mean of above 4 grains		
95				40.5	1.1	*high angle phengite, wrapped by foliation-parallel phengites*		[8]
96	63300 - calcschist, cal-ph-glc-chl-qz-ab		Palos, Diapori	41.8	2	4 fabric-parallel phengites, 1 calcite		[8]
97				37.1	0.4	*single phengite*		[8]
98				40.5	0.4	*single phengite*		[8]
99				34.4	0.5	*single phengite*		[8]
				38.5	**3.3**	mean of above 4 grains		
100	63287a - calcschist, cal-ph-grt-dol-glc-qtz-ep-ttn		Grammata	52.5	0.8	6 fabric-parallel phengites, 4 calcite		[8]
101				52.1	1.1	*single phengite*		[8]
102				46.9	2.3	*single phengite*		[8]
103				48.6	0.5	*single phengite*		[8]
				50	**2.7**	mean of above 4 grains		
104	63287b			47.1	0.6	*single phengite*		[8]
105				46.2	1.3	*single phengite*		[8]
				46.7	**0.6**	mean of above 2 grains		
106	63287a			28.5	0.6	*single phengite; has fine grained recrystallized phengite next to it*		[8]
	S97/234 - greenschist, ab-chl-ph-ep-qz-cal, rare glc		N. Oros Syringas			4 fabric-parallel phengites + 3 ep; 1 grain from decussate pressure shadow adjacent to garnet		
107				33.6	0.4	pseudomorph		[8]
108				29.4	2.3	*single phengite*		[8]
109				34	0.5	*single phengite*		[8]
				33.9	**1.8**	weghted mean of above 3 grains		
110				23	1.1	*decussate phengite*		[8]
111	63301 - greenschist, qz-ph-chl-ab-cal-dol-ttn-ap pg		Foinikia	30.1	0.7	*decussate/radiating cluster at high angle to fabric*; plus 2 cal + 2 ttn		[8]
112				33.7	0.6	*composite fabric-parallel sample*		[8]
113	63310 - blueschist, ep-glc-ph-cal-qz-ab-ttn-tour chl		Delfini	31.3	0.4	2 phengite composite samples aligned with schistosity; 3 ep + 2 cal		[8]

Table A2: Continued. References: (7) Bröcker and Enders (2001), (8) Cliff et al. (2016)...

114						29.5	1.2	*composite #2*		[8]
115			63314 - blueschist, ph-glc-qz-ep-ttn-chl-ab-cal-ap		Delfini	34	1.7	8 fabric-parallel phengites, 1 epidote, 1 apatite, 2 ttn, lots of ep inclusions		[8]
116						39.5	3.1	*single phengite*		[8]
117						33.9	1.2	*single phengite*		[8]
118						36.3	1.3	*single phengite*		[8]
119						34.3	1.2	*single phengite*		[8]
120						33.7	0.6	*single phengite*		[8]
						34.2	**1.3**	regression of above six grains w. epidote		
121						29.7	0.7	*single phengite*		[8]
122						29.2	0.7	*single phengite*		[8]
						29.4	**0.5**	weighted mean of youngest grains		
				GPS points approximated from map, not provided in text						
123			15-SY-03 glaucophane eclogite	37°23'20.99"N 24°57'13.35'	Fabrikas	39.6	1.2	4wm-omph-glauc-ep isochron	Interpreted as peak metamorphism, but probably	[9]
124			15-SY-05 glaucophane eclogite		Fabrikas	41.6	1.5	4wm-omph-glauc-ep-ap isochron	'reworked' during exhumation	[9]
125			15-SY-01-02 epidote blueschist	37°23'17.66"N 24°57'9.50"I	Fabrikas	41.36	0.45	4wm-glauc-ep-ap isochron		[9]
126			17 FB 05 greenschist		Fabrikas	26.9	0.4	wm-act-ap isochron	greenschist recrystallization	[9]
127	**Ar/Ar WM**	~400-450°C	AG144 and BSY260 meta-plagiogranite dyke & breccia		Grizzas	52.3	0.7	Ar steps yield apparent ages between 30-54 Ma	prograde crystallization?	[1]
128		550°C (Ref. 11)								
129			SY01 metachert		North of Delfini	53.5	1.3		prograde?	[10]
130			SY15 metatuff		North of Ag. Dimitrios	44.5	3		(partial) resetting and/or recrystallization	[10]
131			SY30F eclogitic metagabbro		W. Kampos belt	40.2	1.1		(partial) resetting and/or recrystallization	[10]
132			SY501 omphacitic metagabbro		North of Fabrikas	30.3	0.9		(partial) resetting and/or recrystallization	[10]
133			SY7 calcschist-metatuff		East of Kini	37.1	1.3		(partial) resetting and/or recrystallization	[10]
134			SY66 omphacitic metagabbro		Airport	45.3	3.4		(partial) resetting and/or recrystallization	[10]
135			SY08 calcschist		W. Kampos belt	49.7	1.2	paragonite	Prograde? Or partial resetting?	[10]
136			SY20 metagranite		Vari	48 to 75		no Eocene HP history in Vari Unit	Metamorphic crystallization	[10]
137			S07-14 Grt-Omph blueschist	37.4992/24.8935	Grammata	50.84	0.84	single grain (2)	peak conditions	[11]
138						49.44	2.62		peak conditions	[11]
139			S07-16 Grt-Chl micaschist	37.4992/24.8935	Grammata	55.04	0.56	concentrate	peak conditions	[11]
140			S07-01 Gln-Ep micaschist	37.3891/24.9534	Fabrikas	41.65	0.95	single grain	recrystallization	[11]
141			S07-02 Blueschist	37.3891/24.9534	Fabrikas	43.51	0.56	single grain (2)	recrystallization	[11]
142						41.95	0.77		recrystallization	[11]
143			S07-04 Gln eclogite	37.3891/24.9534	Fabrikas	44.89	0.65	single grain	peak in intermediate unit?	[11]
144			S07-04bis Gln eclogite	37.3891/24.9534	Fabrikas	40.29	0.73	single grain	recrystallization	[11]
145			S07-jojo Gln eclogite	37.3891/24.9534	Fabrikas	48.5	1.1	in situ (10), isochron reported	peak in intermediate unit?	[11]
146			S07-17 Alb-Chl micaschist	37.3791/24.8819	NW of Komito Beach	26.12	0.52	single grain	recrystallization	[11]
147			5267 Ph-Chl-Ab-Qz-Cal-Ttn schist	N 37° 27.734' E 24° 53.898'	N. Delfini	35-40		10 grains	Ar ages span 41-27; Rb-Sr ages span 34-20	[6]
148			SYR015 Ph-Pg-Chl-Ab-Qz-Ep-Cal-Ttn schist	N 37° 27.497' E 24° 56.767'	N. of Agios Dimitrios	28-42		12 grains, excludes 1 outlier	Ages record continuous (partial) resetting of isotopic	[6]
149			5243 Ph-Chl-Ab-Qz-Ep-Cal-Ttn-Gr schist	N 37° 23.501' E 24° 54.633'	South Central, Posidonia	28-40		12 grains	systematics and/or (re)crystallization of white mica	[6]
150			5246 Ph-Pg-Chl-Ab-Qz-Ep-Cal-Ttn schist	N 37° 23.643' E 24° 54.151'	South Central, Posidonia	22-30		13 grains	during exhumation and greenschist facies	[6]
151			89646 quartzite		Palos	39.6	0.1	total fusion age, gradient in apparent ages 31 to 41.2	partial loss profile and/or recrystallization after HP ev	[12]
152			89644 glaucophane-marble schist		Kampos belt	53.1	0.2	phengite, total fusion age, graident 52.4 to 55	HP event	[12]
153			89642 retrograde eclogite		Kampos belt	49.2	0.2	phengite, flat spectra, weighted mean	HP event	[12]

Table A2: Continued. References: (9) Skelton et al. (2019), (10) Maluski et al. (1987), (11) Laurent et al. (2017), (12) Baldwin (1996)...

154	89645 retrograde blueschist		Central	39.6	0.1	total fusion age, gradient 34.8 to 42.4	partial loss profile and/or recrystallization after HP event	[12]
155	89649 retrograde blueschist		Airport	43.05	0.12	total fusion age, gradient 40 to 44.2	partial loss profile and/or recrystallization after HP event	[12]
156	SY-7 phengite-rich eclogite		Kampos belt	46.3	0.7	in-situ UV-laser ablation; weighted mean laser fusion ages (n=27)	paper says prograde; could be partially reset, some ages are older (50-52)	[13]
157	SY-25 omphacite-rich meta-gabbro		Agios Dimitrios	47	1.2	in-situ UV-laser ablation; weighted mean laser fusion ages (n=30)	paper says prograde; our observations of Ag. Dim indicate this is likely recrystallization and/or neo-crystallization	[13]
							All ages from [14] are interpreted as crystallization ages related to different microstructures using the 'method of asymptotes and limits'	
158	AG10-31 garnet mica schist	37° 30.081'N 24° 53.173'E	N. of Gramatta	53-48		Δ1B + early Δ1C decussate + post-Δ1C shear zone, pheng-muscovite	timing of Δ1B event	[14]
159	AG10-14 garnet mica schist	37° 29.613'N 24° 54.295'E	N. Kampos belt	51, 46-41		Δ1B + Δ1C + post-Δ1C, older phengite component, younger muscovite component	muscovite component records Δ1C growth and post-Δ1C shearing	[14]
160	AG10-15 Δ1C white mica in boudin neck	37° 29.537'N 24° 54.416'E	Kampos belt	43-47		late Δ1C porphyroblastic white mica from dilational zone next to mega-boudin		[14]
161	AG10-16 early Δ1C decussate wm + titanite	37° 29.546'N 24° 54.404'E	Kampos belt	47.3	0.4	early Δ1C decussate white mica, from edge of mega-boudin		[14]
162	AG10-26S wm-qz-ab-chl-calc greenschist	37° 26.582'N 24° 54.166'E	E. of Kini, roads above Lotos	31, 28-22		Dominant fabric in greenschist facies schist (post-Δ1D and Δ2)	older phengite component; younger muscovite component	[14]
163	AG10-26C wm-qz-ab-chl-calc greenschist	37° 26.582'N 24° 54.166'E	E. of Kini, roads above Lotos	16-22		Extensional shear bands cutting greenschist fabric (relict post-Δ1D + Δ2 + post-Δ2)	muscovite component	[14]
	Kampos transect - *graphite-rich Lws-Grt blueschists and micaschists, with intercalated calcite and siliceous layers*		N. of Kampos belt			*single grain fusion experiments*		
164	12SR100: graphite-rich Lws-Grt-Gln micaschist, static gscht.	N37° 29.855', E24° 54.369'		55-48		broad uniform age		[15]
165	12SR57: siliceous marble; Phg+Gln+ Ep+Qz+ Ttn+Chl	N37° 29.856', E24° 54.220'		55-48		broad uniform age		[15]
166	12SR02: graphite-rich Lws(ps)-Grt-Gln micaschist; ttn in foliation	N37° 29.942', E24° 54.566'		52-45		wide uniform age		[15]
167	12SR97: Phg+Qz+Ep+Ttn bearing marble	N37° 29.827', E24° 54.628'		52-45		wide uniform age		[15]
168	12SR03: phg-bearing marble with columnar aragonite pseudomorphs	N37° 29.821', E24° 54.744'		55-40		heterogeneous		[15]
	San Michalis transect - *marble-schist-marble sequence, middle unit contains pyrite-bearing schists and gneisses, graphite-rich Lws-Grt-Gln micaschists and quartzitic rocks, locally with static greenschist overprint*		S. of Kampos belt			*single grain fusion experiments*		
169	12SR96: Lws-Grt-Gln micaschist, static gscht	N37°29.393', E24°54.891'		49-45		narrow range		[15]
170	12SR04: Lws-Grt-Gln micaschist, static gscht	N37°29.359', E24°55.125'		48-40		heterogeneous		[15]
171	12SR13b: carbonated and brecciated blueschist; Ctd-Gln, Ep	N37°29.328', E24°55.223'		48-40		heterogeneous		[15]

Table A2: Continued. References: (13) Putlitz et al. (2005), (14) Lister and Forster (2016), (15) Uunk et al. (2018).

172	12SR92: Phg-bearing marble; aragonite pseudomorphs	N37°29.395', E24°54.975'		48-40		heterogeneous		[15]
173	12SR93: Phg-bearing marble; aragonite pseudomorphs	N37°29.343', E24°54.904'		50-38		heterogeneous		[15]
	Syringas transect 1 and 2 *- intercalated schist-marble sequence; vary from felsic to Ep-blueschists to pervasively overprinted greenschists*		Sy1 west coast; Sy2 central			*single grain fusion experiments*		
174	12SR78: crenulated felsic mica schist	N37°28.830', E24°53.901'		48-42		narrow uniform age		[15]
175	12SR82: calcschist, Phg+Qz+Chl	N37° 28.666', E24° 55.119'		38-31		intermediate		[15]
176	12SR81: Phg-bearing marble, aragonite pseudon	N37° 28.664', E24° 55.118'		50-40		heterogeneous		[15]
	Myttakas transect *- upper and lower marbles bookending felsic schists and gneisses and intermediate-mafic rocks ranging from ep-grt blueschists to pervasively overprinted greenschists*		NE of Delfini, central			*single grain fusion experiments*		
177	12SR19: Phg-bearing marble	N37°27.889', E24°55.225'		40-39		narrow uniform age		[15]
178	12SR16: Ep-Ab blueschist (+Grt), partial greenschist overprint	N37°27.796', E24°55.147'		40-39		narrow uniform age		[15]
179	12SR20: felsic Ab gneiss; Phg+Qz foliation, Ab porphyroblasts	N37°27.871', E24°55.199'		42-30		heterogeneous		[15]
180	12SR18b: intermediate-to-mafic Grt-Ep blueschist; Phg+Gln+Ep matrix	N37°27.841', E24°55.174'		42-30		heterogeneous		[15]
181	12SR18a: blueschist, static greenschist; Phg+Qz matrix	N37°27.811', E24°55.171'		42-30		heterogeneous		[15]
182	12SR17: greenschist mylonite, fine-grained Act+Chl matrix, Ab blasts	N37°27.798', E24°55.154'		42-30		heterogeneous		[15]
183	12SR15: siliceous marble, Ep+Phg+Qz, aragonite pseudomorphs	N37°27.808', E24°55.101'		42-30		heterogeneous		[15]
184	Calcite marble intercalated with quartz and dolon ?		N. of Delfini	40.2	1.6	Si apfu 3.4-3.6	Authors hypothesized these would be Miocene due to strong EW stretching. Interpreted Eocene ages as evidence that the phengite was not reset during Miocene deformation; our results suggest these could be DT2 greenschist deformation	[16]
185	Shear zone			37.4	1.3			

Table A2: Continued. References: (16) Rogowitz et al. (2015).

al., 2017), 37 ^{87}Rb/^{86}Sr white mica (Cliff et al., 2016), and 1 U-Pb SHRIMP zircon age which is a weighted mean of 7 analyses (Tomaschek et al., 2003). The isochrons include 5 Sm-Nd garnet-whole rock (Kendall, 2016), 3 Lu-Hf garnet-omphacite-whole rock (Lagos et al., 2007), 10 multi-mineral and 2 phengite-whole rock ^{87}Rb/^{86}Sr (Bröcker & Enders, 2001; Bröcker et al., 2013; Skelton et al., 2019), and one 10-point inverse ^{40}Ar/^{39}Ar (Laurent et al., 2017)). The ^{40}Ar/^{39}Ar ages included in the final compilation are in-situ analyses of grains in thin section (used to construct the 10-point inverse isochron), and strong plateaus from step-heating experiments of grains extracted from well-characterized microstructural domains (Laurent et al., 2017). We excluded: 1 Sm-Nd isochron with low ^{147}Sm/^{144}Nd ratio and potential for contamination due to the presence of an off-isochron inclusion (cf. Kendall, 2016); and 50 ^{40}Ar/^{39}Ar ages that exhibit one or more of the complications described above (Maluski et al., 1987; Baldwin, 1996; Tomaschek et al., 2003; Putlitz et al., 2005; Bröcker et al., 2013; Lister & Forster, 2016; Laurent et al., 2017; Uunk et al., 2018).

Lagos et al. (2007) presented Lu-Hf garnet growth ages from meta-igneous rocks at Grizzas and Kini, showing that those blueschist-eclogite localities reached peak metamorphic conditions at 51.9±1.4 Ma and 50±2 Ma, respectively. New fabric ages from Kini blueschists (this study, 52.62 ± 0.64 Ma) overlap with garnet growth ages at Grizzas and Kini, and with the SHRIMP age determined by Tomaschek et al. (2003) for Grizzas metamorphic zircons.

Fabrikas eclogites record Sm-Nd garnet crystallization ages of ∼45±3 Ma (Kendall, 2016). 'Bulk' garnet ages (48.1±2.3 Ma) overlap within error with 'rim' ages (47.1±3 Ma), providing evidence for rapid, pulsed garnet crystallization that is distinctly younger than Grizzas and Kini. Garnet growth ages are consistent with ^{40}Ar/^{39}Ar ages of foliation-forming white mica in Fabrikas glaucophane-bearing eclogites (48.5±1.1 Ma to 44.9±0.6 Ma, Laurent et al. (2017)).

Retrograde blueschist-facies fabric ages range from ∼50-40 Ma, and are captured by: (1) Phengite-whole rock Rb-Sr isochrons from omphacitites at Kampos (49.4±0.7 Ma and 46.3±0.7 Ma, Bröcker and Enders (2001)) and Rb-Sr ages of micro-drilled phengites from glaucophane-bearing calcschists at Gramatta (50.5±3.1 Ma and 47.3±1.2 Ma, Cliff et al. (2016)); (2) A new multi-mineral Rb-Sr isochron from Azolimnos (44.71 ± 0.43 Ma, this study); (3) A Rb-Sr isochron from omphacite-blueschists (41.5±1.5 Ma, Skelton et al. (2019)) and ^{40}Ar/^{39}Ar ages of foliation-forming white mica in retrogressed Fabrikas eclogites and bluechists (44.9±0.65 Ma to 40.3±0.7 Ma, n=4, Laurent et al. (2017)).

Retrograde greenschist-facies fabric ages range from ∼42-36 Ma, and are captured by Rb-Sr multi-mineral isochrons and Rb-Sr ages of foliation-forming micro-drilled phengites from greenschists and calcschists from the following locations: (1) Palos (40.5±1.1 Ma to 34.2±1.4 Ma, Cliff et al. (2016)); (2) Syringas (39.2±3.2 Ma, Bröcker et al. (2013); 33.9±1.8 Ma Cliff et al. (2016)); (3) North of Delfini (33.7±0.6 Ma, Cliff et al. (2016); 33.5±3.2 Ma and 30.8±2.9 Ma, Bröcker et al. (2013)); (4) Delfini (34.2±1.3 Ma to 29.4±0.5 Ma; Cliff et al. (2016); 36.47±0.11 Ma, this study); (5) Fabrikas (26.9±0.4 Ma, Skelton et al. (2019)); and (6) Posidonia (28.7±2.4 Ma, 25.4±0.9 Ma, 20.5±1.3 Ma, Bröcker et al. (2013)).

Appendix B Electron Microprobe Techniques and Data Treatment

B1 Qualitative X-Ray Mapping

Qualitative X-Ray compositional maps were acquired on the JEOL JXA-8200 electron microprobe at the University of Texas at Austin. Polished 30 μm thin sections were analyzed using a 15 kV accelerating voltage, focused beam, 300 nA current, 6 μm step size, and 1 ms dwell time. X-ray maps for Si, Al, Ca, Mg, Fe, Na, K, Mn, Ti, and P were collected. Post-processing to produce false color compositional maps creation was done in ImageJ software by merging element channels with assigned colors.

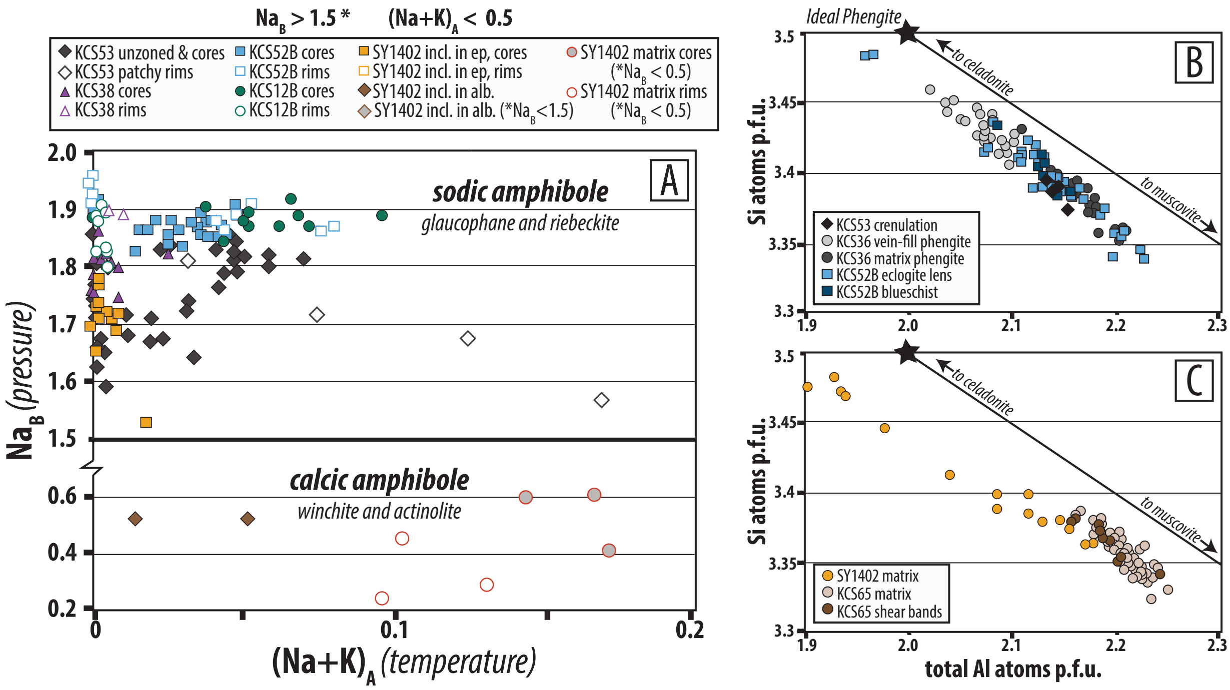

Figure B1: Quantitative EPMA results for (A) amphiboles and (B,C) white micas. (A) Na_B and $(Na+K)_A$ in amphibole are qualitative indicators of pressure and temperature, respectively. Temperature is less reliable since all of these amphiboles are very 'cold' (i.e. crystallize at <500°). Sodic amphiboles correspond to D_S and D_{T1}, and calcic amphiboles correspond to D_{T2}; see text for significance of core-rim zonations and compositional trends during deformation. (B) D_S and D_{T1} white mica chemistry. Elevated Si apfu indicates HP metamorphism. (C) D_{T2} white mica chemistry. Grains cluster towards a lower Si apfu on average, which reflects more pervasive recrystallization under lower P conditions. Intergrown phengite and paragonite is common during all deformation stages. CBU samples do not contain the limiting assemblage required for Si-in-phengite geobarometry calibrated by (Massonne & Schreyer, 1987). However, they do contain other stable Fe-Mg buffering phases (e.g. epidote, amphibole), so within a given sample and between samples of similar bulk compositions, Si variability is a reasonable measure of *relative* changes in pressure, not absolute. Samples in (B) are all meta-mafics, SY1402 in (C) is meta-mafic, KCS65 in (C) is a quartz-rich mixed meta-volcanic/meta-sediment.

B2 Quantitative Point Analyses

Quantitative analyses were collected for representative amphiboles and micas on the JEOL JXA-8200 electron microprobe at the University of Texas at Austin. Samples were selected to cover the range of interpreted structural contexts determined during field work and microstructural analysis. Polished 30 μm thin sections were analyzed using a 15 kV accelerating voltage, a 1μm beam diameter amphibole and a 10μm beam diameter for mica, 10 nA current, and counting time 30 s for all elements. Synthetic compounds and homogeneous minerals were used as standards, and secondary standards were analyzed throughout analytical procedures. Data were processed using the JEOL ZAF procedure.

Sample:	**KCS53**	***n=30***	**KCS53**	***n=6***	**KCS53**	***n=4***	**KCS53**	***n=10***	**KCS38**	***n=14***	**KCS38**	***n=2***	**KCS52B**	***n=21***	**KCS52B**	***n=4***	**KCS52B**	***n=8***	**KCS52B**	***n=3***
Context:	*matrix cores*		*cren. limb cores*		*cren. limb rims*		*cren. hinges*		*matrix cores*		*matrix rims*		*ecl, cores*		*ecl, rims*		*matrix cores*		*matrix rims*	
SiO2	58.71	0.54	58.67	0.32	57.09	1.04	58.60	0.18	59.25	0.22	58.87	0.30	58.54	0.49	58.07	0.20	58.53	0.33	58.03	0.42
Al2O3	11.23	0.20	11.07	0.05	11.00	0.12	11.07	0.15	11.78	0.26	11.59	0.13	10.83	0.72	10.11	0.10	11.26	0.20	10.72	0.43
K2O	0.01	0.01	0.01	0.01	0.03	0.02	0.01	0.01	0.01	0.01	0.00	0.00	0.00	0.01	0.00	0.00	0.01	0.00	0.00	0.00
Na2O	6.54	0.24	7.06	0.11	6.80	0.29	7.13	0.11	6.93	0.16	7.21	0.04	7.20	0.10	7.13	0.01	7.26	0.09	7.22	0.09
CaO	0.97	0.38	0.80	0.14	1.54	0.87	0.70	0.23	0.91	0.16	0.20	0.01	0.32	0.18	0.13	0.04	0.34	0.12	0.12	0.08
MnO	0.06	0.04	0.04	0.01	0.10	0.05	0.05	0.02	0.03	0.02	0.09	0.01	0.11	0.08	0.19	0.02	0.06	0.03	0.17	0.06
FeO	9.16	0.55	9.02	0.18	10.19	0.53	9.33	0.43	7.71	0.50	11.05	0.53	11.09	2.27	14.25	0.23	9.39	0.79	11.95	0.66
MgO	11.43	0.37	11.64	0.21	11.30	0.62	11.52	0.41	11.65	0.51	9.67	0.28	10.28	1.16	8.68	0.04	11.04	0.50	9.59	0.48
TiO2	0.03	0.03	0.00	0.01	0.02	0.03	0.02	0.03	0.02	0.02	0.03	0.01	0.01	0.02	0.02	0.02	0.01	0.02	0.01	0.02
Cr2O3	0.02	0.02	0.02	0.02	0.00	0.00	0.02	0.02	0.01	0.02	0.00	0.00	0.01	0.02	0.03	0.01	0.02	0.02	0.00	0.01
Total	97.89	0.47	98.30	0.26	98.05	0.13	98.44	0.25	98.29	0.49	98.68	0.26	98.37	0.27	98.58	0.15	97.88	0.31	97.79	0.71
Si	7.96	0.05	7.94	0.03	7.81	0.12	7.92	0.03	7.97	0.05	8.00	0.00	7.97	0.02	7.99	0.02	7.96	0.02	7.97	0.02
Al (iv)	0.04	0.04	0.06	0.03	0.19	0.12	0.08	0.03	0.04	0.04	0.00	0.00	0.03	0.02	0.01	0.02	0.04	0.02	0.03	0.02
K (A)	0.00	0.00	0.00	0.00	0.00	0.00	0.00	0.00	0.00	0.00	0.00	0.00	0.00	0.00	0.00	0.00	0.00	0.00	0.00	0.00
Na (A)	0.01	0.01	0.04	0.01	0.10	0.05	0.05	0.01	0.01	0.01	0.01	0.00	0.02	0.02	0.00	0.00	0.04	0.01	0.01	0.02
Na (B)	1.71	0.06	1.81	0.02	1.70	0.12	1.82	0.03	1.80	0.04	1.89	0.00	1.88	0.04	1.90	0.00	1.88	0.02	1.91	0.04
Ca (B)	0.14	0.06	0.12	0.02	0.23	0.13	0.10	0.03	0.13	0.02	0.03	0.00	0.05	0.03	0.02	0.01	0.05	0.02	0.02	0.01
Mn (B, 2+)	0.01	0.00	0.00	0.00	0.01	0.01	0.01	0.00	0.00	0.00	0.01	0.00	0.01	0.01	0.02	0.00	0.01	0.00	0.02	0.01
Fe (B, 2+)	0.11	0.04	0.07	0.01	0.06	0.01	0.07	0.02	0.04	0.04	0.07	0.00	0.06	0.03	0.05	0.01	0.07	0.02	0.05	0.04
Fe (C, 2+)	0.91	0.06	0.82	0.05	0.91	0.09	0.83	0.08	0.81	0.09	1.16	0.05	1.02	0.19	1.32	0.04	0.89	0.09	1.11	0.05
Fe (C, 3+)	0.02	0.03	0.13	0.04	0.20	0.05	0.16	0.04	0.01	0.02	0.03	0.01	0.19	0.13	0.27	0.05	0.11	0.03	0.21	0.10
Al (C, vi)	1.75	0.05	1.70	0.03	1.58	0.10	1.69	0.04	1.83	0.02	1.85	0.01	1.71	0.09	1.63	0.03	1.76	0.03	1.71	0.04
Mg (C)	2.31	0.07	2.35	0.05	2.31	0.13	2.32	0.08	2.34	0.09	1.96	0.05	2.08	0.22	1.78	0.01	2.24	0.09	1.97	0.08
Type	***Glaucophane***		***Glaucophane***		***Glaucophane***		***Glaucophane***		***Glaucophane***		***Glaucophane***		***Glaucophane***		***Mg-Riebeckite***		***Glaucophane***		***Glaucophane***	

Table B1: Amphibole mineral chemistry. Reported values are averages of the number of spots indicated by n values for each sample and micro-textural context. Uncertainties reflect the range of measured values for each micro-textural context as indicated. Cations per formula unit are calculated for ideal element partitioning for 23 Oxygen atoms.

Sample:	**KCS52B** ***n=6***	**KCS52B** ***n=7***	**KCS12B** ***n=11***	**KCS12B** ***n=8***	**SY1402** ***n=8***	**SY1402** ***n=10***	**SY1402** ***n=1***	**SY1402** ***n=2***	**SY1402** ***n=3***	**SY1402** ***n=2***
Context:	*ps, cores*	*ps, rims*	*matrix cores*	*matrix rims*	*incl. in ep, cores*	*incl. in ep, rims*	*incl. in alb (A)*	*incl. in alb (B)*	*matrix cores*	*matrix rims*
SiO2	58.58 0.20	57.72 0.42	56.32 0.22	54.03 0.63	57.78 0.15	57.30 0.69	58.28	56.52 1.24	54.13 0.26	54.93 0.96
Al2O3	11.35 0.13	10.65 0.44	10.72 0.38	4.92 1.61	8.12 0.87	8.45 1.28	8.05	2.80 0.89	3.12 0.16	2.23 0.60
K2O	0.00 0.01	0.00 0.00	0.00 0.00	0.02 0.01	0.02 0.01	0.03 0.03	0.05	0.19 0.14	0.12 0.03	0.09 0.03
Na2O	7.18 0.06	7.24 0.08	7.09 0.14	6.65 0.22	6.50 0.21	6.39 0.33	6.45	1.89 0.06	2.49 0.40	1.32 0.17
CaO	0.48 0.06	0.24 0.13	0.29 0.11	0.66 0.33	0.73 0.33	0.93 0.88	1.14	8.92 0.23	8.58 0.99	10.80 0.26
MnO	0.05 0.01	0.14 0.06	0.06 0.03	0.14 0.03	0.15 0.07	0.16 0.07	0.21	0.32 0.01	0.40 0.05	0.38 0.03
FeO	9.08 0.27	12.51 1.43	16.93 0.49	25.10 2.03	15.28 1.08	15.55 1.60	14.41	12.24 1.06	15.64 1.74	12.16 0.79
MgO	11.23 0.34	9.45 0.66	6.50 0.20	5.85 0.25	9.74 0.48	9.29 0.87	10.32	14.93 1.43	13.92 1.11	16.77 0.74
TiO2	0.01 0.02	0.01 0.03	0.02 0.03	0.02 0.02	0.02 0.03	0.03 0.03	0.00	0.00 0.00	0.02 0.01	0.01 0.01
Cr2O3	0.00 0.00	0.01 0.02	0.01 0.01	0.00 0.00	0.00 0.00	0.00 0.00	0.00	0.00 0.00	0.00 0.00	0.00 0.00
Total	97.92 0.45	97.93 0.33	97.92 0.29	97.35 0.36	98.33 0.41	98.11 0.62	98.91	97.80 0.85	98.42 0.20	98.69 0.42
Si	7.95 0.02	7.95 0.02	7.93 0.04	7.85 0.04	8.01 0.04	7.98 0.07	8.01	8.01 0.05	7.73 0.06	7.74 0.08
Al (iv)	0.05 0.02	0.05 0.02	0.07 0.04	0.15 0.04	0.01 0.02	0.03 0.05	0.00	0.02 0.02	0.27 0.06	0.26 0.08
K (A)	0.00 0.00	0.00 0.00	0.00 0.00	0.00 0.00	0.00 0.00	0.01 0.00	0.01	0.03 0.03	0.02 0.00	0.02 0.00
Na (A)	0.03 0.01	0.04 0.03	0.05 0.02	0.00 0.00	0.00 0.00	0.00 0.00	0.00	0.00 0.00	0.14 0.02	0.10 0.02
Na (B)	1.86 0.01	1.89 0.03	1.88 0.02	1.87 0.05	1.75 0.05	1.73 0.09	1.72	0.52 0.01	0.55 0.12	0.26 0.03
Ca (B)	0.07 0.01	0.04 0.02	0.04 0.02	0.10 0.05	0.11 0.05	0.14 0.13	0.17	1.35 0.01	1.31 0.15	1.63 0.03
Mn (B, 2+)	0.01 0.00	0.02 0.01	0.01 0.00	0.02 0.00	0.02 0.01	0.02 0.01	0.02	0.04 0.00	0.05 0.01	0.05 0.00
Fe (B, 2+)	0.07 0.02	0.06 0.02	0.07 0.02	0.01 0.01	0.11 0.02	0.10 0.04	0.08	0.05 0.03	0.09 0.03	0.06 0.00
Fe (C, 2+)	0.86 0.06	1.16 0.15	1.74 0.06	1.71 0.06	1.28 0.12	1.35 0.15	1.20	1.36 0.16	1.38 0.16	1.07 0.05
Fe (C, 3+)	0.10 0.03	0.22 0.08	0.18 0.03	1.33 0.28	0.39 0.16	0.36 0.18	0.38	0.03 0.05	0.40 0.05	0.30 0.06
Al (C, vi)	1.77 0.02	1.68 0.06	1.71 0.04	0.69 0.29	1.32 0.13	1.36 0.17	1.31	0.45 0.13	0.26 0.05	0.11 0.03
Mg (C)	2.27 0.06	1.94 0.12	1.36 0.04	1.27 0.05	2.01 0.10	1.93 0.17	2.12	3.15 0.25	2.96 0.23	3.52 0.13
Type	***Glaucophane***	***Glaucophane***	***Riebeckite***	***Riebeckite***	***Mg-Riebeckite***	***Mg-Riebeckite***	***Mg-Riebeckite***	***Winchite***	***Fe-Winchite***	***Actinolite***

Table B1: Continued. Amphibole mineral chemistry. Reported values are averages of the number of spots indicated by n values for each sample and micro-textural context. Uncertainties reflect the range of measured values for each micro-textural context as indicated. Cations per formula unit are calculated for ideal element partitioning for 23 Oxygen atoms.

B3 Mineral classification and formula unit calculations

Quantitative point analyses for amphiboles and white micas were converted from oxide percentage to atoms per formula unit on the basis of 22O + 2OH, and 10O + 2OH Oxygen atoms, respectively. Amphibole sub-groups and species were determined following recommendations of the Commission on New Minerals Nomenclature and Classification (CNMNC) of the International Mineralogical Association (IMA) (Hawthorne et al., 2012), and species names follow the (Leake et al., 1997) classification scheme. Classifications did not assume initial M-site$^{3+}/\sigma$M-site ratios, so ferric iron components were estimated based on charge balance by adjusting valences of Fe and Mn by automatically normalizing the cations. Data shown here commonly fell into the "sum Si to Ca=15", "sum Si to Mg=13", and "sum Si to Na=15" normalization schemes (Hawthorne et al., 2012). Hydroxyl contents were not estimated using OH=2-2Ti, and initial H_2O contents were not required for calculations. White mica ferric iron was ignored in formula calculations.

Appendix C Supplemental Field Photos

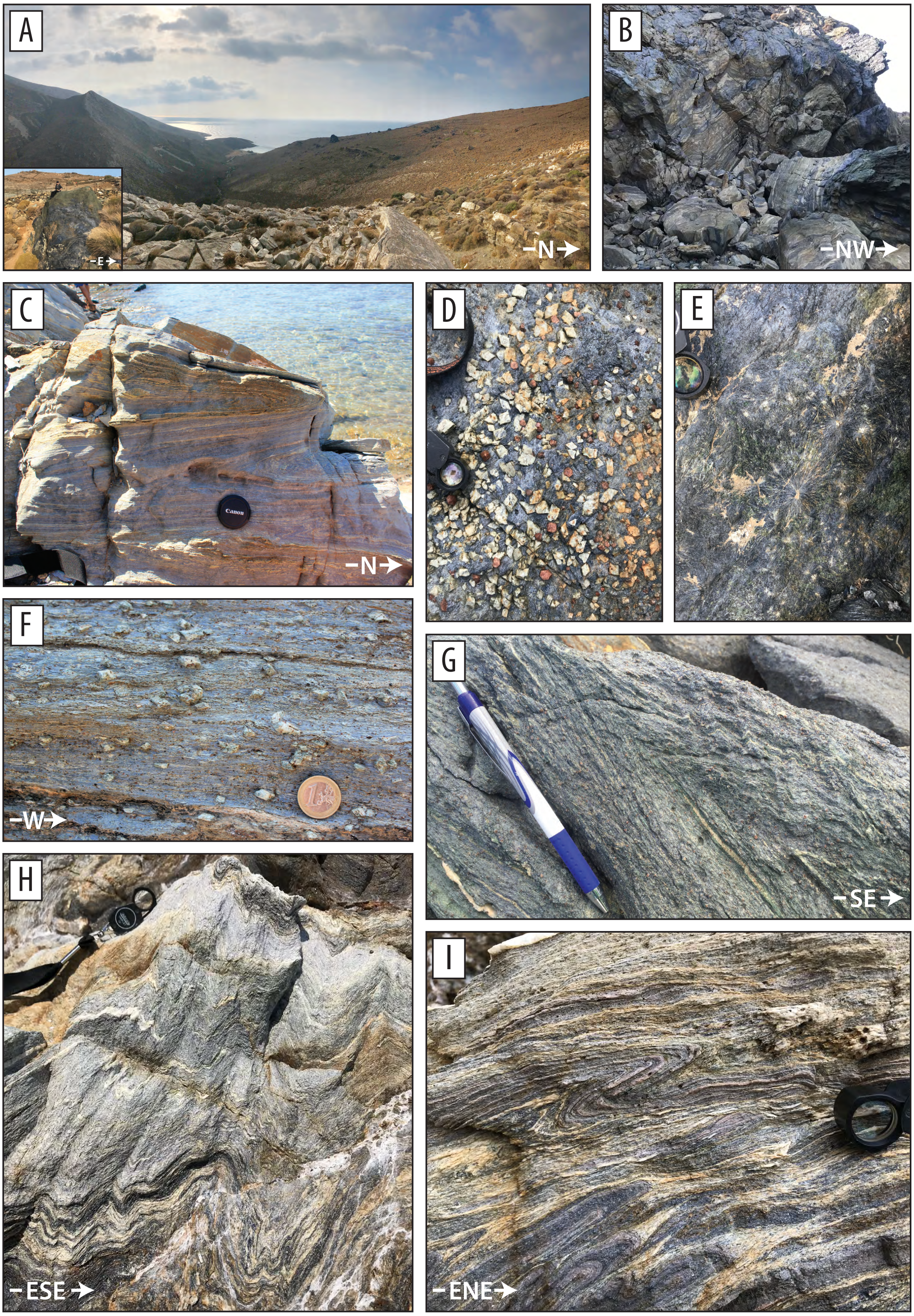

Figure C1: Caption to follow.

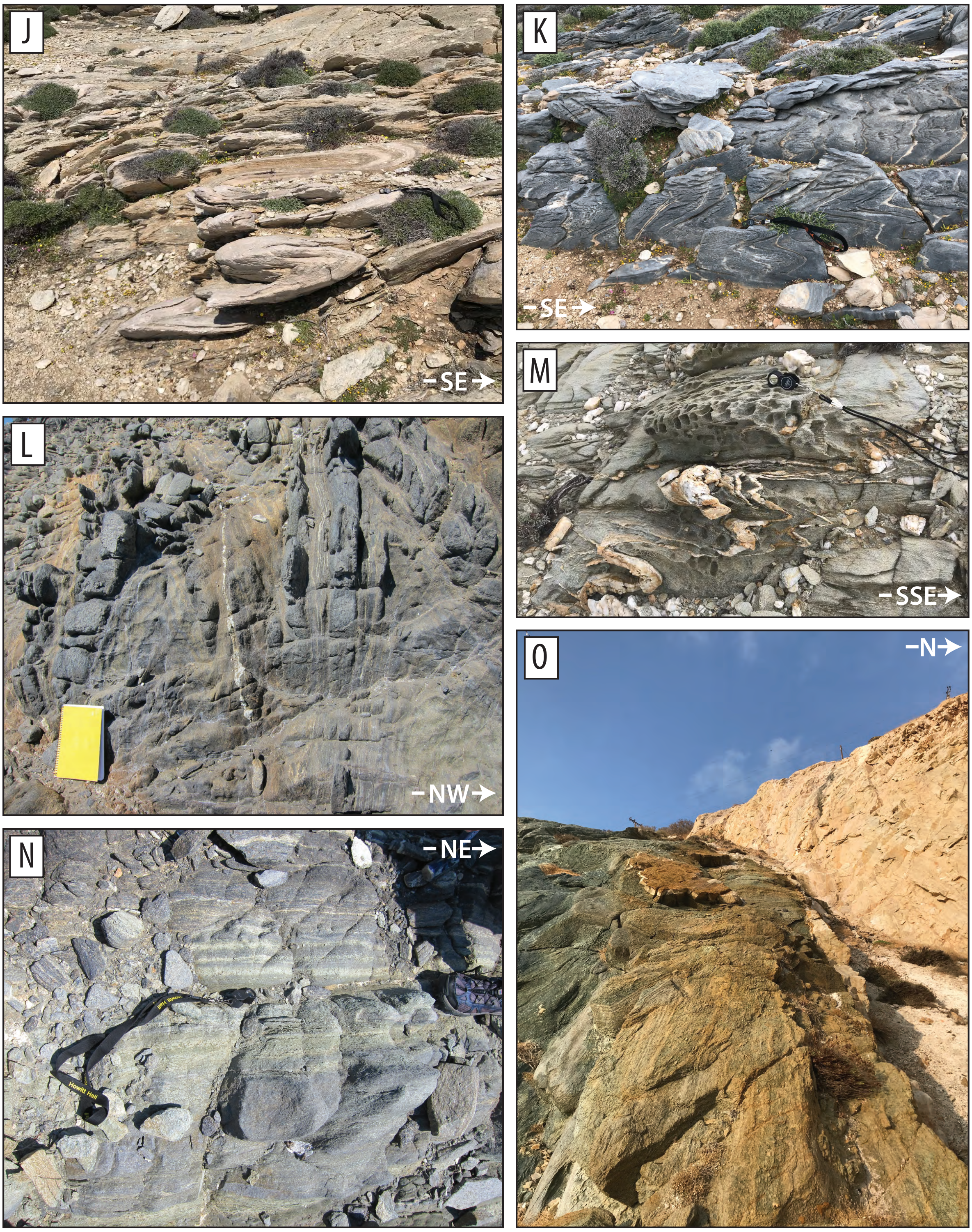

Figure C1: Caption to follow.

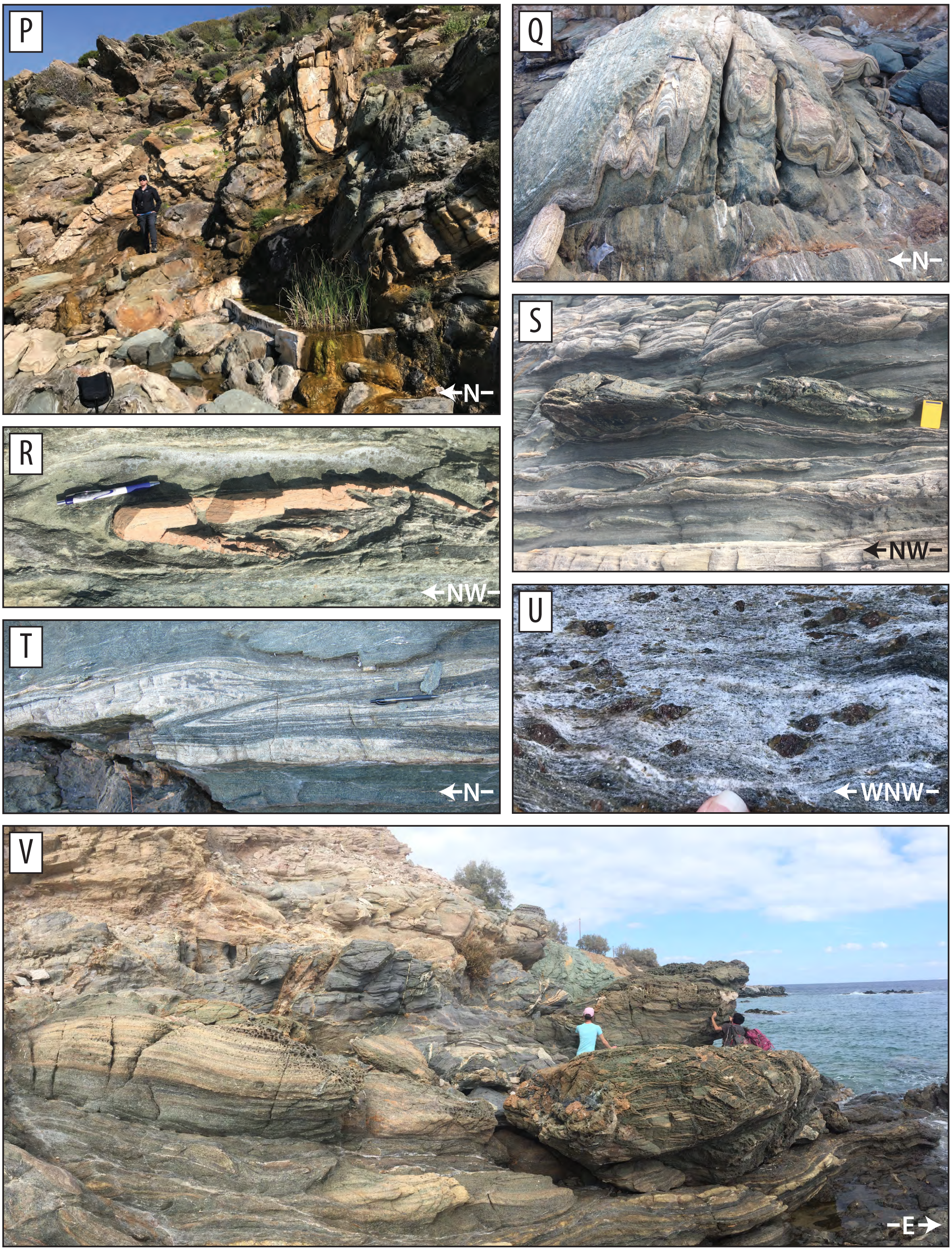

Figure C1: Caption next page.

Figure C1: (Previous pages.) Supplemental field photographs. (A) Eclogitic meta-gabbro 'blocks' pepper the Kampos Belt landscape, and are wrapped by coherent bimodal meta-volcanics (cropping out as resistant ledges in the background). Marbles in the foreground dip down towards the coastline and are structurally concordant with Belt rocks. This is a thrust contact that may have been reworked slightly during exhumation via extension, but we did not see evidence for strongly localized top-to-the-ENE shear. Inset shows example of Kampos meta-gabbro block with glaucophanite carapace. (B) Example of upright, shallowly NNE-plunging D_S folds on the shoreline W of Kampos Belt. (C) Lia Beach isoclinally-folded blueschists; the older, folded foliation is relict D_R, and isoclinal folding developed during D_S. (D) Unstrained cm-sized lawsonite pseudomorphs in Grizzas blueschist. (E) Zoom-in to margin of a Kampos Belt block showing static, radiating clusters of blue and green amphibole. (F) Unstrained D_S lawsonite pseudomorphs in Lia blueschists. (G) D_{T1} crenulation cross-cutting D_S at Kini. (H) The cores of D_{T1} upright folds in Azolimnos schists have strong axial planar cleavages associated with blueschist-to-greenschist facies retrogression. (I) Earlier D_S fabrics in Azolimnos schists record asymmetric shear in isoclinally-folded schists; pinkish layers are meta-cherts. (J) Isoclinal folds in marbles (foreground) and meta-conglomerates (background) and in meta-mafic greenschists (M) on Palos Peninsula mimic the map-scale folding seen in Fig. 2. (K) Sub-horizontal axial planar cleavages form in dolomitic blue-grey marbles during exhumation-related flattening (coaxial strain). (L) Upright D_{T1} folding at Kalamisia is associated with hinge-parallel greenschist retrogression (N) selectively permeating foliation-parallel layers. (O) Fault contact between marbles and blueschist-eclogite lithologies at Agios Dimitrios. Stretching is directly down-dip (essentially out of the page) and parallel to mullion hinges developed along the contact. Structures on either side of this contact are homogeneous. (P-S, U) Multiple generations of folding at Delfini. (P) Upright D_{T2} folding (discussed in text) develops an axial planar cleavage and hinge-parallel stretching and mineral lineations defined by quartz, epidote, and actinolite (Q). Older D_S foliations contain axial planes of isoclinal folds, best seen by salmon-colored meta-cherts (R) and compositional banding (T). Hinge:limb thickness variations locally exceed 20:1 (T, Lotos). (S) Along the limbs of upright folds like (P), coaxial stretching leads to boudinage of competent lenses. These structures record top-WNW shear, but top-ESE structures occur in roughly equal proportions. (U) Symmetric quartz-filled pressure shadows on delta-type D_S garnet porphyroblasts. (V) Asymmetric, non-coaxial strain during exhumation is limited to localities proximal to the Vari Detachment, like this example from Fabrikas.